



**POROUS EMITTER COLLOID THRUSTER PERFORMANCE
CHARACTERIZATION USING OPTICAL TECHNIQUES**

THESIS

Eric T. Wolf, Captain, USAF

AFIT-ENY-13-M-36

**DEPARTMENT OF THE AIR FORCE
AIR UNIVERSITY**

AIR FORCE INSTITUTE OF TECHNOLOGY

Wright-Patterson Air Force Base, Ohio

APPROVED FOR PUBLIC RELEASE; DISTRIBUTION UNLIMITED.

The views expressed in this thesis are those of the author and do not reflect the official policy or position of the United States Air Force, Department of Defense, or the United States Government. This material is declared a work of the U.S. Government and is not subject to copyright protection in the United States.

**POROUS EMITTER COLLOID THRUSTER PERFORMANCE
CHARACTERIZATION USING OPTICAL TECHNIQUES**

THESIS

Presented to the Faculty

Department of Aeronautics and Astronautics

Graduate School of Engineering and Management

Air Force Institute of Technology

Air University

Air Education and Training Command

In Partial Fulfillment of the Requirements for the
Degree of Master of Science in Aeronautical Engineering

Eric T. Wolf, BS

Captain, USAF

March 2013

APPROVED FOR PUBLIC RELEASE; DISTRIBUTION UNLIMITED.

**POROUS EMITTER COLLOID THRUSTER PERFORMANCE
CHARACTERIZATION USING OPTICAL TECHNIQUES**

Eric T. Wolf, BS
Captain, USAF

Approved:

Dr. David Liu, Capt, USAF (Chairman)

Date

Dr. Carl R. Hartsfield, Lt Col (Ret), USAF (Member)

Date

Dr. William E. Wiesel, Jr. (Member)

Date

Abstract

This research focuses on experimentally determining the performance parameters of a colloid thruster with porous emitters using optical techniques. Porous emitters contrast with traditional needles by allowing a variation in the number and size of Taylor Cone locations throughout a range of propellant flow rates. Droplet exhaust characteristics, thrust, and specific impulse specifications must be investigated across the span of flow rates to understand the thruster's operational envelope and potential mission capabilities. Optical methods, including image analysis, image correlation, and use of a fiber optic distance sensor, are evaluated to verify their applicability in obtaining the thruster's range of performance. Algorithms are created to calculate the estimated minimum and maximum number of emitter sites based on imaged porous emitter head topography. Then, theoretical performance models for the variable number of emitter sites are established. The variable and fixed numbers of emitter site models present a positive order of magnitude comparison demonstrating the initial accuracy of the variable model. This variable emitter baseline model can be utilized by future researchers to understand the expected performance range prior to laboratory testing. Experimental techniques for evaluating thrust through elasticity measurements and droplet exit velocity with image examination schemes are proposed and assessed for their compatibility with thruster testing. Calibration and sensitivity analyses show the elasticity procedure is a practical method for thrust determination. Comparisons explain why image correlation is a more promising approach to velocity determination than image streak tracking. Upcoming experimentalists may apply the predetermined elasticity and image correlation

AFIT-ENY-13-M-36

methods to obtaining the colloid thruster thrust and exit velocity, respectively. The research results provide theoretical thruster performance models and experimental procedural investigations laying a foundation for future investigational colloid thruster testing and characterization.

To my amazing wife and wonderful daughter

Acknowledgments

I would like to thank my advisors Capt Liu and Lt Col (Ret) Hartsfield for their guidance in this endeavor. Also, I would like to thank my sponsor, Dr. Hargus for allowing me to work on this project and learn more about electric propulsion than I ever could in a classroom. I thank Dr. Reeder for his support and willingness to help me whenever needed. Lastly, I thank all of the ENY lab techs, Capt Ober, and everyone else who helped me along the way. I couldn't have done it without you.

Eric T. Wolf

Table of Contents

	Page
Abstract	iv
Acknowledgments.....	vii
Table of Contents	viii
List of Figures	x
List of Tables	xv
Nomenclature	xvi
List of Abbreviations	xix
I. Introduction	1
1.1 General Issue	1
1.2 Problem Statement.....	3
1.3 Research Objectives.....	5
II. Literature Review	6
2.1 Electrostatic Propulsion Theory	6
2.2 Colloid Thruster Theory	9
2.3 Taylor Cone Formation.....	10
2.4 Droplet Theory.....	13
2.5 Performance Equations	17
2.6 Colloid Thruster and Electrospray Research History	24
2.7 Current Colloid Thruster Research	25
2.8 Thrust Measurement	29
2.8.1 <i>Force Balance</i>	29
2.8.2 <i>Time of Flight</i>	30
2.8.3 <i>Elasticity Measurement</i>	31
2.9 Flowfield Velocity Measurement	33
2.9.1 <i>Direct Visualization</i>	34
2.9.2 <i>Planar Doppler Velocimetry (PDV)</i>	35
2.10 Summary.....	37
III. Methodology	38
3.1 1U Colloid Thruster	38
3.2 Vacuum Chamber	43

	Page
3.3 Emitter Surface Imaging.....	46
3.4 Theoretical Performance Envelope.....	53
3.5 Thrust Measurement	57
3.6 Exit Velocity Measurement	69
3.7 Taylor Cone Formation.....	79
3.8 Summary.....	85
IV. Analysis and Results.....	86
4.1 Emitter Number Range Development	86
4.2 Theoretical Performance.....	93
4.3 Thrust experiment.....	101
4.4 Exit Velocity Experiment	109
4.5 Taylor Cone Visualization.....	117
4.6 Thruster Operation.....	120
4.7 Summary.....	125
V. Conclusions and Recommendations	126
5.1 Conclusions of Research.....	126
5.2 Significance of Research	127
5.3 Recommendations for Future Research.....	128
5.4 Summary.....	129
Bibliography	130

List of Figures

	Page
Figure 1. Schematic diagram of the one-dimensional electrostatic field created between two parallel charged plates and acting on ionized particles in an electrostatic thruster.	7
Figure 2. Schematic diagram of a typical colloid thruster.	9
Figure 3. Taylor Cone geometry showing the opposing electric and internal surface tension stresses.....	12
Figure 4. The Busek Co. Inc. 1U Colloid thruster (left) with a three by three porous emitter head grid and DCIU/PPU electronics package (right).....	38
Figure 5. The colloid thruster's electronics package used to power and operate the thruster.	40
Figure 6. HP 6205B (top) and HP6266B (bottom) provided input power to the thruster's electronics.	42
Figure 7. Schematic diagram of the required connections between the thruster, electronics package, operator computer, and power supplies.....	43
Figure 8. The AFIT bell vacuum chamber located in the GNAT laboratory. This vacuum chamber provided the proper environment for thruster operation.	44
Figure 9. KJLC 979 pressure transducer used on bell vacuum chamber.	45
Figure 10. Zeiss Discovery V12 light microscope used to capture magnified images of the emitter surface topography.	47
Figure 11. USAF 1951 resolution test target used to determine the resolution of an imaging system.	47

	Page
Figure 12. Emitter head image taken by the Zeiss microscope. The highlighted areas are light reflections overexposing the corresponding pixels.	48
Figure 13. Emitter head section demonstrating the varied surface height.	49
Figure 14. Emitter head image highlighting larger holes in the surface allowing propellant to quickly rise to the surface.	52
Figure 15. Schematic diagram of the thrust measurement experiment arrangement.	57
Figure 16. Actual experimental Setup for thrust measurement experiment.	58
Figure 17. Diagram depicting how increasing catcher plate cross-sectional areas can be used to measure the plume divergence.	59
Figure 18. Philtec distance sensor control unit and sensor tip used for measuring the deflection of a cantilever beam.	60
Figure 19. One-dimensional schematic diagram of the exit velocity experiment. A camera is aimed perpendicular to the page and only its representative field of view is shown.	70
Figure 20. Coherent Verdi 5 laser head (Top), power operating unit (lower left), and cooling unit (lower right) used to illuminate the flowfield during the exit velocity experiments.	71
Figure 21. Geometrical ray trace of a plano-convex lens illustrating how a small laser beam is spread into a thin sheet of light.	72
Figure 22. Actual experimental setup for the particle flowfield tracking experiment.	75

Figure 23. Questar QM100 long distance microscope used to view the Taylor Cone formation during thruster operation.....	80
Figure 24. Shimadzu HPV-2 high speed camera used to image Taylor Cone formation.	81
Figure 25. Shimadzu HPV-2 camera connected to Questar QM100 microscope. The connection completes the Taylor Cone imaging system.	82
Figure 26. Arc lamp (right) and power supply (left) used to illuminate the emitter head when attempting to view Taylor Cone formation.....	83
Figure 27. Optical system used to focus light from the arc lamp onto an emitter head. .	84
Figure 28. Processed image from the emitter site estimation algorithm highlighting the negative results of global thresholding over the emitter head such as oversaturation in some areas and under estimation in other areas.....	86
Figure 29. Histograms of the maximum number of emitter sites extrapolated from each local filter over the first eight heads.	88
Figure 30. Emitter head images highlighting surface discolorations.....	90
Figure 31. Emitter head surface fusing example with the fused area highlighted.	92
Figure 32. Emitter head image on a 30 degree angle displaying the profile along the porous head.....	93
Figure 33. Theoretical beam current and thrust varying with volumetric flow rate.	94
Figure 34. Theoretical specific charge as a function of volumetric flow rate.	95
Figure 35. Theoretical specific impulse as a function of volumetric flow rate.	96

	Page
Figure 36. Number of droplets released per second as a function of volumetric flow rate for the constant droplet release rate and variable release rate theories.....	98
Figure 37. Droplet mass as a function of volumetric flow rate for the constant and variable droplet release rate cases.....	99
Figure 38. Theoretical droplet radius as a function of volumetric flow rate.	100
Figure 39. Theoretical droplet charge as a function of volumetric flow rate.	100
Figure 40. Distance sensor response raw data with a 5000 Hz sampling rate.	102
Figure 41. Distance sensor raw data during the 5000 Hz sampling rate in the first four seconds of data collection.....	103
Figure 42. Fast Fourier Transform (FFT) of the 5000 Hz sensor data, shown with logarithmic x-axis.	104
Figure 43. Calibration curve for the cantilever beam thrust measurement setup.	104
Figure 44. Distance sensor response data collected during a calibration. Data points were produced at an average 2.5 Hz.....	106
Figure 45. Uncertainty in the number of droplets in the flowfield as a function of the overall thrust.	108
Figure 46. Sample image of CO ₂ particles using Phantom camera at 20 μ s exposure time.	109
Figure 47. Velocity profile of CO ₂ particles across the span of the flow using image cross-correlation.	110

Figure 48. CO ₂ particle velocity distribution as a function of the particles' minimum diameter.	112
Figure 49. Sample image of CO ₂ particles using Phantom camera at 500 μ s exposure time.	113
Figure 50. CO ₂ particle velocity profile across the span of the flow using the streak tracking method.	114
Figure 51. Particle velocity as a function of minimum streak distance.	115
Figure 52. Emitter head pictures taken with the Shimadzu HPV-2 camera. The pictures show the brightness contrast depending on the location of the mirror used to image the emitter.	117
Figure 53. Three pictures capturing the progression of propellant pooling on the emitter head. Time increases with the pictures from left to right.	118
Figure 54. Beam voltage data captured during the high voltage impedance test as part of the startup procedure.....	122
Figure 55. Beam voltage and valve voltage data captured during thruster startup procedure.	123
Figure 56. Image of the propellant pool around the thruster's base after attempted operation.	125

List of Tables

	Page
Table 1. EMI-IM propellant physical properties [17].....	53
Table 2. Final results from algorithm computing number of emitter sites based on microscope images.....	87
Table 3. Statistics for the extrapolated number of emitter points	89
Table 4. Final parameters used for the cantilever beam	101
Table 5. Calibration data obtained from MATLAB's <i>polyval</i> function	105

Nomenclature

Symbol	Definition	Units
B	Magnetic field magnitude	T
C	Capacitance	F
D	Beam deflection	m
d	One-dimensional distance	m
$d\vec{a}$	Differential surface area element	
dv	Differential volume element	
E	Electric field magnitude	V/m
E_{gen}	Approximated electric field	V/m
E_n	Normal component of electric field	V/m
\vec{E}	Electric field	V/m
F	Thrust	N
F_{el}	Electric force	N
F_m	Mechanical force	N
F_{tot}	Total electromagnetic force	N
f	Focal length	m
f_n	Natural frequency	Hz
f_{st}	Surface tension per unit area	N/m ²
$f(\varepsilon)$	Colloid experimental function	
g_0	Gravitational acceleration	m/s ²
I	Second moment of area of inertia	m ⁴
I_b	Beam current	A
I_{sp}	Specific impulse	s
K	Electrical conductivity	S/m
L	Momentum	N-s
L_b	Beam length	m
L_{las}	Laser sheet length	m
m	Mass	kg
m_{eff}	Effective mass	kg
m_i	Initial mass	kg
m_f	Final mass	kg
$m_{particle}$	Particle mass	kg
\dot{m}	Mass flow rate	kg/s

Symbol	Definition	Units
N	Number of droplets per second	
N_p	Population number	
\hat{n}	Unit normal vector	
P	Pressure change	Pa
P_d	Internal droplet pressure	Pa
P_{in}	Input power	W
P_{jet}	Jet power	W
P_t	Tank pressure	Pa
P_∞	Atmospheric pressure	Pa
Q	Volumetric flow rate	m ³ /s
Q_{net}	Net surface charge	C
q	Electric charge of a particle	C
q_d	Droplet electric charge	C
q/m	Charge-to-mass ratio	C/kg
R_d	Droplet radius	m
R_1, R_2	Principal radius of curvature	m
r	Taylor cone length	m
r_{las}	Radius of laser beam	m
\hat{r}_i	Incident light vector	
\hat{r}_o	Observation vector	
S	Standard deviation	
\vec{s}	Energy, flux density	W/m ²
T_n	Normal component of electric stress tensor	N/m ²
\tilde{T}	Maxwell stress tensor	N/m ²
t	Beam thickness	m
V	Voltage	V
V_a	Accelerating voltage	V
V_s	Surface voltage potential	V
ΔV	Voltage Difference	V
ΔV_s	Spacecraft velocity change	m/s
v	Velocity	m/s
v_{CO2}	Carbon dioxide velocity	m/s

Symbol	Definition	Units
v_e	Exit Velocity	m/s
W	Weight	N
w	Beam width	m
x_i	Trial number	
\bar{x}	Mean	
Y	Modulus of elasticity	N/m ²
z	Distance from cylindrical lens	m
α	Taylor Angle	Radian
γ	Liquid surface tension	N/m
δ	Quantity difference	
δ_{ij}	Kronecker Delta	
ε	Dielectric constant	
ε_0	Permittivity of free space	F/m
η_t	Thruster efficiency	
ϑ	Slope	Radian
κ	Surface curvature	m ⁻¹
λ	Wavelength	m
μ_0	Permeability of free space	(V-s)/(A-m)
$\Delta\nu_D$	Doppler frequency shift	Hz
ρ	Density	kg/m ³
ρ_{CO2}	Carbon dioxide density	kg/m ³
σ	Standard error	
ψ	Theoretical constant	

List of Abbreviations

Abbreviation

ASCII	American Standard Code for Information Interchange
AFIT	Air Force Institute of Technology
CCD	Charge-Coupled Device
CO ₂	Carbon Dioxide
DCIU	Digital Control Interface Unit
EP	Electric Propulsion
FFT	Fast Fourier Transform
GNAT	Geo-orbital Nano-thruster Analysis and Testing
JPL	Jet Propulsion Laboratory
KJLC	Kurt J. Lesker Company
MEMS	Micro-Electro Mechanical Systems
NASA	National Aeronautics and Space Administration
PCA	Potential Capability Area
PDV	Planar Doppler Velocimetry
PPU	Power Processing Unit
ST7	Space Technology 7
TCOM	Thruster Common
USAF	United States Air Force
USB	Universal Serial Bus

POROUS EMITTER COLLOID THRUSTER PERFORMANCE CHARACTERIZATION USING OPTICAL TECHNIQUES

I. Introduction

1.1 General Issue

Space assets are critical to the United States Air Force (USAF) as the 21st Century progresses. Increasing budgetary constraints motivate research into smaller satellites as future testbeds for new space technologies. In fact, the most recent “Technology Horizons”, authored by the USAF Chief Scientist, stated one of the Technology-Enabled Potential Capability Areas (PCAs) is rapidly composable small satellites [61]. These small satellites, often in a CubeSat format, offer benefits throughout multiple operational domains and provide “good enough” capabilities in response to varying space missions. The Air Force Institute of Technology (AFIT) has focused research into this area to advance potential uses. AFIT is researching and testing an in-house CubeSat with the end goal of launching the fully operational satellite [24].

One area of CubeSat research is the propulsion system. Electric propulsion (EP) systems are one option available for CubeSat missions, offering a high specific impulse while minimizing the overall satellite mass. There are several options of EP including ion thrusters, Hall effect thrusters, pulsed plasma thrusters, and colloid thrusters. Each of these options has strengths and weaknesses. However, the colloid thruster, in particular, is seeing a renewed interest as a possible leader in this arena. The colloid thruster has multiple advantages over other EP systems. First, hazardous chemicals and high pressure vessels are avoided with the colloid thruster. Second, the colloid thruster has the ability to adjust its thrust and specific impulse performance to accommodate the required

mission. Third, the colloid thruster can provide a large thrust density when compared to other EP systems. This makes the colloid thruster attractive for missions requiring relatively large amounts of thrust in a small propulsion system package.

One of the key features of a colloid thruster is the emitter. This is the component of the thruster used to release the propellant. A traditional emitter consists of a thin needle with an inner bore or capillary. When an electric field is applied to the needle, the propellant responds by flowing up the capillary and ultimately exiting the top of the needle. The weakness of this design is the numerous needles required for the thruster to provide a substantial amount of thrust. Hence, one objective of colloid thruster design is to create the maximum number of emitter sites within the smallest area possible thereby reducing its overall weight.

Recently, Busek Co. Inc. developed a new type of colloid thruster utilizing a porous stainless steel emitter instead of the traditional mechanisms [14]. This highly compact porous emitter replaces the large number of small needles. The porosity comes from a sintering process resulting in potentially thousands of emitter sites. An additional benefit of the porous emitter is how it may allow the number and size of emission sites to vary with the propellant mass flow rate.

AFIT has acquired and tested this new colloid thruster, manufactured by Busek Co. Inc., which may meet the requirements for AFIT's CubeSat [24]. Ober's research demonstrated the successful operation of the colloid thruster in the AFIT Geo-orbital Nano-thruster Analysis and Testing (GNAT) laboratory [43]. However, the colloid thruster's performance characteristics were not previously examined and this research attempts to experimentally obtain the performance characteristics of the Busek thruster.

The first chapter of this thesis provides the background, motivation, and objectives for this research. The second chapter reviews the history, current state, and relevant discussion of colloid thruster research. Additionally, the experimental techniques of thrust measurement and flow observation are examined. Chapter three explains the experimental methodology used in this work. The experimental results and analysis are provided in Chapter four. Finally, conclusions based upon the results and recommendations for future work are addressed in Chapter five.

1.2 Problem Statement

This research is aimed at testing and characterizing the Busek colloid thruster's performance in a near space environment. Since the colloid thruster has proven operational in the AFIT laboratory, its performance characteristics need to be verified. The individual performance properties, including thrust and specific impulse, combine to form the thruster's overall operational envelope and can be used as a basis for future mission planning.

This new technology has yet to be fully investigated in a laboratory setting. Determining the thruster's operational envelope will validate its theoretical specifications as stated by the manufacturer. The given operating parameters are currently based on theoretical equations with assumptions regarding the propellant properties and porous emitter behavior. Thruster testing can provide more accurate and realistic parameters than the given theoretical estimates.

The operational envelope lays the foundation for mission analysis and discovering the thruster's optimal mission type. Different mission profiles such as orbit keeping or

orbit transfer demand diverse thruster qualities. Once a mission is known, the appropriate thruster can be selected based on the mission requirement for maximum thrust density, specific impulse, etc. Consequently, further work can be accomplished in optimizing the AFIT CubeSat for its specified mission by integrating the colloid thruster into the design after the performance specifications are known.

In addition to characterizing the colloid thruster, innovative methods of measuring electric propulsion performance are needed at AFIT. The colloid thruster has two constraints which prohibit the use of a traditional thrust stand to measure its thrust. The first restriction comes from the thruster's liquid propellant. Using liquid requires the unit to remain parallel to the ground so the propellant can evenly distribute across the emitter heads in the presence of gravity, instead of pooling to one side and flooding. The second constraint is the large differences in the force being measured. The thruster body as a whole has a weight on the order of tens of Newtons, but the thrust produced is on the order of micro-Newtons. There is no thrust stand available that has the required force resolution to can support this heavy of a thruster with enough precision to accurately measure micro-Newton thrust.

Finally, a creative method of measuring the velocity of the particles in the thruster's exhaust plume must be developed. The vacuum chamber to be used for testing has small viewing windows creating a constraint when viewing the exhaust flowfield. Furthermore, the exhaust particles' velocities are too high for any of AFIT's commercial particle tracking software packages to be used. Accurately measuring the velocity of the exhaust plume particles is essential for determining the thruster's specific impulse, a key operational factor.

1.3 Research Objectives

The overall research goal is to characterize the operation envelope of the colloid thruster. This goal is accomplished by developing theoretical performance specifications based on known operating conditions, creating and implementing experimental methods to measure the thruster's specific impulse and thrust. Therefore, the research goal is broken down into four research objectives. The first objective is developing a theoretical operating regime based on known parameters and quantifiable data. Designing new experimental methods to measure thrust and particle velocities, and directly view the exhaust conditions encompasses the second objective. The third objective is to test the newly developed methods in a relevant setting and analyze their usefulness when used with the colloid thruster. The final objective involves using the innovative methodologies with the colloid thruster to collect and analyze the relevant thruster properties of thrust, specific impulse, and emission site dynamics. An indirect objective is to bring new capabilities to AFIT by developing original measurement techniques for colloid type propulsion systems. The first four objectives listed above will ensure an accurate assessment of the colloid thruster's laboratory capabilities and will help reach the research goal of developing the thruster's operational envelope. The following chapters present the background, theory, and research for obtaining these stated objectives.

II. Literature Review

Chapter two provides relevant discussion into the background, theory, current state of colloid thrusters, thrust testing, and flowfield velocity measurement. An overview of the colloid thruster concept is presented, followed by a review of electric propulsion and colloid thruster performance to include some governing equations. A brief history of electrospray and colloid thruster research is given followed by the current status of colloid thruster research. Finally, current research is presented regarding thrust and flowfield velocity measurement.

2.1 Electrostatic Propulsion Theory

Electric propulsion can be defined as “The acceleration of gases for propulsion by electrical heating and/or by electric and magnetic body forces” [28]. There are three general categories of electric propulsion systems electrothermal, electromagnetic, and electrostatic. The primary difference between these three categories is the process used to accelerate the propellant. The colloid thruster is part of the electrostatic thruster family.

Electrostatic thrusters accelerate their propellant by applying a direct electric field to ionized particles. A one-dimensional schematic diagram of this interaction is shown in Figure 1.

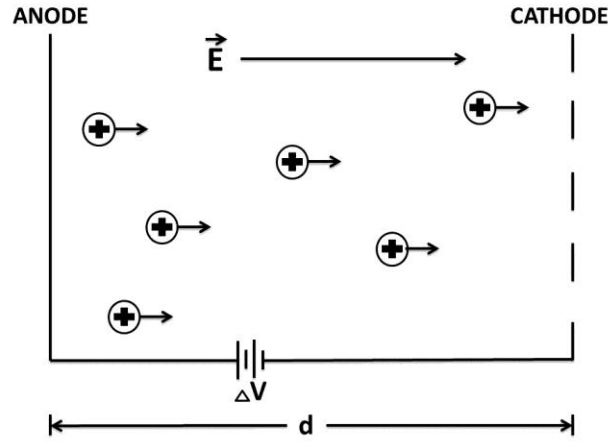


Figure 1. Schematic diagram of the one-dimensional electrostatic field created between two parallel charged plates and acting on ionized particles in an electrostatic thruster.

The electric field interacts with charged particles by generating an internal body force on the particle. This interaction is given by Coulomb's Law, Equation (1), where \vec{F}_{El} is the electric force created on the charge particle and q is the electric charge of the particle [23].

$$\vec{F}_{El} = \vec{E}q \quad (1)$$

The electric force causes the particle to accelerate through the cathode and exit the exhaust nozzle consistent with Newton's second law of motion.

In the operational environment of space, the spacecraft housing the thruster is a closed system with a limited number of electrons. This limiting factor creates a total electrical capacitance, C , of the spacecraft, given by Equation (2), where Q_{net} is the net charge on the surface and V_s is the voltage potential of the surface relative to infinity.

$$C = \frac{Q_{net}}{V_s} \quad (2)$$

As the thruster emits a positively charged ion current, a negative voltage potential accumulates on the spacecraft. The potential can collect at a rate as high as 10^9 volts per second [28]. The voltage potential accumulation can have devastating effects on the spacecraft electronics and thereby mission objectives.

A neutralizing beam is the solution to the charge accumulation problem. After being accelerated out of the nozzle, the still-ionized particles are sent through a neutralizing area. The neutralizing area contains a cathode emitting an electron current. The electrons in this current combine with the ions in the exhaust beam to neutralize the overall thruster emission.

Electrostatic thrusters traditionally use ionized gas as propellant because gas requires less energy than liquid to ionize, although gas may not always be the optimum propellant for a given mission. Gas propellant is much less dense than a liquid and must be stored under high pressure, requiring more structural mass for storage. Plus, each ionized gas has a single, distinct charge-to-mass ratio (specific charge), an important quantity in electric propulsion performance discussed later, setting the performance limitations of the thruster. Alternatively, ions within a homogenized liquid could contain a range of charge-to-mass ratios thus varying the thruster performance as needed during a mission. The freedom of performance specifications could broaden the mission capabilities of a spacecraft.

Liquid propellant has received a renewed interest as a viable propellant with the creation and proliferation of new ionic liquid compounds. An ionic liquid is a room

temperature colloidal liquid containing ions and rapidly changing ion pairs. A force is generated in the ionic liquid similar to the force created in an ionic gas when subjected to an electric field. Due to the similarity in propellant accelerating mechanisms and body forces, colloid thrusters can use these colloidal ionic liquids instead of a gas as propellant to obtain the thruster benefits listed in the previous paragraph.

2.2 Colloid Thruster Theory

A schematic of the typical colloid thruster is shown in Figure 2. The main components are the fluid reservoir, fluid pump and feed, emitter array, extractor grid, acceleration grid, and neutralizer.

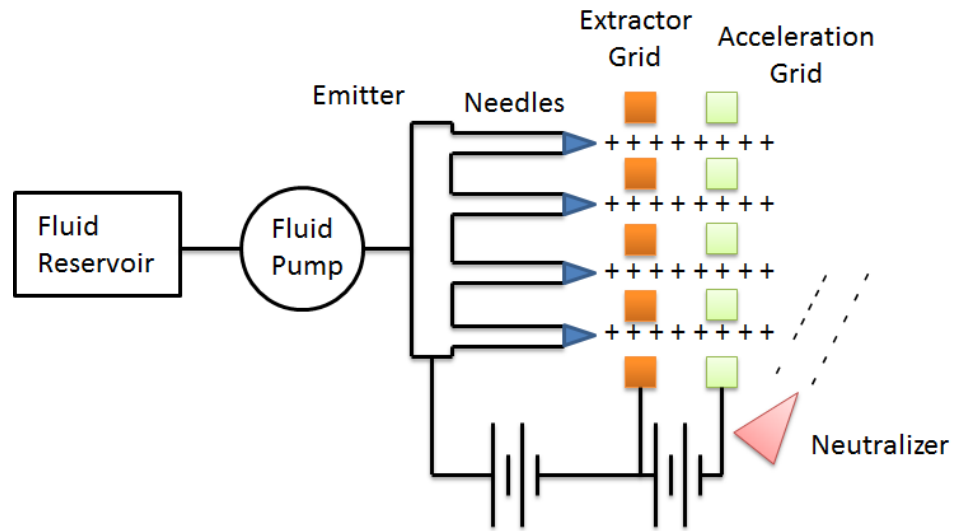


Figure 2. Schematic diagram of a typical colloid thruster.

The fluid reservoir stores the working fluid, or propellant, used by the thruster. Liquid propellant is drawn from the reservoir into a shallow pool under the emitter by the fluid pump and feed.

The emitter contains an array of needles. These needles can either have an internal capillary or have a solid core. An internal capillary allows the propellant to flow through the needle internally and if the needle's center is solid the propellant flows externally up the needle's side wall. Needles with these configurations are referred to as internal and external, respectively. The needle shape is used because it is the most efficient structure for generating a large electric potential at the tip while minimizing the surface area for the propellant to traverse.

An electric potential is applied between the emitter and the extractor grid generating an electric force, Equation (1), on the propellant drawing it up along the emitter needle. When the propellant reaches the tip of the needle, it is balanced by two opposing forces, the pull toward the extractor by the electrostatic field and the pressure keeping the liquid on the tip surface by the propellant's local surface tension. As the electrostatic force's magnitude increases past the surface tension force, the liquid begins to lift off the needle tip in a cone formation toward the extractor. The cone formation has been given the name Taylor Cone after Sir Geoffrey Taylor who first theoretically derived its geometry in 1964.

2.3 Taylor Cone Formation

The previous section described how the propellant is drawn up along the needle emitter and eventually lifted off due to the electrostatic field strength. A large concentration of electric charge forms on the needle tip as the propellant is drawn toward the extractor. The total force on the propellant in the volume of the needle tip is given by Equation (3) where F_{tot} is the total electromagnetic force, \vec{T} is the Maxwell stress tensor

with units of force per unit area, $d\vec{a}$ is the differential surface area vector, ϵ_0 is the permittivity of free space, μ_0 is the permeability of free space, \vec{s} is the energy flux density, and dV is the differential volume element [23].

$$F_{tot} = \oint_S \vec{T} \cdot d\vec{a} - \epsilon_0 \mu_0 \frac{d}{dt} \int_{Vol} \vec{s} dV \quad (3)$$

It is assumed there is no energy lost or added to the system, only the force due to the electrostatic field is present. This assumption removes the second half of Equation (3). Also, the Maxwell stress tensor is given by Equation (4) where E is the electric field magnitude, B is the magnetic field magnitude, and δ_{ij} is the Kronecker Delta [51].

$$T_{ij} = \epsilon_0 \left(E_i E_j - \frac{1}{2} \delta_{ij} E^2 \right) + \frac{1}{\mu_0} \left(B_i B_j - \frac{1}{2} \delta_{ij} B^2 \right) \quad (4)$$

Magnetic fields are assumed to be nonexistent in this interaction making all B terms equal zero. The propellant is assumed to be a perfect conductor so the tangential electric field forces are also zero. The remaining electric field component is in the normal direction to the surface, E_n . These assumptions reduce the nine tensor components in Equation (4) to the three normal components, T_n , given by Equation (5).

$$T_n = \epsilon_0 \left(E_n^2 - \frac{1}{2} E_n^2 \right) = \frac{1}{2} \epsilon_0 E_n^2 \quad (5)$$

Equation (5) provides the resulting stress on the propellant due to the electrostatic field. This force acts to draw the liquid off the needle tip and toward the extractor.

On the other hand, the liquid's local surface tension holds the liquid on the needle tip and is given by Equation (6), where f_{st} is the surface tension per unit area, γ is the liquid interfacial surface tension and \hat{n} is the unit vector normal to the surface.

$$f_{st} = \gamma \nabla \bullet \hat{n} \quad (6)$$

Meusnier's Theorem can be applied to Equation (6) using a conical surface. After applying Meusnier's theorem and setting the result equal to Equation (5), the normal electric field strength used to form the cone structure is shown in Equation (7), where r is the distance from the cone's apex and α is the angle between the cone centerline and wall [32].

$$E_n = \left[\frac{2\gamma \cot(\alpha)}{\epsilon_0 r} \right]^{1/2} \quad (7)$$

Figure 3 displays the Taylor Cone geometry with its interacting surface tension and electric forces.

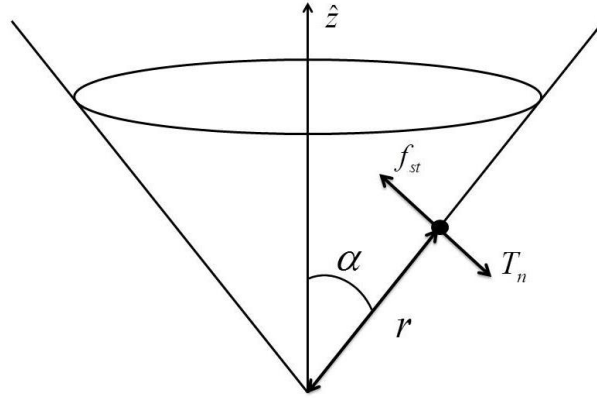


Figure 3. Taylor Cone geometry showing the opposing electric and internal surface tension stresses.

The electrostatic field must be such that the surface of the cone is equipotential. In order to include this constraint, Laplace's Equation was used in the axisymmetric case to solve for the necessary angles. Details of this derivation have been documented by Lozano

[32]. The resulting 49.29 degree angle, the Taylor Angle, specifies the cone surface geometry, and is independent of the liquid parameters or fields involved.

The gradual propellant draw toward the extractor forms the conical structure shown in Figure 3 but instead of coming to a point at the end of the cone, the propellant forms into a thin liquid jet. This is due to the singularity behavior as the cone length, r , goes to zero in Equation (7). Instabilities begin occurring in the flow along the thin jet due to the liquid's surface tension interaction with the external environment and electric and aerodynamic forces. The instabilities create tiny waves on the jet surface. The waves' amplitudes increase along the length of the jet until the stream is no longer stable. Liquid droplets break away from the jet stream and jettison downstream toward the extractor as a result of the instability. Lord Rayleigh first studied this phenomenon and thus this stability limit is called the Rayleigh instability [3].

A great deal of electric power is required to run the extraction and acceleration grids. The power required is a limiting factor during thruster operation because of the limited power supply on the spacecraft. Along with the mechanical systems and physical components, Taylor Cone formation contributes to the decrease in efficiency of the thruster in converting power to useable energy. However, the Taylor Cone formation is one of the physical phenomena present containing key interactions that are central in the operation of the thruster.

2.4 Droplet Theory

The Rayleigh instability causes the liquid jet to break up into liquid droplets. The droplet's velocity, v_e , is determined by the accelerating voltage, V_a , between the

extractor and accelerating grids, the mass, m , and charge, q , of the droplet, known as charge-to-mass ratio, $\frac{q}{m}$. Energy conservation is utilized to calculate the particle velocity from the variables listed above, Equation (8) [32].

$$\frac{1}{2}mv_e^2 = qV_a \Rightarrow v_e = \sqrt{2V_a \left(\frac{q}{m} \right)} \quad (8)$$

The charge-to-mass ratio, $\frac{q}{m}$, has a large impact on a colloid thruster's performance.

Therefore, it is beneficial to know the theoretical limits of this charge-to-mass ratio so the corresponding performance limitations can be estimated. Once the liquid is in the form of a droplet instead of a bulk flow, the local surface tension in the liquid mass accumulated at the needle tip provided by Equation (6) must be replaced by the internal pressure of a liquid droplet. A liquid droplet's internal pressure is found by using the Young-Laplace Equation, Equation (9), where P is the change in pressure across a curved surface, γ is the interfacial surface tension, κ is the curvature of the surface, and R_1 and R_2 are principal radii of curvature at a given point [62].

$$P = \gamma\kappa = \gamma \left(\frac{1}{R_1} + \frac{1}{R_2} \right) \quad (9)$$

The Young-Laplace Equation describes the relationship between the change in pressure across a curved surface and the surface tension of the medium. The limiting case for Equation (9) is when the curved surface is a sphere, causing R_1 , R_2 , and the droplet radius, R_d , to be equal. Equation (9) simplified for the case of a sphere becomes Equation (10) where P_d is the internal pressure of a liquid droplet.

$$P_d = 2\gamma / R_d \quad (10)$$

Since the liquid is in a spherical droplet instead of an accumulation at the needle tip, the internal pressure of Equation (10) replaces the local surface tension, given in Equation (6) and is balanced by the stress from the electric field given by Equation (5). The limit on the electric field strength at the droplet surface is calculated by setting the electric stress in Equation (5) equal to the pressure in Equation (10) and solving for the normal electric field. Equation (11) shows the resulting normal electric field strength.

$$E_n = \sqrt{\frac{4\gamma}{\varepsilon_0 R_d}} \quad (11)$$

The force of any electric field strength above this value overcomes the liquid's internal pressure and deforms the theoretically spherical droplet creating secondary disintegration into smaller droplets.

Assuming the droplet is perfectly spherical, Gauss' Law, Equation (12), provides the electric field on the surface of the spherical droplet where \vec{E} is the electric field on the drop of liquid, q_d is the electrical charge on the drop, ε_0 is the permittivity of free space, and R_d is the radius of the drop [23].

$$\vec{E} = \frac{q_d}{4\pi\varepsilon_0 R_d^2} \quad (12)$$

The maximum charge a spherical droplet can hold is calculated by setting the two droplet electric fields in Equation (11) and Equation (12) equal and solving for the droplet charge, q_d . The maximum droplet charge is shown in Equation (13).

$$q_d = q_d^{\max} = 8\pi\sqrt{\gamma\varepsilon_0 R_d^3} \quad (13)$$

Although Equation (13) gives the theoretical maximum charge on a liquid droplet, previous research has determined the droplet becomes unstable when $0.5q_d^{\max} \leq q_d \leq q_d^{\max}$ [32]. In the region when the droplet charge is above $0.5q_d^{\max}$, tiny waves develop similar to the liquid jet stream and the droplet's shape quickly becomes non-spherical. The non-spherical shape is inherently unstable and leads to secondary liquid disintegration or evaporation.

Finding the maximum charge-to-mass ratio of the droplet is now a matter of dividing the maximum charge shown in Equation (13) by the definition of spherical mass, $\frac{4}{3}\pi R_d^3 \rho$, where ρ is the liquid's density. The result is shown by Equation (14).

$$\left(\frac{q}{m}\right)^{\max} = \frac{6\sqrt{\epsilon_0 \gamma}}{\rho R_d^{3/2}} \quad (14)$$

The minimum droplet charge-to-mass ratio has been theoretically determined as one half of the maximum value [32]. Nominal operating extremes for the propellant's charge-to-mass ratio are set by the minimum and maximum charge values.

Once the droplets are released from the liquid jet, the electric force on the particles caused by the voltage potential between the extractor and accelerator grids propels the droplets out of the engine at the designed exit velocities. A neutralizing anode is placed outside of the accelerator grid to emit opposing electric charges and neutralize the exiting propellant. A neutralizer is not necessary in the successful operation of the thruster, but may be critical during actual space missions for reasons previously discussed.

This concludes the discussion about the many internal mechanisms and electrical interactions within the colloid thruster. While the Taylor Cone and droplet properties are helpful to know, the main concerns with colloid thrusters, as with any thruster, are the overall performance specifications.

2.5 Performance Equations

Space propulsion systems are described and analyzed using many different performance parameters. However, four key parameters are typically at the forefront of thruster design. These key parameters are thrust, specific impulse, power, and efficiency. These design elements are highly interrelated to each other and to the inputs from an electric thruster (i.e. current, voltage, and propellant mass flow rate).

The definition of thrust is the force supplied by the thruster. It is derived from Newton's second law of motion relating force to the time rate of change of the momentum. Momentum is defined as a mass multiplied by its velocity, shown in Equation (15), where L is momentum, m is mass, and v is velocity.

$$L = mv \tag{15}$$

Differentiating both sides of the momentum equation results with the time rate of change of momentum equaling the time rate of change of mass multiplied by the velocity, Equation (16), assuming a constant velocity.

$$\frac{dL}{dt} = \frac{dm}{dt} v \tag{16}$$

Newton's second law states the time rate of change of momentum is equal to the force on an object. Also, the time rate of change of mass is equal to the mass flow rate.

Substituting these relationships into Equation (16) provides the result of the rocket thrust

for space propulsion, given by Equation (17), where F is the thrust, \dot{m} is the mass flow rate and v_e is the exit velocity of the propellant.

$$F = \dot{m}v_e \quad (17)$$

Momentum is produced when mass is propelled out the back of an engine. The spacecraft must then increase its momentum in the opposite direction because the total system momentum is conserved. This momentum change is the applied force by the thruster.

Another important performance parameter is the specific impulse, I_{sp} . The specific impulse characterizes the amount of thrust obtained for a given mass flow rate, typically specified in units of seconds, Equation (18), where g_0 is the gravitational acceleration [26].

$$I_{sp} = \frac{F}{\dot{m}g_0} = \frac{v_e}{g_0} \quad (18)$$

When thrust is held constant, a smaller mass flow rate corresponds to a larger specific impulse. A smaller mass flow rate for a given thrust is desirable because it means the propellant has more energy as it exits the thruster and less propellant is required for a given mission.

Mass flow rate equals the propellant particle flow rate, in particles per second, multiplied by the particle mass, shown in Equation (19) where $mass_{particle}$ is the particle's mass.

$$\dot{m} = \frac{\# particles}{time} \times mass_{particle} \quad (19)$$

Since electrostatic thrusters operate with propellant masses near those of atoms, the mass flow rate is extremely small. These small mass flow rate numbers correspond to a relatively large specific impulse for electric propulsion. The ideal rocket equation shows why this is advantageous. A large specific impulse translates into overall propellant mass savings over a long duration mission.

The ideal rocket equation, Equation (20), is derived from the analysis of momentum exchange and infinitesimal mass and velocity changes during thruster operation where m_i is the initial vehicle mass, m_f is the final vehicle mass, and ΔV_s is the required total change to the spacecraft's velocity [26].

$$\frac{m_i}{m_f} = e^{\Delta V_s / I_{sp} g_0} \quad (20)$$

The purpose of Equation (20) is to relate the initial and final spacecraft masses to the amount of propellant needed for a given mission requiring a total velocity change, ΔV_s . A small initial to final mass ratio is desired meaning less propellant is required to complete a given mission. The thruster's specific impulse has a direct effect. Larger specific impulses reduce the spacecraft mass ratio. Large specific impulses make electric propulsion systems attractive for many space mission applications.

Another look at Equation (18) shows the specific impulse is directly related to the exit velocity of the particles. This means by determining the particles' exit velocity, one can directly obtain the system's average specific impulse. Colloid thrusters have the ability to vary the mass flow rate. Therefore, a relationship exists indicating that as the mass flow rate is decreased, the specific impulse and exit velocity of the particles are increased.

The power of a thruster's jet is yet another important specification in its characterization. The system's jet power, P_{jet} , is related to the thrust, mass flow rate, exit velocity, and specific impulse by Equation (21) [55]. Jet power is defined as how much power is contained in the jet stream. In other words, how much useful power is being used in the exhaust stream.

$$P_{jet} = \frac{1}{2} \dot{m} v_e^2 = \frac{1}{2} F I_{sp} g_o \quad (21)$$

The electric power demanded by the thruster from the spacecraft is a limiting factor in electric propulsion performance. Equation (21) shows how power, thrust, and specific impulse are directly related. Choosing to maximize thrust or specific impulse becomes a mission dependent trade-off when the power is fixed.

Finally, the thruster's efficiency in converting its source electrical power into jet power, η_t , is given by Equation (22) as the jet power divided by the total necessary input power, ΣP_{in} [55].

$$\eta_t = \frac{P_{jet}}{\Sigma P_{in}} \quad (22)$$

Energy or efficiency lost in a colloid thruster comes from many sources, but is dominated by the formation of the Taylor Cones. Colloid thrusters carry an additional efficiency loss because of their ability to emit ions and droplets. This phenomenon is named the polydispersity efficiency [32]. Stated another way, the propulsive efficiency measures how well energy from the electric source in the spacecraft is converted to thrust power delivered.

In addition to the electrical efficiency, another efficiency loss comes from the imperfectness of the exhaust plume. Ideally, all exhaust would be directed exactly parallel to the thruster so all of the particles work to produce thrust in the desired direction. Yet in reality, some particles stray at various angles from the centerline exhaust. The occurrence of unwanted particle separation from the axial direction is called plume divergence. Plume divergence is one area contributing to the overall thruster efficiency loss and is experimentally determined.

The equations developed thus far are applicable to all general electric propulsion thrusters. Electrostatic thrusters have the unique characteristic of expelling a charged propellant, as opposed to a neutral propellant, out of the engine to produce thrust. Additional equations relating thrust and specific impulse are gained from knowledge of the charged propellant characteristics.

Propellant qualities such as electrical conductivity, surface tension, and density are critical components in the design and operation of a colloid thruster. Along with these propellant properties, the propellant's charge-to-mass ratio, $\frac{q}{m}$, the thruster's total beam current, I_b , and volumetric flow rate, Q , are important design parameters. The charge-to-mass ratio is an inherent quality of each droplet being propelled from the engine during operation. Every droplet contains a certain charge due to its electrical nature and having a finite mass. The droplet's charge divided by its mass gives the charge-to-mass ratio. This parameter was developed earlier in this chapter when laying the foundation for the Taylor Cone theory and equations. The total beam current of the thruster is the summation of the charge on each individual droplet being expelled per unit

time, seen in Equation (23) where N is the number of droplets emitted per second and q_d is the individual droplet charge. Equation (23) assumes each droplet has the same charge.

$$I_b = \sum Nq_d \quad (23)$$

The total beam current is related to the volumetric flow rate and propellant properties, shown in Equation (24) [14]. In Equation (24), ε , Q , K , and γ are the propellant's dielectric constant, volumetric flow rate, conductivity, and surface tension, respectively. The additional function $f(\varepsilon)$ is determined experimentally, a function of the liquid's dielectric constant, and is dimensionless.

$$I_b = f(\varepsilon) \sqrt{\frac{QK\gamma}{\varepsilon}} \quad (24)$$

Equation (25) relates the charge-to-mass ratio of the liquid droplets during a specified operating condition to the beam current and volumetric flow rate, where ρ is the propellant density [14].

$$\frac{q}{m} = \frac{I_b}{\rho Q} \quad (25)$$

Equations (23), (24), and (25) are useful in determining the properties of the exhaust beam, but to provide any usefulness in characterizing the thruster, these must be related to the thrust and specific impulse.

Another parameter that is crucial in determining the system's performance is the accelerating voltage, V_a , also referred to as the beam voltage. The accelerating voltage is the thruster's applied voltage used in creating the electric field to accelerate the droplets.

The thrust is related to the beam current, accelerating voltage, and charge-to-mass ratio as displayed in Equation (26) [29].

$$F = I_b \sqrt{\frac{2V_a}{\left(\frac{q}{m}\right)}} \quad (26)$$

Equations (24), (25), and (26) can be combined into a single equation for thrust containing the two independent variables, the volumetric flow rate and the accelerating voltage, Equation (27) [66].

$$F = \sqrt{2V_a \rho f(\varepsilon)} \left(\frac{K\gamma Q^3}{\varepsilon} \right)^{1/4} \quad (27)$$

A similar expression for the specific impulse, can be written by combining Equation (27) with Equation (18) and using the relationship of the mass flow rate equaling the volumetric flow rate divided by the density, Equation (28) [66].

$$I_{sp} = \frac{1}{g_0} \sqrt{\frac{2V_a f(\varepsilon)}{\rho}} \left(\frac{K\gamma}{Q\varepsilon} \right)^{1/4} \quad (28)$$

Equations (17), (18), (21), and (22) show how the four parameters of thrust, specific impulse, power, and efficiency can be obtained by measuring the thrust generated by the propulsion system and the exit velocity of the propellant. The correlation between the four key parameters is a tool used by mission planners to understand the range of performance of the colloid thruster. For this reason, measuring thrust and exit velocity are a focus of this thesis.

Equations (24), (27), and (28) display the relationship between the beam current, volumetric flow rate, beam voltage, thrust, and specific impulse. The porous emitter thruster may have the option for the operator to command the beam current and beam

voltage. The thruster uses these two variables to set its propellant emission levels for the correct amount of thrust. Hence, these equations are critical to theoretically determine the performance of the thruster given user input values.

2.6 Colloid Thruster and Electrospray Research History

The genesis of colloid thruster technology dates back to 1917. John Zeleny began extensive research into the formation and visualization of the disintegration of electrified liquid surfaces where his experiments used various liquids, such as ethanol and glycerin [68]. The process of using electric potential to disperse liquids is now termed the electrospray process. Following the initial work of Zeleny, various researchers continued to study the electrospray effect through the 1950's. The 1960's saw another boost in related research. In 1964, Sir Geoffrey Ingram Taylor analytically described the electrospray liquid cone formation, as opposed to the previous pure visualization and experimental analysis [57]. For his influential work the phenomenon of the cone formation and disintegration from the electrospray is named the "Taylor Cone". In the early 1960's, Victor Krohn proposed the idea of using electrosprays as the thrusting mechanism for space propulsion. Research into Krohn's propulsion concept continued through the 1970's with experiments to understand different propellant behavior, characterize thruster performance due to its unique ability to mix ions and droplets, and characterize colloid emissions through time of flight measurement techniques. In the early 1970's, Kidd and Shelton created a 432 needle prototype thruster consisting of 12 arrays each made out of 36 needles. One array completed 4350 hours of testing [63]. Their research efforts were able to demonstrate a 15% performance loss at the end of the

testing providing the first indication of the colloid thruster lifetimes. Mainstream research of colloid thrusters steadily decreased and became dormant for the next two decades. The high operative voltages and complexity of colloid thrusters diverted the attention of researchers to the less complex and mission capable ion engines. In addition, the Space Shuttle was introduced and dominated National Aeronautics and Space Administration's (NASA) and the Department of Defense's space budget causing the new and "high risk" programs of colloid thrusters to be largely scaled back.

Interest in colloid thrusters was revamped in the mid-1990's. During this time, the prospect of micropropulsion devices became an area of interest because of its relative small size and light weight. An influential article from the NASA Jet Propulsion Laboratory (JPL) stated, "Of all micro-electric primary propulsion options reviewed so far, colloid thrusters are quite possibly the most suited for micro-spacecraft primary propulsion applications" [39]. Independent companies such as Phrasor and Busek sprouted up and continued research into this area along with Universities, such as Massachusetts Institute of Technology, Yale, and Stanford. Many of these research efforts are funded by government entities such as NASA and the United States Air Force [63].

2.7 Current Colloid Thruster Research

The NASA JPL has been a major contributor to many of the recent advancements in colloid thruster research and technology due to its Space Technology 7 (ST7) demonstration mission [48]. Many researchers in government, industry, and academia have contributed to colloid thruster research for the ST7 mission. The goal of the ST7

mission is to test the use of colloid thrusters in the Disturbance Reduction System for future applications of precision formation flying. Many risks of micro-newton colloid thrusters including the thrust command and control, the thrust noise, and thruster lifetime will be addressed. This is the first time colloid thrusters will be launched into space for operational use. The thruster has been ground tested to the fullest extent possible and the projected launch date is 2014 [69].

Due to the many on-going research efforts, the colloid thruster operating theory, design, and testing have given rise to well documented performance parameters. However, two current research areas, plume characterization and system miniaturization, continue to have a strong emphasis in modern research efforts.

Predicting the characteristics of the exhaust plume continues to elude researchers. Plume characteristics are measurable in a laboratory setting using the time of flight, retarding potential, and Faraday cup techniques. These techniques are used to measure such values as the charge-to-mass distributions of the beam particles, beam profiles, and energy density of the particles, respectively [21]. The measured values are then used to map the plume particle distributions and trajectories. Since colloid thruster plume research is still in its relative infancy, direct measurement and laboratory experiments have been acceptable to understand the characteristics. However, the focus is on developing models of the plume in order to facilitate new designs and optimize future colloid thrusters [56]. The great variances in charge-to-mass ratio, particle size, and mass flow rate of the propellant correspond to a large variation in the plume profiles of these thrusters. Working models of these changing variables will be vital for future mission

planning. However, experimental research will remain critical to verify and validate the results of the models. Once the model has provided results sufficiently in agreement with the experimental data, the model is used to analyze more complex or new thruster scenarios. One such new thruster idea is scaling down current thrusters to micro-sized using Micro-Mechanical-Electrical Systems (MEMS) technology.

Advancements in MEMS technology have opened the door for the realization of miniature thrusters. The physics behind colloid thruster operation enable the thruster to be scaled down into a micro-sized system [40]. Research into MEMS fabrication has introduced new possibilities for different needle/emitter configurations. Instead of the traditional macroscopic emitter needles to extract the propellant, emitters can be micro-fabricated on a silicon substrate resulting in extremely small emitters, on the order of tens of microns in diameter [29]. This research will continue to grow as the need for micro propulsive devices becomes greater with pico- and nano-satellite designs.

Since MEMS devices can fit a large number of emitters into a small area, a current research topic is the interaction of multi-emitters for electrospray applications. As the needles get smaller and closer together due to MEMS fabrication, the number of emitters per unit area becomes very high. Therefore, the close proximity of the charged droplets released from the needles can create a significant space charge resulting in electrical shielding and ultimately cessation of droplet emissions.

An alternative to numerous single emitters in a compact area may be larger porous emitters. AFIT is investigating this new porous surface emitter approach. Instead of using discrete emitter sites at the tips of needles, material is sintered together to

produce a rough surface allowing for a various number of emitter sites. The number and size of the emission sites, or Taylor Cones, depend on the thruster's beam current, acceleration voltage, and emitter topography. If the acceleration voltage is made constant, the variation in beam current changes the number of emission sites.

A small beam current will result in a small amount of thrust, as seen in Equation (26). Equation (24) shows how the beam current is directly related to the propellant flow rate. A small flow rate means the propellant will travel slowly to the emitter surface. As it gets near the surface, the strong electrostatic field will draw the ionic propellant to the surface where it will be emitted. Since the electrostatic field is pulling the propellant to the surface by its electrical charge, its size will be small. The small amount of propellant will result in a small Taylor Cone emission site. The Taylor Cone will be anchored to a peak in the emitter's topography because the peaks are closest to the extraction grid creating the strongest electrostatic fields. The small amount of propellant being emitted from each site will require numerous sites in order to create the necessary beam current and corresponding thrust. Equation (27) shows a direct relationship between the flow rate and thrust. Small flow rates will produce small amounts of thrust. Alternatively, Equation (28) shows an inverse relationship between flow rate and specific impulse. A small flow rate creates a large specific impulse. As the beam current increases, the flow rate also increases. More propellant in the emitter will distribute the electric field charge so less propellant will be pulled to the surface by the electric field. More propellant will be pushed to the surface by the feed system. The mass of the individual propellant streams will increase and thus the size of the emission sites will also increase. The

increase in emission site size will require less emission sites for the necessary beam current. Finally, at high beam currents, the flow rate will be high as well. It is believed the feed system will push enough propellant through the emitter head to create a small pool on the surface. The large pore structure of the emitter head will create local maximum electric field points and the emission sites will center on these. The electric field will have a great deal of propellant to draw from resulting in large emission sites. The large emission site magnitudes will require fewer sites for the needed thrust. At this condition, the thrust will be the largest and the specific impulse will be minimized due to the respective direct and inverse relationship to the flow rate, as previously discussed in the low flow rate case.

2.8 Thrust Measurement

Electric propulsion systems deliver thrust at the nano- or milli-Newton level as a consequence of their high specific impulse and low mass flow rate design. Measuring these thrust forces at the micro-Newton level presents many challenges. Forces with a much greater magnitude, such as spring, gravity, and friction, can interfere with the measurement of smaller forces. However, novel methods and systems were developed to measure the tiny forces of electric thrusters. These innovative techniques include balance systems, time of flight measurement, and beam deflection measurement.

2.8.1 Force Balance

Various balance designs, such as the capacitive and pendulum, were created using non-contact sensors to measure the displacement or rotation of a lever arm due to an input force. However, some of these systems are limited by the total mass and external

vibration. Therefore, a commonly used design is a torsional balance [18]. This method uses a sensor to measure the angular displacement of a balance arm caused by thrust from a propulsion system. The axis of rotation is normal to the gravity vector making the thruster's weight independent of the force measurement. Flexural pivots connecting the balance arms to the system are nearly frictionless and tuned to dampen out any vibrational forces or displacements. Another direct measurement system similar to a torsional balance is a pendulum balance.

A pendulum balance is designed so the thruster rests on a platform hanging from a moment arm attached to a base by a pivot point of known stiffness. AFIT's pendulum balance was successfully utilized for measuring the thrust of electric propulsion devices. However, the problem with the pendulum balances is it measures force directed tangent to the ground. This is an issue with measuring the colloid thruster since the force of the colloid thruster in this direction would require the thruster to be operated while the exit plane is rotated 90 degrees. Thruster rotation would make the liquid propellant pool towards the side and flood the thruster. Propellant flooding would then cause the extractor grid to have an electrical short which would not allow the propellant to travel up through the emitter.

2.8.2 Time of Flight

An alternative technique for determining thrust is using the time of flight method. In this method, the time it takes an exhaust particle to traverse a known distance is measured and provides the particle's velocity. The thrust and mass flow rate are then calculated from the particle's known time of flight, thruster acceleration potential, and thruster current [19]. There are many variations to this approach in which different

variables are directly measured to obtain different parameters, such as the charge-to-mass ratio of the propellant, thruster efficiency, and beam potential.

Although this process is common, it does have some limitations. For instance, the procedure increases in complexity when more than one emitting source is used. The exact relationship between the stopping source (electrostatic gate) and collector (metallic plate) is unknown. Two factors cause this ambiguity, first, the gate needs to close fast enough to simultaneously block all of the emitters and second, it is not directly known which emitter released the last particle hitting the collector plate. Also, the measured time of flight can have relatively large variations due to the polydispersive nature of the exhaust plume, the limited detector speed, and beam potential variation. In addition, capacitive coupling between the collector plate and high voltage gate signal may be involved distorting the time of flight results [32].

2.8.3 Elasticity Measurement

A third method of obtaining thrust is to measure the displacement of a cantilever beam as a result of thrust acting on it [66]. The Euler-Bernoulli beam theory is fundamental to this measurement technique. The mechanical force, F_m , on the cantilever beam due to the displacement at the free end is given by Equation (29), where D is the beam deflection, L_b is the beam length, Y is the beam Modulus of Elasticity, I is the beam second moment of cross sectional area, w is the beam width, and t is the beam thickness [50].

$$F = \left(\frac{3YI}{L_b^3} \right) D = \left(\frac{Ywt^3}{4L_b^3} \right) D \quad (29)$$

Thus, by inverting Equation (29), the force is directly related to the displacement through the beam stiffness, where the beam stiffness is the value in the parentheses.

The experimental setup is straight-forward. A device producing exhaustive thrust is setup so the thrust vector is directed at the free end of a cantilever beam. As the thruster operates, the exhausted particles impact the beam on the free end causing measurable deflection. A non-contact sensor is then on the opposite side of the beam's free end which measures the tip deflection. The measured deflection is then used in conjunction with Equation (29) to calculate the resultant thrust from the measured displacement.

There are two main features of this technique that make it favorable for measuring the thrust on the colloid thruster. The first positive aspect is the relatively small amount of equipment required. There are only three main components of the experiment, the thruster, beam, and sensor. Once the beam is properly tuned to minimize vibration, while providing an adequate displacement range, the data collection process is relatively simple since there are no outside electrical fields or moving parts involved.

The second advantage of this system is the absence of the colloid thruster's weight in the measurement. Since the sensor only measures the displacement of the beam, it is independent of the thruster's weight. This is convenient since the thruster weighs orders of magnitude more than the thrust it produces, such as the case with the colloid thruster.

On the other hand, this method has two negative aspects. The first is the Euler-Bernoulli beam theory approximates the force on the free end of the beam as a point source [50]. This means in order for the equation to approximate the thruster force, the

area on the beam where the force acts needs to be minimized. If the force acts through a large enough area, this approximation will not hold and the point force would need to be treated as a pressure. However, this negative aspect can be overcome when using an array of emitters instead of a single emitter by funneling the exhaust plume from the emitter array down to a single attachment point on the beam.

The second adverse feature of the elasticity measurement method is how the displacement sensor output contains two components. The first component is the desired displacement caused by the thrust and the second component is the undesired free vibration of the beam [67]. A large free vibration will result in errors to the displacement readings, thus special care is taken to minimize this source of error by adjusting the beam stiffness to dampen the vibration. The beam stiffness is most sensitive to changes in the thickness and length where the stiffness is proportional to both the thickness and the length cubed. Thus increasing the thickness will increase the stiffness for a given length of beam reducing the free vibration. Conversely, if the thickness is too large, the increased stiffness will dampen the sensitivity of the measurement and the displacement sensor will not have necessary resolution. The beam's vibrational response to the thrust can have a significant impact on the results so the beam's stiffness must be properly tuned in order to reduce the undesired vibrational affects.

2.9 Flowfield Velocity Measurement

Flowfield measurement using optical techniques has proliferated in recent years due to advancements in laser, image capturing, and computing technologies. There are

numerous methods available to visualize flowfields and measure properties such as particle velocity.

2.9.1 Direct Visualization

One of the most straightforward methods to measure flowfield velocity is to directly capture images of the particles in the flowfield. The captured images offer quantitative information about the flowfield such as the particles' path and travel distance based on the known exposure time. This is the method used by Tirsi to calculate the exit velocity of a Pulsed Plasma Thruster [60]. Tirsi was able to view an entire particle streak pattern in one image and back out the velocity from the exposure time and length of the streak.

If the entire streak is not present in each image, digital image correlation data is used to find the velocity of a given particle. Digital image correlation involves analyzing localized subsets within an image to determine the movement of a pattern from one image to the next [58]. A distinct pattern or template subset figure in one image is designated. The template passes across a second image and the sum of the products of image intensities, or pixel values, is computed for each template location. A maximum correlation value results from the area of the second image with the best correlation to the template. The number of pixels between the location of the template pattern in the first image and highest correlated point in the second image provides the pixel movement of the object being tracked. There are many commercial cross correlation algorithms used for image correlation, such as MATLAB's *xcorr* function. A cross correlation function uses the same algorithm as digital image correlation, but it can be applied to any matrix, not solely digital images. Digital image correlation is a well-known method which has

proven successful for simple flowfield patterns, as well as when the particles in the flow are visible and distinct from frame to frame. The relative simplicity of this method makes it an ideal candidate for exit velocity measurements for the colloid thruster plume. More complicated flows with indistinguishable particles require more sophisticated methods for velocity determination.

2.9.2 Planar Doppler Velocimetry (PDV)

Particle Image Velocimetry (PIV) and Planar Doppler Velocimetry (PDV) are two alternative methods of flowfield velocity measurement. Particle Image Velocimetry requires placing foreign seed particles into the flow and tracking the particles throughout the flowfield. PDV has an advantage over PIV where it does not require flow seeding. This makes the PDV a non-intrusive method of obtaining velocity and turbulence information in various flowfields.

The PDV method typically uses a penetrating light source, imaging system, and filter to take advantage of the visual Doppler Effect seen from small particles or molecules in motion [1]. When incoming light interacts with a small particle or molecule, a fraction of the light scatters. The frequency of the scattered light shifts from its original value due to the Doppler Effect. The Doppler Effect on scattered light is determined by the velocity of the particle with respect to the incoming light and the observation direction of the final scattered light [38]. This frequency shift is a measurable quantity used to obtain the original velocity of the particle. The Doppler shift of incoming light due to interference with a particle is the basis behind PDV measurements.

Determining the velocity of engine exhaust particles is one application of PDV. This application requires measuring the Doppler shift induced by the thruster's exhaust particles when flowing through a sheet of laser light. A laser beam with a known frequency is spread into a thin sheet of incoming light with a unit vector, \hat{r}_i . The engine is fixed in such a way as to cause the exhaust particles to travel through the sheet with velocity, v_e . Outgoing scattered light is observed by two imaging systems, typically CCD cameras, one with a filter to block the incident laser light and background light, and one without a filter to collect the Doppler-shifted light. The unit vector of observation from the particle to the camera is labeled \hat{r}_o . The Doppler frequency shift of the scattered light, $\Delta\nu_D$, is then given by Equation (30) where λ is the wavelength of the incoming light.

$$\Delta\nu_D = \frac{1}{\lambda} v_e (\hat{r}_o - \hat{r}_i) \quad (30)$$

Planar Doppler Velocimetry is very robust making it a suitable alternative experimental method for determining the exit velocity of the colloid thruster's exhaust plume particles. It has been successfully used in numerous applications providing a velocity measurement when the flowfield is rapidly changing or too complex for image correlation techniques. However, the number of experimental items and the precise system calibration required makes the direct visualization with image correlation method a more appropriate first choice in velocity measurement techniques.

2.10 Summary

The colloid thruster operation theory including Taylor Cone formation and performance equations were discussed in detail. Next, an overview of the history of colloid thruster research was provided, followed by current on-going research. In addition thrust measuring techniques were also discussed including balances, time-of-flight technique, and elasticity measurements based on beam theory. Finally, flowfield measurement techniques were addressed including direct visualization measurement and PDV.

III. Methodology

The methodology and equipment used to achieve the research goals are outlined in this chapter. The colloid thruster itself and equipment required for operation such as the vacuum chamber and power supplies are discussed first. Then, a detailed description of the processes and tools used to accomplish the thesis objectives is presented.

3.1 1U Colloid Thruster

Busek Co. Inc. developed and provided the porous emitter colloid thruster. Two components comprise the thruster system, the thruster itself and the electronics module, shown in Figure 4. The electronics module contains the Digital Control Interface Unit (DCIU) to interface with the operator's computer terminal and the Power Processing Unit (PPU) to provide power to the thruster.

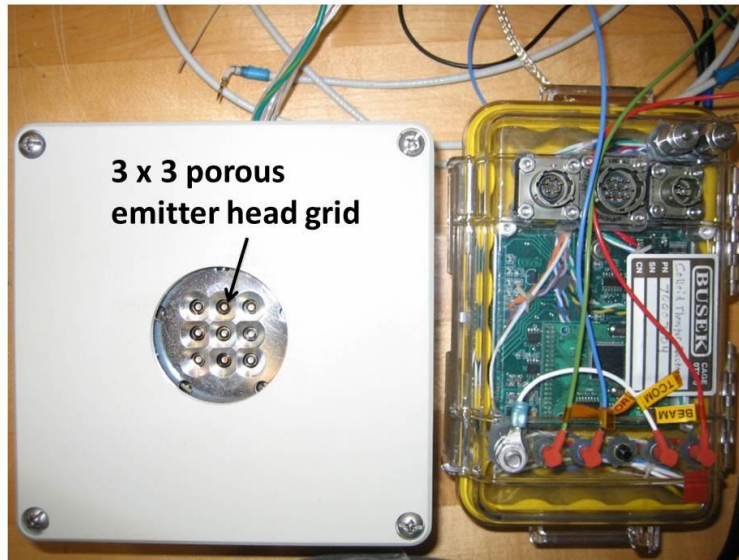


Figure 4. The Busek Co. Inc. 1U Colloid thruster (left) with a three by three porous emitter head grid and DCIU/PPU electronics package (right).

This thruster was developed in 2010. Nine large porous emitters located in a three by three grid replace the need for potentially hundreds of smaller single emission needles. The thruster is designed for operation in an environment with a pressure of less than 9×10^{-6} torr. The Busek Co. Inc. has determined the maximum nominal thrust to be 1 mN. A gray protective metal box with 6 inch long and 4 inch high sides surrounds the thruster. The present mass of the thruster including its housing is approximately 2.5 kg.

There are many internal subassembly mechanical systems enabling the operation of the thruster its operation. Inside the thruster, the subsystems include a heater and propellant storage, feed system, and flow control valve. The heater lies at the bottom of the thruster and maintains a constant temperature throughout the system. A constant operating temperature is important to keep the propellant's chemical properties consistent throughout operation. In addition, the high beam voltages between the emitter and extractor grid create heat. If this heat is not balanced throughout the thruster, large temperature gradients could occur and damage critical components. The heater has a 15 W power output. A 50 mL metal container rests above the heater storing the propellant. A connected bellow is pressurized to 30 psi with dry nitrogen and provides back pressure to push the propellant up into the emitter array. Propellant flow from the storage container into the emitter is regulated by a piezo-actuated flow valve. The valve voltage is dependent on the thruster beam current. Therefore, the magnitude of the beam current sets the required propellant flow rate. The piezo valve opens and closes accordingly releasing the desired amount of propellant. The valve actuation has a maximum voltage of 200 V.

The thruster also has the ability to operate a carbon nanotube field emission cathode. This cathode neutralizes the exhaust beam to balance any spacecraft charge during operational use, a requirement discussed in Chapter two. The cathode has a maximum input voltage of -800 V resulting in electron currents greater than 1 mA. Even though the cathode was available to use during the laboratory experiments, excess charge was not a concern, so the cathode was not installed into the thruster.

Although the previously discussed systems are important for successful operation, the thruster cannot operate as a stand-alone unit. It must receive its power and electronic commands from an external source, the DCIU/PPU package, shown in Figure 5.

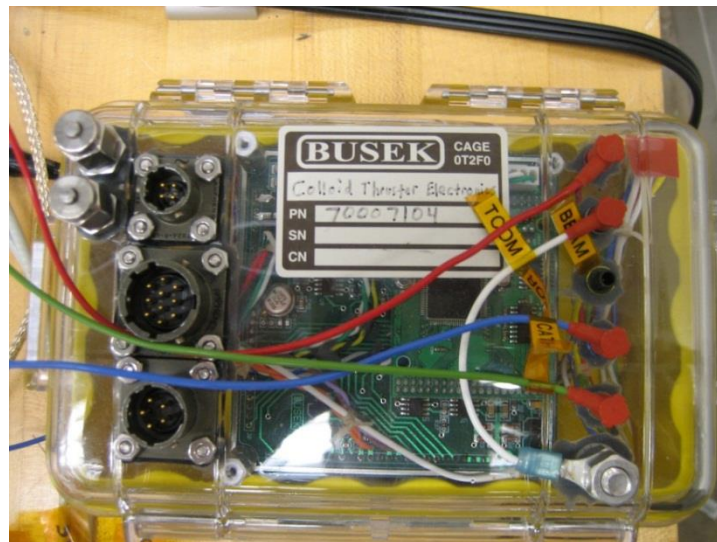


Figure 5. The colloid thruster's electronics package used to power and operate the thruster.

The DCIU/PPU controls the power provided to the thruster, is the interface between the thruster and the operator's computer, and acts as the central processing unit during thruster operation. During operation, the electronics package remains at standard

atmospheric conditions outside the vacuum chamber. Inside the container, the electronic boards are submerged in Fluoroinert, a liquid preventing arcing or short-circuiting by isolating the high voltage components. In Figure 5 the colored wires connected to the PPU on the right side of the image are high voltage wires, carrying voltages up to 10 kV. The high voltage wires are connected to corresponding wires from the thruster through high voltage electrode pass-throughs on the vacuum chamber wall. A chassis wire was connected to the vacuum chamber to ground the PPU. The thruster common wire, or TCOM, was connected to the chassis as a common connection point for the electronics. There are three cannon plug ports on the left side of the electronics package. To regulate the heat during operation, the four pin plug connects to the heater element in the thruster. A de-bugging wire connects via the five pin plug, for Busek to troubleshoot any thruster problems. Finally, the 12 pin plug attaches to an RS-232 communication port, connecting the PPU to the operator's computer terminal. Additionally, the 12 pin plug connects to separate 28 V and 5 V power supplies providing input power to the electronics.

The 28 V power source provides approximately 1 A of current and powers the DCIU/PPU. Communication channels between the computer, electronics, and thruster are powered by the 5 V power supply. An HP 6266B and an HP 6205B were the power supplies used in the experiments, as seen in Figure 6.



Figure 6. HP 6205B (top) and HP6266B (bottom) provided input power to the thruster's electronics.

The final component required to operate the thruster is the operator computer software. A Labview-based executable program allows the operator to control the thruster via the DCIU/PPU. The interface permits the operator to command electrical inputs and receive operational output data. Three different thruster operational modes, beam current control, thrust control, and manual, are available to the user through the executable program. A specific beam current, up to $300\ \mu\text{A}$, can be set with the beam current control mode. The thrust control allows a specific thrust level to be maintained with a maximum of $1\ \text{mN}$. Finally, the manual mode provides control of multiple parameters and is intended for use only during troubleshooting. The operator software also has the ability to log operational data into a text file. Real-time graphs updating approximately once every second can be observed by the operator as well.

The 1U Colloid Thruster is an extremely sophisticated electric propulsion system with many subsystems working together to enable the thruster's operation. This section has given a brief overview of the main components. A schematic of the connections between the thruster, electronics package, operator computer, and external power supplies is given in Figure 7. More in depth information about the thruster's design and operation can be found in [14] and [43].

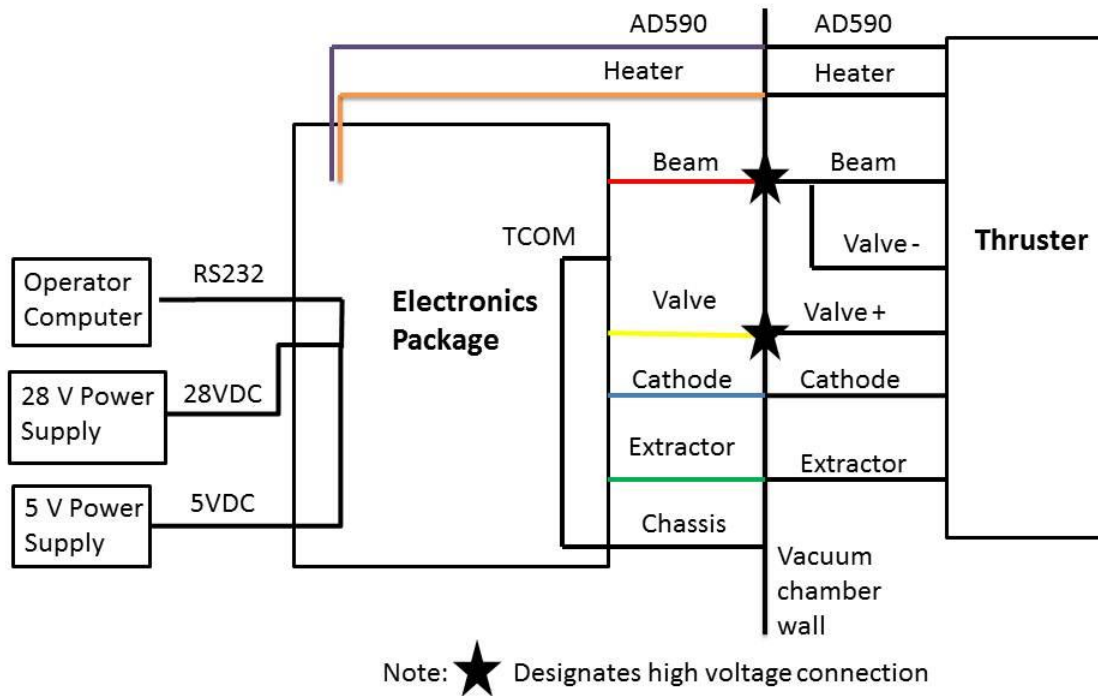


Figure 7. Schematic diagram of the required connections between the thruster, electronics package, operator computer, and power supplies.

3.2 Vacuum Chamber

The bell vacuum chamber located in the AFIT Geo-orbital Nano-thruster Analysis and Testing (GNAT) Laboratory produces the necessary vacuum for the thruster's operation. A picture of the bell chamber is shown in Figure 8.

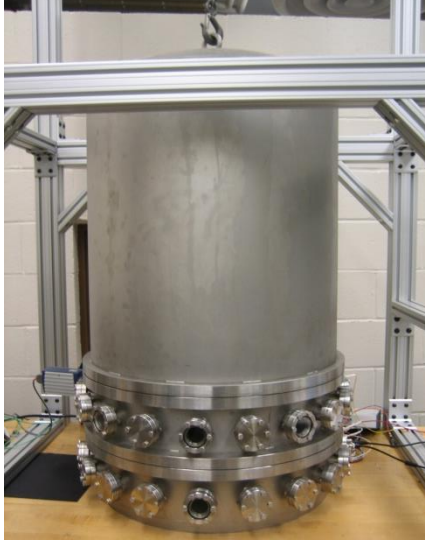


Figure 8. The AFIT bell vacuum chamber located in the GNAT laboratory. This vacuum chamber provided the proper environment for thruster operation.

The chamber has a useable inner diameter of 23 inches and an inner height of 38.25 inches. There are two rows of 18 ports located near the bottom; each port has a diameter of 1.25 inches. Windows or high voltage feed-throughs can be interchanged with the solid metal ports. The top row of ports can be removed, shrinking the overall height of the chamber. A single larger window with a 4 inch diameter is located 12 inches above the upper row of small ports. A limited number of visual access points into the chamber are allowed by the single large window and smaller circumferential ports. Access to the inside volume is granted through a pulley system used to vertically lift the chamber.

The vacuum system for the bell chamber is capable of creating a vacuum below 10^{-8} torr. A roughing pump, Welch 1374 belt-drive model, and diffusion pump, Varian VHS-6, work together to create the vacuum pressure. A KJLC 979 Series wide-range combination vacuum gauge, displayed in Figure 9, measures the chamber pressure. The KJLC 979 transducer is connected to a KJLC PDR900 series controller used to view and

data log the chamber pressure. The vacuum gauge and controller operate at a range of pressures from standard atmospheric pressure to 10^{-10} torr.

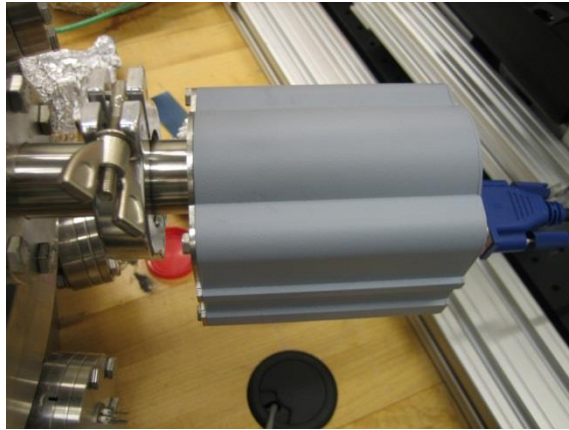


Figure 9. KJLC 979 pressure transducer used on bell vacuum chamber.

Cooling the diffusion pump is a Neslab Coolflow HX-100, a refrigerated recirculation unit. A cooling unit is essential to keep the diffusion pump at an appropriate temperature to prevent the pump's oil from producing vapor. Any oil vapor could leak into the chamber and coat the contents inside. The set-temperature of the cooler was 16 degrees Celsius.

The essential components for successfully operating the colloid thruster have been reviewed. Necessary equipment includes the main thruster unit, the DCIU/PPU, two power supplies, and a computer. The bell chamber provides a suitable vacuum environment as required by the thruster for effective operation. Next, the equipment and procedures used to meet the research objectives are reviewed.

3.3 Emitter Surface Imaging

The unique porous emitter is capable of producing a varying number and size of droplet emission sites determined by the mass flow rate. Estimating the number of emission sites is difficult because the propellant flow dynamics through the porous heads is not well understood. The continuous surface of each head allows multiple emissions, while discrete needle emitters allow only a single emission at a time. Therefore, the first research objective attempts to establish a baseline for the number and arrangement of emission points on the emitter surface during the various operating conditions.

Emitter head images were collected to start the process of gaining a better understanding of the possible number and size of emission points. Then a developed algorithm estimated the number of possible emission points, based on the images taken, for the minimum and maximum propellant flow rates. Once the range of numbers of emission sites was known, the values within the extremes were interpolated.

The cross-sectional area of each emitter head is approximately 7.2 mm^2 . Thus, only a highly magnified image could provide any meaningful insight into the emitter's topography. To the naked eye the emitter head appears relatively flat and level, but on the micron scale, the emitter head terrain is very diverse and uneven. A Zeiss Discovery V12 light microscope, shown in Figure 10, was used to obtain the required magnified emitter surface images. The microscope does not have dynamic image resolution calibration; therefore, the image resolution had to be determined through another avenue. A USAF 1951 resolution test target, shown in Figure 11, was used to determine the microscope's resolution.

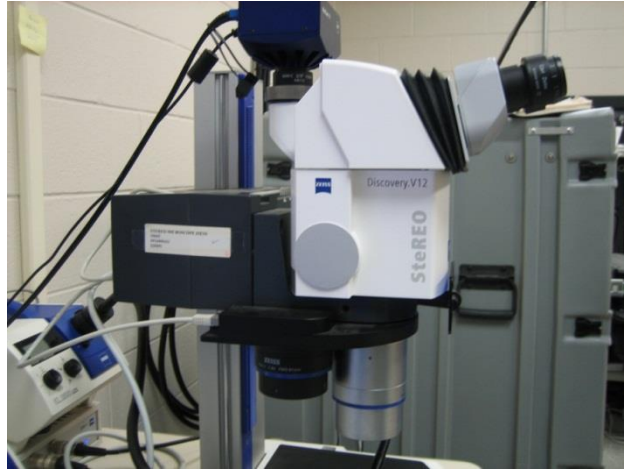


Figure 10. Zeiss Discovery V12 light microscope used to capture magnified images of the emitter surface topography.

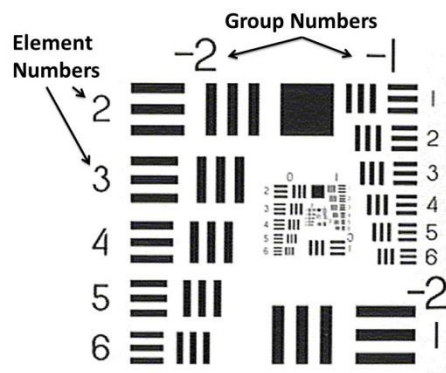


Figure 11. USAF 1951 resolution test target used to determine the resolution of an imaging system.

Two aspects of the imaging system created problems affecting the images. The two problems were overexposure of light in certain areas and a small depth of field. A sample emitter head image is displayed in Figure 12, highlighting overexposed areas on the emitter.

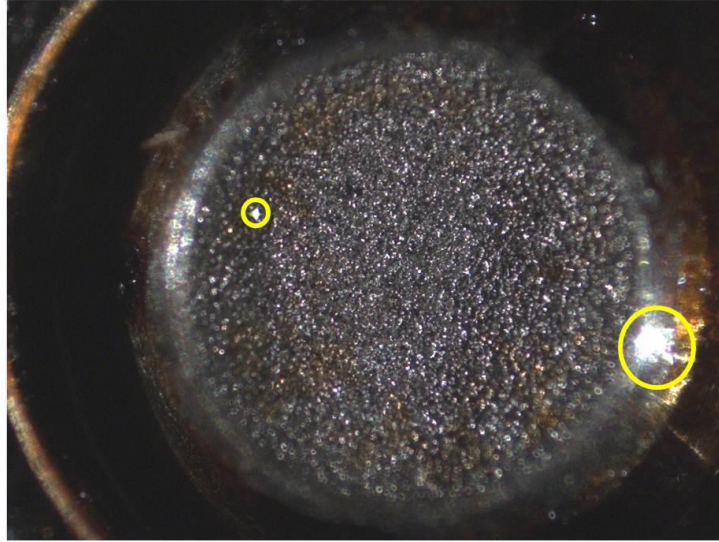


Figure 12. Emitter head image taken by the Zeiss microscope. The highlighted areas are light reflections overexposing the corresponding pixels.

The emitter heads are set down in a thin metal enclosure on the thruster. When capturing the high magnification images, the microscope lens was too close to the thruster to have direct overhead light illuminate the emitter surface. Therefore, point lights were used for illumination. The lights were directed at the heads from the sides of the microscope and reflected off the metal enclosures onto the heads. Nearly every light and thruster angle were attempted to reduce the amount of overexposure in each image. However, a small amount of overexposure remained in each image.

Another obstacle inherent in any imaging system is the depth of field. In an image, the depth of field is the range of distance in focus. The depth of field of the microscope was too small to adequately keep the entire emitter head in focus, because the height of the emitter head varies greatly, as shown in Figure 13.

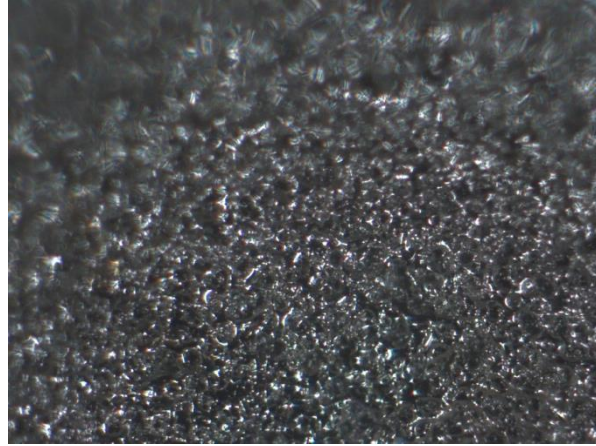


Figure 13. Emitter head section demonstrating the varied surface height.

The bottom of Figure 13 is in focus and displays the center of the emitter head.

However, the top of Figure 13 is out of focus toward the edge of the emitter head. Figure 13 depicts how the center of the emitter head is much deeper than the edges creating a trough structure.

An in-depth discussion of the hypothesis on how the number of emission sites varies with propellant mass flow rate occurred in Chapter two. The first theory was a low flow rate would result in the maximum number of emission sites on the highest emitter head peaks. Visually analyzing the emitter head images, such as Figure 12, showed the illuminating light directed at the head from the side produced numerous bright spots. The brightest spots correspond to the highest points along the surface because they are the closest to the microscope lens and reflect the most incoming light. Each of these points is a possible emitter location during the low flow rate condition. An algorithm to count the bright spots was developed to obtain the maximum emitter site condition.

MATLAB was used to implement the counting algorithm determining the maximum number of possible emission sites. The overall steps of the algorithm are discussed here. First, the images were imported into the algorithm and the *graythresh* and *im2bw* functions were used to threshold and convert the images from grayscale into black and white. Next, the program located the areas with the highest numbers of white pixels, removed these areas from consideration, and calculated the weighted center of mass of the picture. The areas of high white pixel count were the overexposed areas and how large of an area to exclude was decided by the user. After removing the large overexposed areas to prevent those areas from skewing the centroid location, the weighted center of mass of the image was calculated. The calculated centroid was taken to be the center of the emitter head. Then, the program cropped the image around its center based on the user's specification, such as cropping the image to 50% of the emitter area or 75% of the emitter area. 60% was the final value used during the analysis because this percentage gave the largest area of in-focus pixels. Cropping the image around the center eliminates the out-of-focus regions at the edge of the emitter from consideration. Next, a filter to normalize localized sections of the image was created. The filter used the *imfilter* function to sweep through the image finding the local maximum pixel intensity in a small section of the grayscale image and normalized the neighborhood pixels to the maximum. Then the filter recorded any point that was greater than a threshold set by the user, such as 0.8 or 0.9. The threshold of 0.9 was used in the final analysis because after adjusting the numbers, it was assumed 0.9 struck an acceptable balance between too many and too few bright spots considered. A summation of all the points collected by the filter was taken along with an extrapolation from each

filter. After the filter collected points from a given location, the number of points in the filter area was extrapolated to estimate the corresponding number of points within the area of the emitter head. The extrapolation was done as a check to ensure there were no substantial variations in emitter sites between the filter locations.

Each localized peak was a potential emitter during the low flow rate condition. The sum of all of the peaks provided an approximation of the expected number of emission sites. However, a separate method was developed to estimate the number of emission sites during the high flow rate condition.

During the maximum flow rate condition, the sizes of the propellant drops were estimated to be maximized while the number of emission sites is minimized. The emission sites were thought to occur at larger areas of the emitter head than the smaller emission sites previously discussed. If the emission sites for the low flow case occurred at the peaks, then the emission sites for the high flow condition most likely occurred at plateaus. The larger plateaus would draw up the propellant on the surface where it would be pulled by the electrostatic field. Significant open area valleys are present on the porous emitter head complimenting the plateaus where the propellant is able to reach the surface the quickest. These open valleys or “craters” are highlighted in Figure 14.

Determining the minimum number of emitter sites began the same as the method of finding the maximum number. Overexposed areas were removed from consideration, the emitter center was estimated, and the image was cropped to a given percentage of the entire area. After the image was cropped, instead of determining local maximum points, the entire image was taken under consideration.

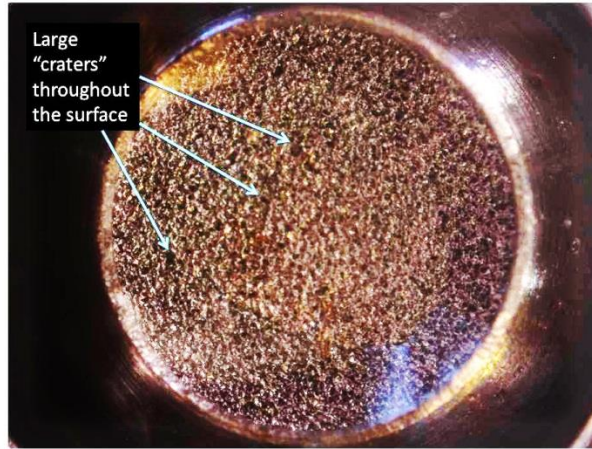


Figure 14. Emitter head image highlighting larger holes in the surface allowing propellant to quickly rise to the surface.

Individual bright points in local areas were grouped together to make a larger emitter area. The user could then decide how big of a pixel area constituted an emitter site and the number of those areas with the selected pixel size or greater were counted as an emitter site.

Statistics were employed in the algorithms to establish the maximum and minimum number of emitter sites. Obtaining the final emitter estimates involved averaging sample data points from individual filters to find the mean. Each set of sample points was termed a population and represented an infinite set of data. An infinite data set can never be sampled so statistical methods provide meaning to the data and give a quantitative result to the limited number of data points. Each set of sample points had an associated mean, \bar{x} , and standard deviation, S , given by Equation (31) and Equation (32), respectively, where N_p was the number of sample points in the population and x_i was the value of a specific sample point [2].

$$\bar{x} = \frac{\sum x_i}{N_p} \quad (31)$$

$$S = \sqrt{\frac{\sum (\bar{x} - x_i)^2}{N_p - 1}} \quad (32)$$

The mean is the average value of the sample points and the standard deviation is an estimation of the variance of the sample population. Another insightful quantity is the standard error, σ , shown in Equation (33).

$$\sigma = \frac{S}{\sqrt{N_p}} \quad (33)$$

The standard error “estimates the standard deviation of the sample mean based on the population mean” [65]. Each data set’s standard error was calculated to give an estimate of the range of values within the set.

3.4 Theoretical Performance Envelope

Equations developed and listed in Chapter two were used to predict the thruster’s operating parameters and performance specifications. First, the known operating conditions of the thruster were used to calculate foundational parameters. Then, those parameters were used to calculate operating conditions outside of the documented values.

Acquiring the relevant electrochemical propellant properties was the first step in the performance analysis. Table 1 provides a compiled list of the relevant properties.

Table 1. EMI-IM propellant physical properties [17]

Property	Symbol	Value
Density (kg/m ³)	ρ	1520
Surface Tension (N/m)	γ	0.0349
Electrical Conductivity (S/m)	K	0.88

The only pertinent value missing from Table 1 is the dielectric constant, ε . Aside from the propellant properties, another important unknown value was the experimental function, $f(\varepsilon)$, first seen in Equation (24). Since both of these parameters are present in Equation (24), they were grouped together to form a new parameter termed the “theoretical constant”, ψ , equal to the experimental function divided by the square root of the dielectric constant as shown in Equation (34).

$$\psi = \frac{f(\varepsilon)}{\sqrt{\varepsilon}} \quad (34)$$

This new function was resolved by knowing the maximum operating conditions of the colloid thruster. The maximum beam current the thruster can support is $300 \mu\text{A}$. A 1 mN thrust occurs at this maximum beam current. Plus, the accelerating voltage was known and taken to be constant at 10 kV throughout the thruster’s operating regime. By knowing the values of F , I_b , and V_a , at the maximum thrust condition, the corresponding charge-to-mass ratio was calculated using Equation (26). Next, the charge-to-mass ratio was used with the known beam current and propellant density to solve for the volumetric flow rate, Q , at the maximum thrust condition using Equation (25). Finally, the theoretical parameter was solved by using Equation (24). After the theoretical parameter was known, it could be used to relate the flow rate to the beam current through Equation (35), where K and γ are the propellant specific conductivity and surface tension, respectively.

$$\psi = \frac{I_b}{\sqrt{QK\gamma}} \quad (35)$$

The theoretical parameter was assumed to remain constant over the performance envelope. In reality however, this parameter is likely a function of the thruster temperature and atmospheric pressure. After obtaining the theoretical function, the thruster's thrust, specific impulse, and charge-to-mass ranges were calculated.

The thrust, specific impulse, and charge-to-mass ratio could be obtained without direct knowledge of the emitter site or droplet information. Independently varying the volumetric flow rate allowed the ranges of these three parameters to be calculated. Given a flow rate, the total beam current was calculated using Equation (35), since all of the other variables were assumed constant and propellant-specific. After the beam current was known, Equation (25) was utilized to calculate the charge-to-mass ratio. Finally, Equations (27) and (28) were used to calculate the resulting thrust and specific impulse, respectively.

The minimum and maximum number of emitter sites were critical in calculating the droplet radius, mass, number of drops, and specific charge ratio variables. Once the maximum and minimum number of sites was determined, a linear profile between them was assumed. After an equation relating the number of emitter sites to the flow rate was established, the beam current and charge-to-mass ratio were obtained using the same process as used for the charge per mass ratio calculation. Once the total beam current was known, it was related to the number of drops per second through Equation (23); however, a relationship between the number of drops per second and number of emitter sites had to be created.

Experimental research has shown the approximate time for the full transient response of a Taylor Cone emission is 1 ms [15]. Therefore, it was assumed one droplet

was released per Taylor Cone emission site every 1 ms. This corresponded to approximately 1000 droplets per Taylor Cone per second, and was assumed to be independent of Taylor Cone size. The total number of drops per emitter head per second was then found by multiplying the 1000 droplets per Taylor Cone by the number of emission sites corresponding to the specified flow rate. Lastly, the number of drops per emitter was multiplied by nine to account for the nine emitter heads. This process resulted in the total number of droplets per emitter per second. The uniformity of the droplets across the entire emitter head was assumed in this development. Since the total number of drops released per second was obtained, the droplet parameter calculations could proceed with Equation (23).

The charge on each individual drop, q_d , was calculated by dividing the total beam current by the number of drops per second. Next, the droplet radius was calculated by dividing the droplet charge by the mass of the droplet, $\frac{4}{3}\pi R_d^3 \rho$, setting this equal to the previously calculated charge-to-mass ratio, $\frac{q}{m}$, and solving for R_d . Equation (36) shows the final result.

$$R_d = \left[\frac{q_d}{\frac{4}{3}\pi\rho\left(\frac{q}{m}\right)} \right]^{1/3} \quad (36)$$

Finding the droplet radius enabled the calculation of the droplet mass using the definition of mass, $\frac{4}{3}\pi R_d^3 \rho$.

Completing the stated series of calculations provided the droplet characteristics relevant to the study of colloid thrusters. This information led to a better understanding the operating regime of the thruster. The theoretical parameters were then used to qualitatively evaluate the effectiveness of the designed experiments at measuring the thrust and specific impulse, thus completing the objectives of this thesis.

The remaining sections of this chapter discuss the experiments created to measure the operational characteristics of the thruster. However, the thruster became inoperable before any of the experiments were performed. Therefore, for each experiment, the theory, setup, and diagnostics are discussed as a template for future use without the application of the experiment to the operating thruster itself.

3.5 Thrust Measurement

The first experiment was designed to measure and characterize the thrust and plume divergence of the colloid thruster. A cantilever beam, a thin plate rigidly attached to the free end of the beam, and a distance sensor were utilized in the experiment. Figure 15 shows a side view schematic diagram of the arrangement.

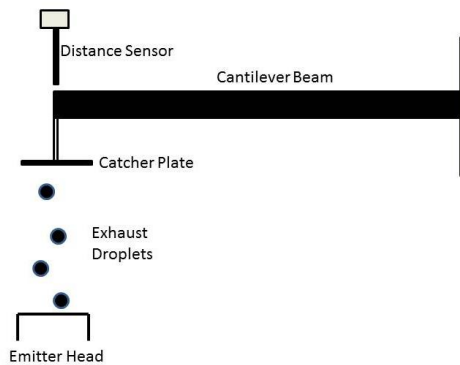


Figure 15. Schematic diagram of the thrust measurement experiment arrangement.

During thruster operation, the exhaust plume would be directed at the catcher plate. A rigid connection is made between the plate and the cantilever beam with known mechanical stiffness and dimensional properties. The force from the exhaust plume incident on the catcher plate would induce a displacement on the free end of the beam. A distance sensor located directly above the beam's free end would measure the displacement distance during thruster operation. Figure 16 displays the actual experimental setup.

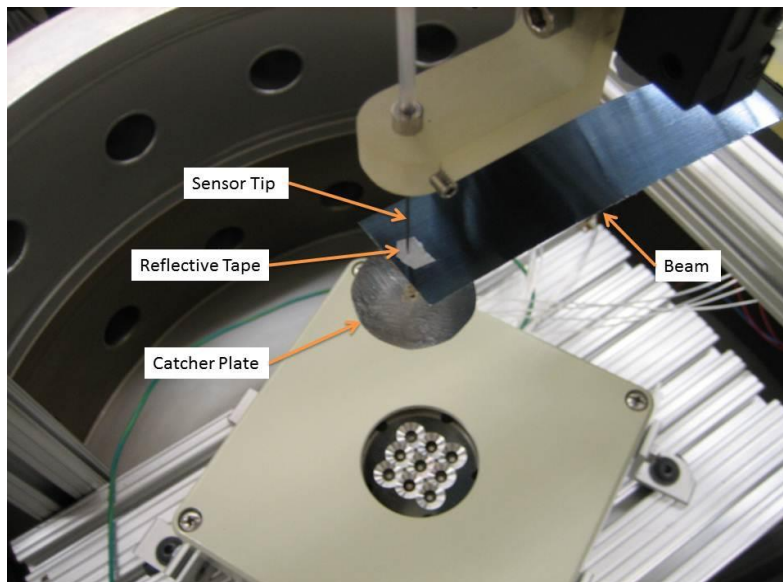


Figure 16. Actual experimental Setup for thrust measurement experiment.

The displacement distance would be subtracted from a reference distance to ultimately determine the deflection of the beam. Equation (29), the Euler-Bernoulli beam theory, would be used to calculate the thrust by relating the beam's stiffness and dynamic deflection to the corresponding required thrust force. Dynamic thrust and plume divergence estimates would be determined from the experimental setup.

Plume divergence would be determined by using a series of catcher plates with increasing cross-sectional areas. The plate with the smallest cross-sectional area would have the same perimeter as the emitter head grid. Then, with each new plate, the area would increase in constant increments while the distance between the emitter and plate would remain constant until a 45 degree angle existed between the outside edge of the plate and the outside perimeter of the emitter head grid. A diagram representing this idea is shown in Figure 17.

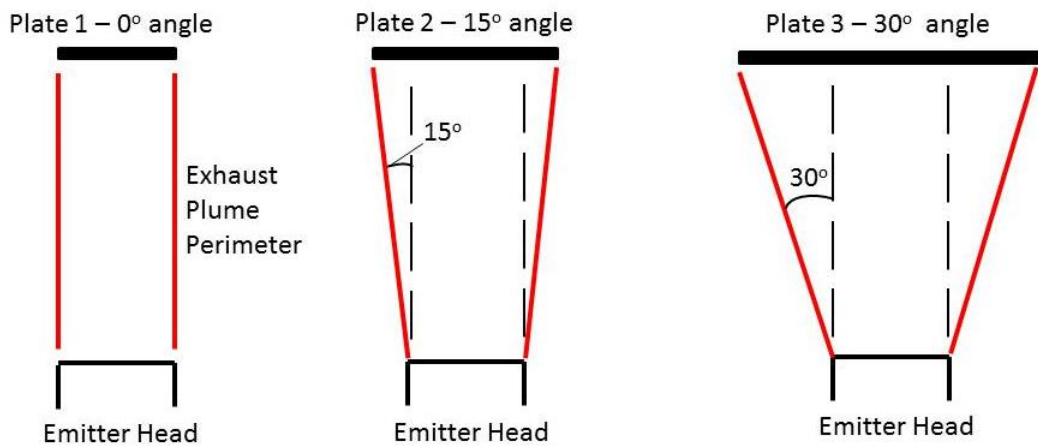


Figure 17. Diagram depicting how increasing catcher plate cross-sectional areas can be used to measure the plume divergence.

The 45 degree maximum was established because this angle is believed to be greater than the largest divergence without becoming large enough to cause the catcher plate weight to change the beam dynamics. Calculating the differences in thrust between each plate, for a given operator input, during operation would result in the amount of plume divergence in a given range of angles. An indication as to how many more particles collide with the larger plate as opposed to the smaller plate would be given by the thrust

difference. Next, the individual components of the experiment are discussed. Although the experiment was not complete due to the malfunction of the thruster, some calibration work was successfully accomplished.

The distance measuring sensor best suited for this application is the Philtec RC20. It is a reflectance compensated fiberoptic sensor. Side by side fiberoptics are located at the tip causing light reflected off the target to follow two different paths into the sensors where it goes through a ratiometric calculation, making the distance reading independent of varying surface reflectance. The sensor has a spot size of 0.5 mm and a linear range of just over 1 mm. Power for the RC20 sensor is provided by the muDMS amplifier. The muDMS amplifier connects to a computer via USB and is controlled using proprietary software. Figure 18 displays the RC20 sensor and muDMS amplifier.

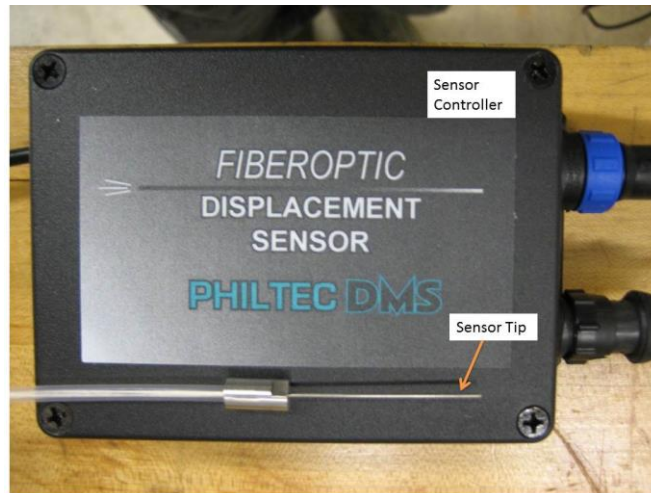


Figure 18. Philtec distance sensor control unit and sensor tip used for measuring the deflection of a cantilever beam.

The sensor has an internal sampling rate of 10 kHz and its output is an averaged point across the sampling rate. A sample rate of 2.5 s was used during sensor calibration

and operation to receive a more time-averaged reading. The time-averaged reading eliminated the need for numerical filters on the data. Also, more data points increase the accuracy of the averaged point.

Since the displacement sensor uses optical measurements, all of the window ports on the vacuum chamber were covered to remove stray light from the chamber, hence removing noise from the sensor's reading. During operation, the muDMS amplifier was placed outside the vacuum chamber and connected to the sensor through a specialized vacuum port. The sensor was fixed above the cantilever beam.

The beam used in the calibrations was a piece of AISI 1095 spring steel shim stock. Spring steel was chosen as the material because of its durability, long fatigue life, and low outgassing properties. After the material and beam thickness selection, analysis was completed to calculate the remaining beam dimensional parameters to ensure the 0.01 inch thick AISI 1095 steel could be used for the experiment. Determining the total desired beam displacement was the first step in the analysis.

The maximum total linear range of the Philtec distance sensor is specified as being close to 1.0 mm. Thus, the beam would need to be placed 0.5 mm from the sensor for a full range of linear motion, positive and negative deflection, detected by the sensor. The maximum range of the beam tip itself is then 0.5 mm. A safety factor of two was introduced into the analysis to compensate for the small distance from the beam to the sensor. It was unknown how much the real beam would deflect under a given load. If the beam deflected more than the theoretical value, it would collide with the sensor, so the safety factor helped prevent any collisions between the beam and sensor. The final

result of the maximum desired beam tip deflection was 0.25 mm. Establishing the beam dimensional parameters of length and width was the next step in the beam analysis.

A code solving the Euler-Bernoulli cantilever beam deflection equation, Equation (29), was developed to tune the physical beam dimensions so the maximum force on the beam results in a displacement of less than 0.25 mm. The limiting dimensional constraint was the requirement to fit within the vacuum chamber with enough space to clamp one end while placing the thruster beneath its other end. Other considerations in the calculations were the catcher plate assembly mass and the beam mass. The catcher plate mass was estimated to be 2.0 g and the weight of the beam itself was estimated as two point masses located at the fixed and free ends. A set giving a deflection of 0.25 mm by a force of 1 mN was found by the program iterated through possible length and width dimensions. To match the tolerances of creating the piece, the final length and width were rounded. The final length and width were 6.8 inches and 1 inch, respectively, corresponding to a maximum theoretical deflection of 0.2 mm. After the final set of beam parameters was chosen, the Euler-Bernoulli beam theory for a cantilever beam's slope at the free end, Equation (37), was used to ensure the arc length of the beam due to the slope, θ , was no larger than the order of magnitude of the beam thickness, to satisfy small displacement assumptions [50].

$$\theta = \frac{FL_b^2}{2YI} \quad (37)$$

In Equation (37), F is the thrust force acting on the free end of the beam, L_b is the beam length, Y is the modulus of elasticity, and I is the second moment of the beam cross-sectional area. Equation (37) was used with the final beam dimensions and the resulting

maximum slope was 0.12 degrees. The subsequent arc length due to the slope was 0.01 inches, where the arc length was approximated as equal to the beam length multiplied by the slope. This arc length equals the beam thickness, but is assumed to be an acceptable value given the mass assumptions and rounding error. Ensuring the system's estimated natural frequency was out of range from the sampling rate was the last step in the beam's dimensional analysis.

After the dimensions of the beam were finalized through using the Euler-Bernoulli beam equations, the system's theoretical natural frequency was calculated using the Rayleigh Method of Effective Mass. The natural frequency is the frequency at which a system will naturally vibrate without outside disturbances. It is important to know the natural frequency of the system. The natural frequency may affect the collected data by adding extraneous oscillations. Therefore, the natural frequency should be far outside the range of the sampling frequency. The mass of the catcher plate was again estimated to be 2.0 g. Half the beam mass plus the catcher plate mass combined to make the total effective system mass. This effective mass was then used in Equation (38) to find the system's natural frequency [59].

$$f_n = \frac{1}{2\pi} \sqrt{\frac{3YI}{m_{eff} L_b^3}} \quad (38)$$

In Equation (38), m_{eff} is the effective system mass, L_b is the length of the beam, Y is the modulus of elasticity, and I is the second moment of the beam cross-sectional area. The resulting theoretical natural frequency of 6 Hz was estimated to be out of the range of any data sampling. Therefore, the beam dimension parameters were finalized. Once the beam dimensions were decided, the physical beam was formed from the shim stock.

After obtaining the shim stock from the distributor, it had to be cut to the calculated size. The shim was cut using metal clippers due to their ability to provide clean, straight cuts. However, cutting this thin metal introduced a permanent length-wise curve to the piece. This slight curve was assumed to have a negligible effect on the beam's material properties. Plus, any distortion in the beam was accounted for during calibration.

Following the beam formation, it was sandwiched between two stereo-lithographed blocks to form the clamped end. The blocks were able to rotate about the horizontal axis. This rotation was necessary and counteracted the cut-induced curve so the free end was parallel with the emitter surface. Lastly, a piece of reflective tape was placed on the beam under the sensor so the sensor would have enough optical return signals to make an accurate measurement.

When using the Euler-Bernoulli beam theory the force on the beam is assumed to act through a point. In order to help comply with this assumption, the catcher plate was rigidly connected to the beam through as small an area as possible. Electrical wire and hot glue created the small connection point. The electrical wire served to provide a buffer distance between the beam and catcher plate and tune the catcher plate's final position relative to the thruster. Hot glue produced the rigid connection between the plate and wire.

The catcher plates were made from aluminum foil. Foil was determined to have the combined properties of being both lightweight and sturdy. Also, it is assumed the metal foil's structural properties would not change significantly when put in a vacuum. A digital caliper was used to measure the diameter of the emitter head grid to size the

diameter of the smallest catcher plate. The diameter measured 1.39 inches. Then the caliper was used to set the distance on a handheld compass. A razor blade was placed inside the compass and the catcher plates were cut from pieces of aluminum foil. This way, the diameter of the first catcher plate was the exact diameter of the emitter grid. The other plates were created in the same manner with a cross-sectional radius of two, four, and six inches to gradually increase the catching area. As the area of the catcher plate grew, there was more of a tendency for the perimeter to sag under its own weight. Electrical wires were connected to the plates because they were rigid, yet light enough, to keep the surface of the plate on one plane. Since 6 inches was the maximum plate radius, the beam and catcher plate assembly was adjusted so the catcher plate was located 6 inches above the emitter surface to achieve the 45 degree maximum divergence angle. The varying size of catcher plates is instrumental in understanding the plume divergence.

The nature of the liquid droplet plume is a relatively new phenomenon and it was unknown how the exhaust plume and catcher plate would interact. More specifically, the largest concern was whether the interaction would cause particles to rebound off or adhere to the plate. Therefore, two actions were taken to mitigate the effects of either of these occurrences. First, the surface of the foil incident to the exhaust flow was scoured using 320 grit sandpaper. Scouring the foil made the surface extremely rough relative to the droplet size. The uneven surface means if the droplets ricocheted off the foil, they would most likely travel in random directions instead of reflecting directly back toward the emitter heads. On the other hand, if the particles stuck to the plate instead of bouncing off, a charge would build up over time. It was unknown exactly how any accumulated plate charge would affect the experiment. An assumption was the charge

would repel the incoming droplets, causing a loss of acceleration and thrust, therefore the corresponding beam deflection would decrease. To mitigate any problems with the droplets remaining on the plate the foil was neutralized. The foil catcher was rigidly connected to electrical wire and the wire in-turn was connected to the beam, as discussed in the previous paragraph. This made a circuit running from the foil plate through the steel beam. A wire with alligator clip ends was attached on one side to a metal frame and attached on the other side near the clamped base of the beam. The alligator clip wire acts as a ground to neutralize the system.

The beam and sensor components were connected to an 80/20 aluminum scaffolding and placed in the vacuum chamber. Even though the physical elements were ready for the experiment, the system had to be calibrated before an accurate measurement of thrust could be made. A system calibration was critical prior to thruster operation. The control masses were various pieces of string and wire and were weighed using the Mettler Toledo MS204 analytical balance, with a precision of ± 0.00005 g, to acquire their calibration mass. Eleven masses were used with masses ranging from 0.001 g to 0.1122 g. Once the set of known masses was obtained, they were placed on the catcher plate individually and the displaced distance was measured by the sensor. Afterward, a correlation, or calibration curve, was created between the added weight and distance displaced.

The RC20 distance sensor has pre-programmed factory calibration curves used to set the distance from an object. In performing these calibrations the mirror (specular) curve was used. The sensor was set to a transmit power of 100% and had an average receive power of approximately 25%. The calibrations were set to digitally output a data

point at an average of 4096 readings, or at a rate of approximately 2.5 Hz. During the first unweighted condition, a range of output sampling rates was captured. The quickest sampling rate was $200 \mu\text{s}$ per point. This fast output setting was used to compare to the slower averaging data to ensure the data sets were consistent.

Using the range of masses previously stated, the beam deflection was calibrated. The calibration process consisted of measuring an unloaded condition, where no additional mass was added to the catcher plate. Then a mass was placed on the catcher plate and the loaded condition was measured. The calibration proceeded this way until all of the weights had been measured.

A real time graph, updating with every output point, of the beam displacement was available to the user. After adding or removing a mass, the time to settle into a steady-state was approximately 1 minute. The steady state condition was defined as the peak-to-peak distance readings remaining less than $1 \mu\text{m}$. In order to get a sizable amount of sampling points, each calibration setting was measured for 2 minutes, or twice the time to reach steady state. After all of the calibration data were taken, the mean and standard deviation of the sample points were calculated. This gave a statistical representation of the average deflection due to the known force and the variance in the deflection readings, respectively.

The given force, or control weight, also had uncertainty in its magnitude requiring quantification. The scale used to acquire the masses of the calibration weights had an absolute uncertainty of $\pm 0.00005 \text{ g}$. Although the absolute uncertainty was known, the distance data points taken by the sensor were a collection of points instead of a single value like the mass of an object. Therefore, it was more appropriate to relate the

uncertainty of the object's weight to its standard deviation for similar comparison to the uncertainty of the distance readings. Converting the uncertainty to a deviation was accomplished by assuming the mass had a two-thirds, or one standard deviation, probability of enclosing the actual value with a rectangular probability distribution. This assumption allowed for the uncertainty limits, or standard deviation, of $\pm (2/3) \delta_{mass}$ and hence $\pm (2/3) \delta_{Weight}$ where the operator δ represents the difference of the quantity.

An important part of generating a meaningful calibration curve is the statistical analysis. The calibration curve would be used to calculate the force from the thruster given the sensor distance measurements. However, the thrust is not a continuum, the averaged thrust is a result of thousands of droplets colliding with the catcher plate. Thus, the uncertainty in the thrust measurement system was translated to an uncertainty in the number of droplets in the thruster's flowfield. The overall thrust was decomposed by analyzing the thrust per droplet in the colloid thruster's exhaust plume. An electric field is created by the accelerating voltage across the extraction zone in the colloid thruster. Coulomb's Law, Equation (1), provides an approximation of the thrust acting on each droplet with an individual charge, q_d , within the electric field, \vec{E} . However, the summation of all the charges in the flowfield per time is the beam current, shown in Equation (23). Thus, a generic electric field variable can be related to the thrust by Equation (39), where F is the total thrust, E_{gen} is the approximated electric field acting on the charged droplets, and I_b is the total beam current.

$$F = E_{gen} I_b \quad (39)$$

The electric field strength can be extracted by varying the flow rate, calculating the beam current and thrust, and then using Equation (39) to obtain the electric field as a function of thrust and beam current. Subsequently, when completing the theoretical analysis for the variable number of emission sites, the number of droplets equaling the uncertainty of the thrust was calculated by dividing the thrust by the electric field and droplet charge. The droplet analysis gave an indication of how great an impact the uncertainty would have on the results.

This concludes the discussion on the methodology used for the thrust measuring experiment. The details of the system's hardware and theory were discussed, followed by a discussion in uncertainty and statistical analysis. A step forward in understanding and characterizing the thruster operating regime will be provided by the direct measurement of thrust.

3.6 Exit Velocity Measurement

The second experiment was designed to track the exhaust plume particles through image sequences and resolve their velocity through image analysis. The colloid thruster's specific impulse is directly related to the exit velocity of the exhaust droplets. Therefore, together with the thrust experiment, this testing would help determine the thruster's operational envelope. However, the actual experiments performed used a representative flow instead of the colloid thruster when the thruster became inoperable. A Carbon Dioxide (CO₂) dewar exhaust simulated the colloid thruster droplets in the flowfield to determine the accuracy of the code and generalize the tracking methodology of the colloid thruster's exhaust. As it would relate to the thruster, the experimental

process and methodology were analyzed. The experiment consisted of illuminating the exhaust plume with a thin laser sheet and tracking the trajectory of each particle through a series of high speed camera images. An experimental schematic is shown in Figure 19 where the camera is directed into the page, nearly perpendicular to the CO₂ exhaust flow.

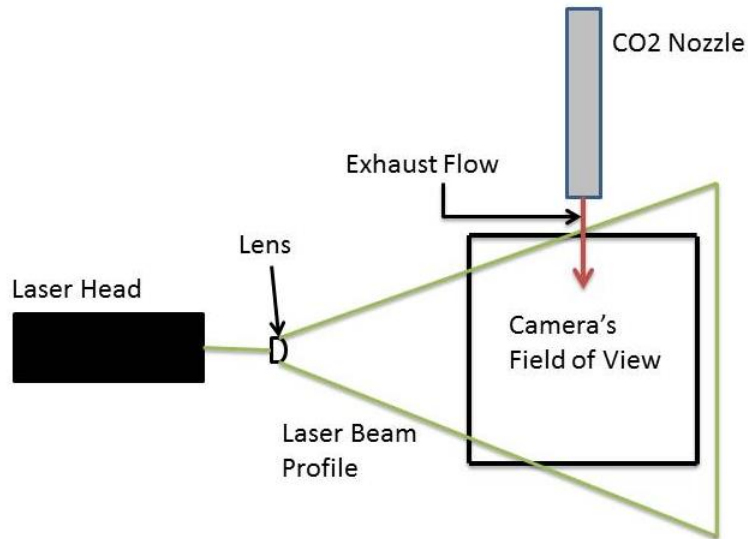


Figure 19. One-dimensional schematic diagram of the exit velocity experiment. A camera is aimed perpendicular to the page and only its representative field of view is shown.

Two camera exposure times, $20\ \mu\text{s}$ and $500\ \mu\text{s}$, were used when imaging the droplets. The image sequences of the two different exposure times were post-processed to determine the stream-wise mean particle velocity. Image sequences with the fast exposure time, $20\ \mu\text{s}$, were cross correlated to find the distance traveled by a particle from one frame to the next. Image series with the slow exposure time, $500\ \mu\text{s}$, had each frame analyzed individually to find the length of the particle's streak pattern during the exposure time.

A benefit of this experiment was the limited number of laboratory components required for testing. However, the few necessary pieces of equipment were critical to the experiment's success, the first being the laser. The laser used for this experiment was the Coherent Verdi 5. This is a continuous wave laser with an adjustable power output with a maximum of 5 Watts. It is a Neodymium-doped yttrium orthovanadate (Nd:YV04) type laser operating at a wavelength of 532 nm with a diameter of $2.25 \text{ mm} \pm 10\%$ spherical beam [30]. A separate power control unit and water cooling system were used in conjunction with the laser head. Figure 20 shows the laser head, operating unit, and cooling component.



Figure 20. Coherent Verdi 5 laser head (Top), power operating unit (lower left), and cooling unit (lower right) used to illuminate the flowfield during the exit velocity experiments.

The light emitted from the laser had to be shifted from a cylindrical beam into a one-dimensional flat sheet in order to get a planar view of the flowfield. The best practice for creating a flat sheet of laser light is with a cylindrical lens, either plano-concave or plano-convex. Simplified geometrical optics theory was used to estimate the required lens parameters for this experiment. A representation of a light path through the lens as it relates to the geometrical theory is presented in Figure 21.

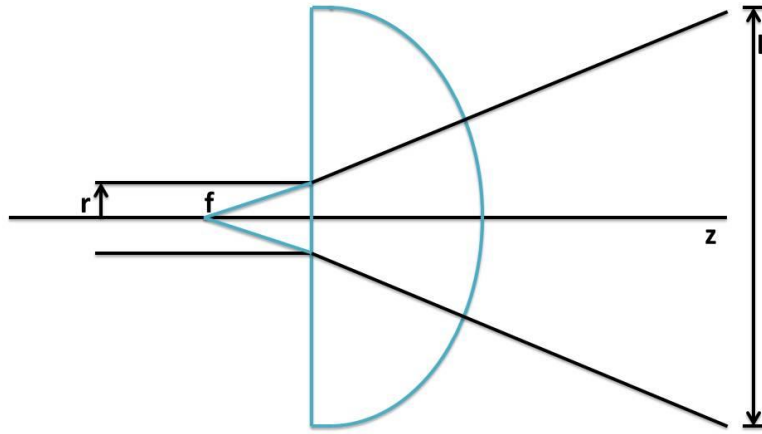


Figure 21. Geometrical ray trace of a plano-convex lens illustrating how a small laser beam is spread into a thin sheet of light.

If the focal length, f , of the lens is known, then the length L_{las} of the laser sheet at a distance z away from the lens is given by Equation (40), where r_{las} is the radius of the incoming beam [41].

$$L_{las} = 2(r_{las}/f)(z + f) \quad (40)$$

Constraints for the lengths z and L_{las} were imposed by the vacuum chamber. The lens was placed inside the chamber and the exhaust flow was imaged nearly perpendicular to the laser sheet. The near-perpendicular requirement forced the thruster to be placed in the middle of the chamber, imposing a maximum to the z distance of 12 inches. Therefore, the laser sheet spread from the cylindrical lens to the emitter grid. A third constraint was created by the vacuum chamber window size. The camera viewed the flow through one of the small window ports on the bottom of the chamber. The diameter of the port is fixed and created a constraint on the camera's field of view of approximately 10 inches. This constraint meant the laser sheet length, L_{las} had a maximum of 10 inches. The laser beam radius was set by the laser specification at 1.13 mm. The only remaining unknown in Equation (40) was the focal length of the lens. Solving Equation (40) with the constrained values resulted in the lens requiring a focal length of about 3 mm. However, due to limited mass market availability and high cost of specialized lens manufacturing, a lens of focal length 4 mm was used instead. This focal length was close enough to the optimum focal length to provide the required effect on the laser sheet. The ThorLabs cylindrical lens LJ1310L1-A was the final beam-spreading optic utilized.

The last essential devices required in the experiment were the imaging system components. Flowfield images were captured by the Phantom v12.1. The Phantom is a high-speed, variable resolution camera with the ability to capture images with an exposure time as small as $0.2 \mu s$. It provides 8 bit grayscale images in a variety of image formats.

It was desired to have the camera as close to the chamber as possible to obtain the largest field of view through the window port. Standard lenses have a large focal length, therefore requiring a camera placement further from the port than desired. In order for the camera to be placed directly outside the chamber, a focal length of around 12 inches would be needed to focus in the laser sheet plane. However, this focal length is less than the minimum length of most lenses. The problem of the short focal length was overcome by using a macro lens. The macro lens paired with the Phantom camera was the Sigma DG Macro 24mm F1.8 lens. Its focal length is 24 mm and minimum f/# is 1.8.

The Phantom v12.1 camera was combined with the Sigma Macro lens to produce the required images with a 12 inch focal length and a resolution of 512 by 512 pixels. The USAF 1951 resolution target was again used to determine the camera's resolution in pixel per true distance for this imaging setup, in the same manner as with the emitter head imaging. Before this experimental setup was used with the thruster, a test setup verified the fidelity of the system.

A (CO₂) dewar provided a stream of particles into the image capturing area representative of the colloid thruster droplets. After taking images of the CO₂ particles, comparisons were drawn to how the imaging system would perform with colloid thruster particles. A CO₂ dewar is a container storing liquefied CO₂ at cryogenic temperatures. An expansion nozzle can be connected to the dewar to draw out the liquid. As the liquid moves through the nozzle, it begins to evaporate and cool. This cooling decreases the remaining liquid's temperature, in turn freezing it into solid particles. The discrete solid particles are ejected from the nozzle with a range of mean diameters on the order of 5 to 15 μm [31]. The size of these particles was larger than what would be expected from the

colloid thruster, but they were an appropriate representation of the types of expected discrete particles. In order to eject the CO₂ particles in the laser sheet path, a hose was connected to the dewar and passed through an open port on the vacuum chamber wall. The hose then ran up the side of the chamber and a nozzle attached to the end of the hose was fixed in the plane of the laser sheet directly above the camera's field of view. The nozzle aimed vertically down toward the bottom of the vacuum chamber. Figure 22 displays the complete experimental setup.

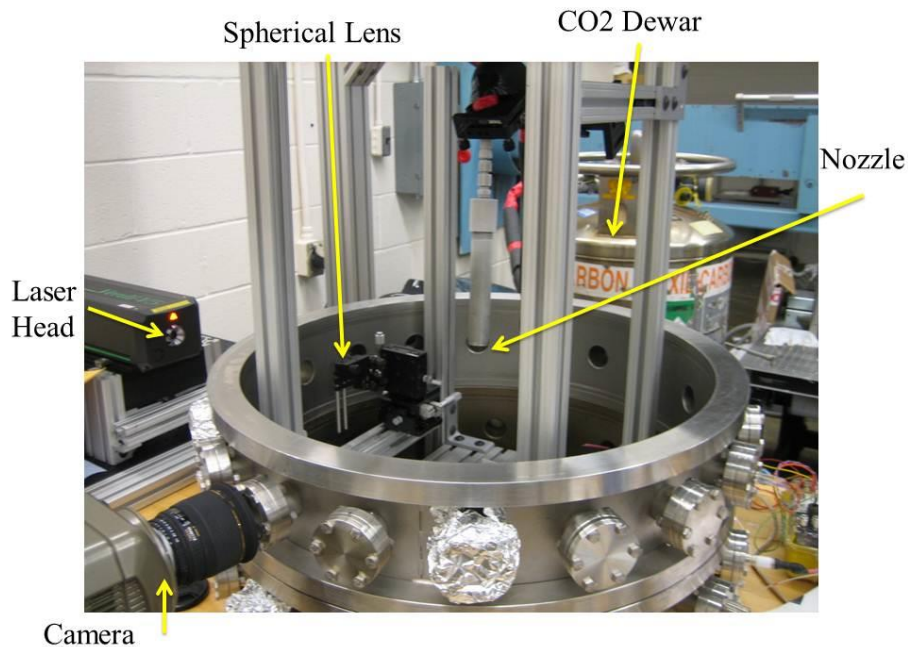


Figure 22. Actual experimental setup for the particle flowfield tracking experiment.

For a meaningful experimental comparison, the CO₂ dewar exhaust had to be representative of the expected colloid thruster exhaust characteristics. An important aspect in comparing the flowfield from the CO₂ dewar to the probable flowfield from the thruster was the relative length of time the particles were being captured by the camera.

When imaging each field the velocity of the thruster particles would be much greater than the CO₂ particles so the exposure times and frame rates should be adjusted accordingly.

The nominal specific impulse range of the thruster is between 400 and 1300 s [7]. Using Equation (18), the specific impulse span corresponds to an exit velocity range of approximately 4000.0 to 13000.0 m/s. The image resolution of the setup was determined to be 4480 pixels/m by using the USAF 1951 resolution target. This resolution converted the thruster's velocity range from m/s to pixel/s. The definition of velocity as distance per time was used to calculate the average time for a particle to traverse the camera's 512 pixel resolution. This average time was 9 to 28 μ s. Even though the optimal time was 9 μ s, the Phantom camera has an 8 μ s exposure time which was considered close enough, for the purposes of this experiment, to the time for the particle to move across the imaging plane. A total distance traveled by the droplet in 8 μ s was obtained by multiplying the 8 μ s exposure time by the velocity.

Using Bernoulli's Equation with a stagnant flow, Equation (41), where v_{CO_2} is the velocity of the CO₂ particles, P_t is the pressure inside the CO₂ dewar, P_∞ is the atmospheric pressure, and ρ_∞ is the density of the CO₂ particles at atmospheric pressure the estimated velocity of the CO₂ particles was obtained [5].

$$v_{CO_2} = \sqrt{\frac{2(P_t - P_\infty)}{\rho_\infty}} \quad (41)$$

The approximate distance a colloid thruster particle would travel during the exposure time was divided by the estimated velocity of the CO₂ particles. The resulting time was the exposure time required to image the CO₂ particles traveling a distance equal to the

colloid droplets. The approximate similarity exposure time was $582 \mu\text{s}$. However, the closest exposure time on the Phantom was $500 \mu\text{s}$, so this exposure time became the long exposure time to capture a streak of a CO₂ particle across the image plane.

It was necessary to also find the similar short exposure time for the CO₂ particles. The shortest exposure time on the Phantom was $0.285 \mu\text{s}$. The velocity of the thruster's particles at their slowest rate is approximately 4000.0 m/s . This velocity was multiplied by the $0.285 \mu\text{s}$ exposure time to obtain the distance a droplet would travel during the exposure time. This distance was then divided by the CO₂ velocity of 55.0 m/s to find the similar exposure time. The similar exposure time was approximately $21 \mu\text{s}$. The closest exposure time on the Phantom was $20 \mu\text{s}$, so this became the short exposure time. Multiple trials were performed to capture the flowfield from the CO₂ dewar using the long and short exposure times.

An algorithm was created and implemented in MATLAB to analyze the flowfield and post-process the image sequences to extract the particle velocities. Since two different exposure times captured the images, two different algorithms were created to estimate the velocities. The two algorithms are discussed next, beginning with the short exposure time algorithm. Reference images were taken at the beginning of every image set to remove any systematic irregularities in each image.

The short exposure program began by importing the reference images and finding a mean value of each pixel as its reference state. Then, the flowfield images were imported and each value of the image pixel intensity was mathematically subtracted from its reference counterpart. This ensured the resulting set of pixel intensities had any

abnormalities removed. Next, the program iterated through the images and with the function *graythresh* filtered out any background light to ensure only the light from the illuminated particles was present. Then the area and equivalent circular diameter of each particle were calculated using the *regionprops* function. If the area of the particle was greater than a minimum level set by the user, the image was cropped around the particle with square dimensions of the equivalent circular diameter. The cropped image became the template for the image correlation. The normalized two-dimension cross correlation function *normxcorr2* was used to cross-correlate the template with the next image in the original image sequence. How far the particle had moved was indicated by the *normxcorr2* function locating the point in the image with the greatest correlation to the template. The distance of the particle from the first to the second image was calculated and this corresponded to the distance traveled between the picture frames. The distance was divided by the time between pictures to provide the velocity of the particle.

A mean result was generated by combining the results of the particle cross-correlation between two successive images. For instance, each particle had a given velocity computed between two images. The standard errors of the correlation and velocity of each image pair was calculated to gauge the accuracy of the results. The most important feature of this code was the cross correlation between images. On the other hand, the long exposure algorithm analyzed each frame individually to extract the velocity.

The algorithm for the long exposure began similarly to the short exposure algorithm by importing the image set, subtracting the reference images, then converting each image to binary. Next, the mean particle area and major axis length were calculated

using the *regionprops* function. The program then looked for any particle area greater than a given magnitude specified by the user. When the program located a particle with this area, it stored the particle's major axis length. The major axis length divided by the exposure time equaled the particle's velocity. All of the velocities were averaged together and standard errors based on those averages were calculated.

This concludes the discussion of the methodology for the second experiment. The experiment was performed to image illuminated particles in a flowfield and extract their velocity from analyzing those images and image sequences. Image correlation and smear tracking methods were used with fast and slow exposure times, respectively, to obtain the particles' average velocity.

3.7 Taylor Cone Formation

Viewing the Taylor Cone formation on a single emitter head at various propellant flow rates was the objective of the final experiment. Busek's hypothesis can be summarized as the Taylor Cone formation and number of emitter sites show different characteristics through the range of three different propellant flow rates. The low flow operation is less than 0.5μ Liters per minute. The moderate flow range is from 0.5 to 5.0μ Liters per minute. The high flow rate range is greater than 5.0μ Liters per minute. Each of these flow rates has a corresponding theoretical Taylor Cone formation profile [14]. The hypothetical description of the Taylor Cone number and size, dependent on the flow rate, was described in Chapter two. The purpose of this experiment was to image the Taylor Cone formation in each of these flow rate phases, then analyze the cone

geometry and number density across the emitter. This section describes the equipment and methodology of this experiment, starting with the imaging system.

Two overall requirements were set for the imaging system. A fast camera frame rate to capture the sub-millisecond progression of the Taylor Cone was the first requirement. The second requirement was for a telescoping lens to magnify the emitter surface. A Questar QM100 telescope was the solution to the telescoping lens.

A magnification device had to be used to view the Taylor Cones because the image scale of the cone formation is on the micron level. This makes the cones smaller than can be perceived by the human eye, or any non-telescoping lens, alone. Therefore, the Questar QM100 long distance microscope, shown in Figure 23, was used to magnify the images.

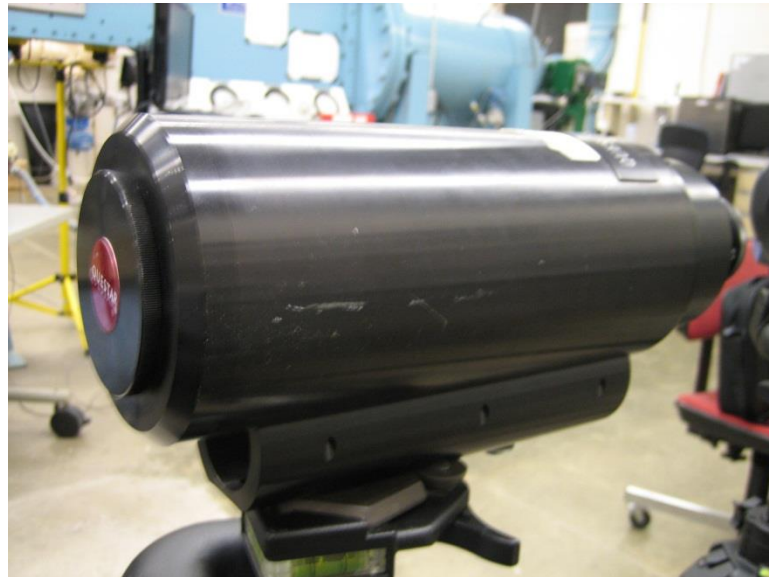


Figure 23. Questar QM100 long distance microscope used to view the Taylor Cone formation during thruster operation.

This microscope has a working distance range of 15 to 35 cm, with magnification ranging from 3.43X to 8.13X, respectively and an optical resolution of $1.1\ \mu\text{m}$ at 15 cm [47].

The Questar and camera are not vacuum rated so they remained outside the vacuum chamber during testing. Due to optical path constraints from focusing the light source, discussed later in this section, the final distance from the emitter head to the telescope was approximately 11 inches resulting in an optical resolution of approximately $2\ \mu\text{m}$.

The Shimadzu HPV-2 is a high speed camera system capable of a $1\ \mu\text{s}$ exposure time with a 1 million frame per second sampling rate. Exposure times vary from 33 ms to $1\ \mu\text{s}$ in doubling increments (2 ms, 4 ms, 8 ms, etc). Figure 24 shows the camera without a lens.

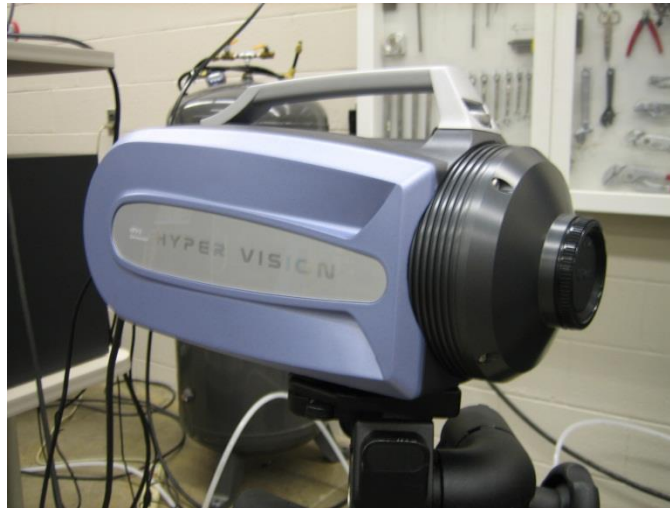


Figure 24. Shimadzu HPV-2 high speed camera used to image Taylor Cone formation.

The imaging device is a Charged Coupled Device (CCD) sensor and the camera uses an internal cooling system to keep the electronics from overheating. The resolution is 312 x 360 pixels with a 10 bit monochrome color map. Due to the size of the camera's internal

memory, a maximum of 100 frames at a time can be obtained during each recording session. The camera interfaces with proprietary software to provide the images. The combined camera and microscope system were connected with a Nikon F-series mount and the system is shown in Figure 25.

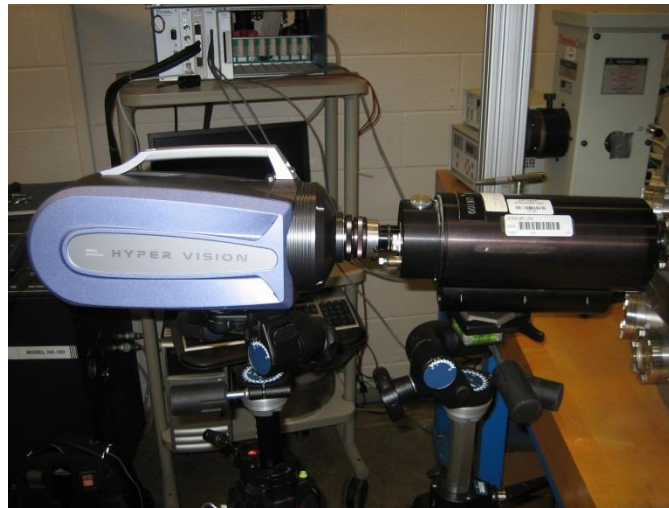


Figure 25. Shimadzu HPV-2 camera connected to Questar QM100 microscope. The connection completes the Taylor Cone imaging system.

A camera's exposure time corresponds to how long the camera's shutter is open and actively absorbing light to capture the image. A fast exposure time means there is less opportunity for light to enter the camera lens and a darker picture will result. Hence, the fast exposure time of $1 \mu\text{s}$ means the image subject must be extremely bright for a well-lit image. There are no lights inside the bell vacuum chamber so an external light source had to be used to illuminate the emitter head.

A Thermo Oriel Arc lamp provided illumination on the emitter head inside the bell chamber. A Xenon arc source is used by the Arc lamp and has a maximum power of

1000 W. The lamp is powered by a Spectra-Physics 69920 power supply. Figure 26 displays the Arc lamp and power supply.



Figure 26. Arc lamp (right) and power supply (left) used to illuminate the emitter head when attempting to view Taylor Cone formation.

The Arc lamp intensity was controlled by setting the amperage on the power supply. While performing the experiments, the amperage was set to the maximum value of 48 A. This corresponds to the lamp's 1000 W maximum. Even at the maximum power, the arc lamp could not produce enough light on the emitter for the camera to capture an illuminated image with a sub-millisecond exposure time. Therefore, an optical system used formed to focus the light onto the emitter.

The optical light focusing system consisted of a series of Thorlabs mirrors and lenses; 2 plane mirrors and 2 plano-convex lenses. The Arc lamp was positioned outside the vacuum chamber so light entered the chamber through a small window port on the side wall of the chamber. After the light entered the chamber, a 2 inch diameter, 125 mm focal length plano-convex lens focused the collimated light down to a near point. Then, a

1 inch diameter circular plane mirror redirected the light upward along the height of the chamber. Next, a 4 inch x 5 inch rectangular mirror reflected the light at a slight angle back down toward the thruster emitter head. The second mirror was larger than the first to collect all of the light spread from the first mirror. After the second mirror, another 3 inch diameter plano-convex lens focused the light onto the emitter surface. The optic system described above is shown in Figure 27.

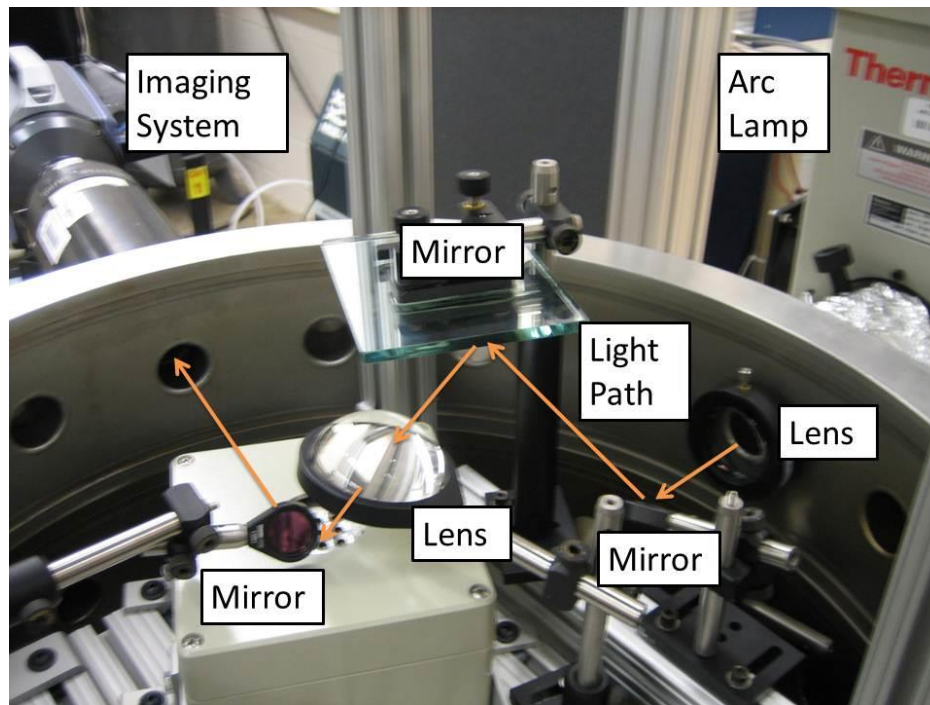


Figure 27. Optical system used to focus light from the arc lamp onto an emitter head.

A single 1 inch diameter mirror was placed directly above the emitter head at an angle with respect to the emitter in order to reflect the vertical image into the horizontal microscope/camera assembly. Available thruster locations inside the vacuum chamber were constrained by this additional mirror. The focusing system was the reason the

thruster was not placed at the minimum distance from the QM100 microscope to get the smallest resolution possible. This concludes the equipment necessary to image the Taylor Cone formation on the emitter head to complete the third objective.

3.8 Summary

This chapter described the methodology and equipment used when performing the research of this thesis. The procedure for imaging the emitter heads and estimating the number of emitter locations was described. Next, the experimental processes implemented to measure the thrust and droplet exit velocity were reviewed. An overview was given regarding the approach taken to image the Taylor Cone formation during thruster operation. Finally, colloid thruster issues were touched upon. Chapter four provides the results and discussion from executing the methods described in this chapter.

IV. Analysis and Results

Chapter four provides the results as well as a discussion of implementing the procedures presented in Chapter three. Results from the theoretical study of the emitter head are presented first. Second, results from operating the distance sensor to obtain a system calibration curve and error estimations are shown. Third, results from the exit velocity determination of the CO₂ particles are reviewed. Fourth, discussion and results from the Taylor Cone imaging experiments are given. Last, a review of the thruster's operation is discussed.

4.1 Emitter Number Range Development

Emitter head images were obtained and processed as described in Chapter three. The need for localized thresholding to find the maximum number of emitter sites is apparent from Figure 28.

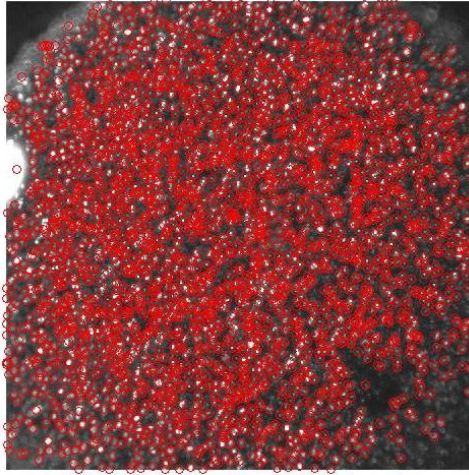


Figure 28. Processed image from the emitter site estimation algorithm highlighting the negative results of global thresholding over the emitter head such as oversaturation in some areas and under estimation in other areas.

When global thresholding was applied to the emitter head image, the center of each possible emission site can be seen in Figure 28 as the red circles. There are no shown emitter sites in the area in the bottom right corner of the figure. However, emitter sites will most likely occur in the area even though it is dark compared to the rest of the image. Using a localized filter to threshold the image for bright intensities resolves this problem. Another problem seen in Figure 28 is how many of the emitter points are overexposed. Overexposure on one pixel can bleed over to another pixel in an image. Therefore, the number of possible emitter sites is considered a maximum due to these bleed over pixels counted as emitter sites by the MATLAB algorithm. Final results from the developed program are shown in Table 2.

Table 2. Final results from algorithm computing number of emitter sites based on microscope images

Flow Rate Condition	Mean Number of Emitter Sites (Unitless)	Standard Error	Standard Error Percentage of Mean
Minimum	10100	154	1.5
Maximum	3700	503	13.6

There is an error of 2% for the maximum number of emitter sites instead of the 14% error from the minimum number of sites. This result was expected because the lower error is likely a consequence of many more sample points in the population. A more discrete method of selecting the likely emitter points was used for the minimum flow rate algorithm whereas the maximum flow rate algorithm had more variability with its global threshold.

Results from each image filter used to count the number of possible emitter sites in a local area in the minimum flow analysis were extrapolated to the actual area of the

emitter head. This was performed as a check to ensure the number of emitter sites across the head was uniform and there were no local areas around the head with an extreme number of potential sites. Histograms of eight emitter heads are shown in Figure 29 where the x-axis represents the extrapolated number of possible emitter sites and the y-axis is the total number of local image filters containing the extrapolated value.

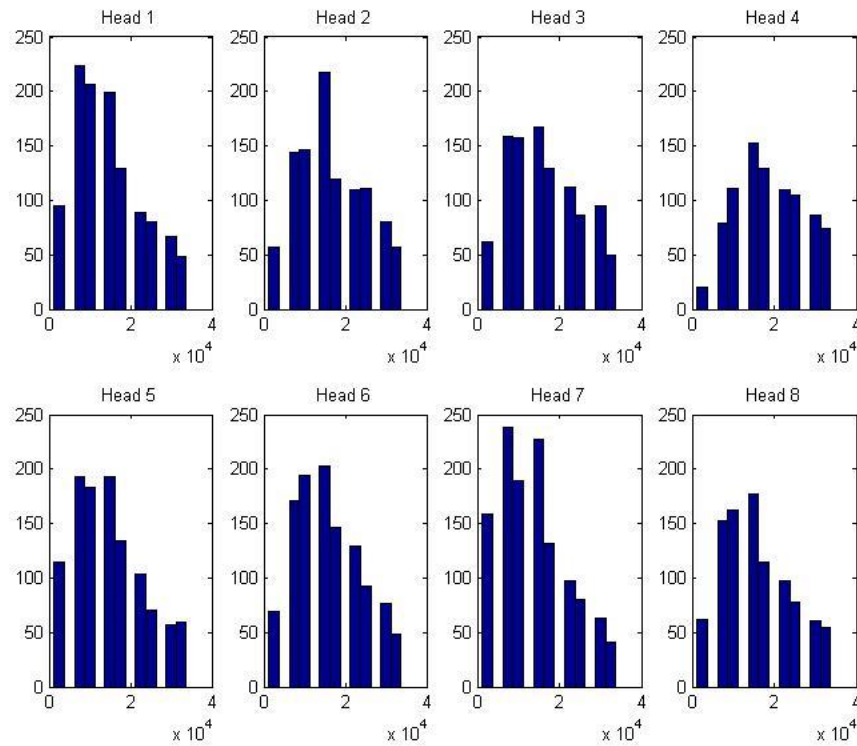


Figure 29. Histograms of the maximum number of emitter sites extrapolated from each local filter over the first eight heads.

The histograms in Figure 29 show how the local filters have a relatively parabolic distribution of extrapolated emitter points. This suggests the filter algorithm was

successful in determining localized emitter sites around the entire head. Table 3 shows the mean and standard error of the extrapolated number of emitter sites on each head.

Table 3. Statistics for the extrapolated number of emitter points

Emitter Head	Mean Extrapolated Number (Unitless)	Standard Error of Mean
1	15,400	243
2	17,400	256
3	17,100	264
4	19,500	276
5	15,500	252
6	16,600	239
7	14,600	233
8	16,600	268
9	15,900	265

Analysis of Table 3 reveals the mean number of extrapolated emitter locations is as much as 190% higher than the result of adding each filter together and extrapolating the combined sum to fit the actual emitter head area. This is attributed to the large difference between the area of each filter and the area of the emitter head. The filter area is around 2% of the emitter head area. Checking for extreme values or skewed data was the main goal of using the extrapolation points. Since there were no signs of distorted data or irregularities, the extrapolation checks helped defend the estimated number of maximum emitter sites.

Capturing magnified emitter surface images revealed many traits not apparent on a larger scale. These characteristics may have an adverse effect on the number and location of the emission sites; however, no proof has been acquired. Therefore, only observations and possible causes and effects are addressed, but only in a qualitative nature.

Discoloration on the head is the first irregularity. Examples of discoloration are shown in Figure 30.

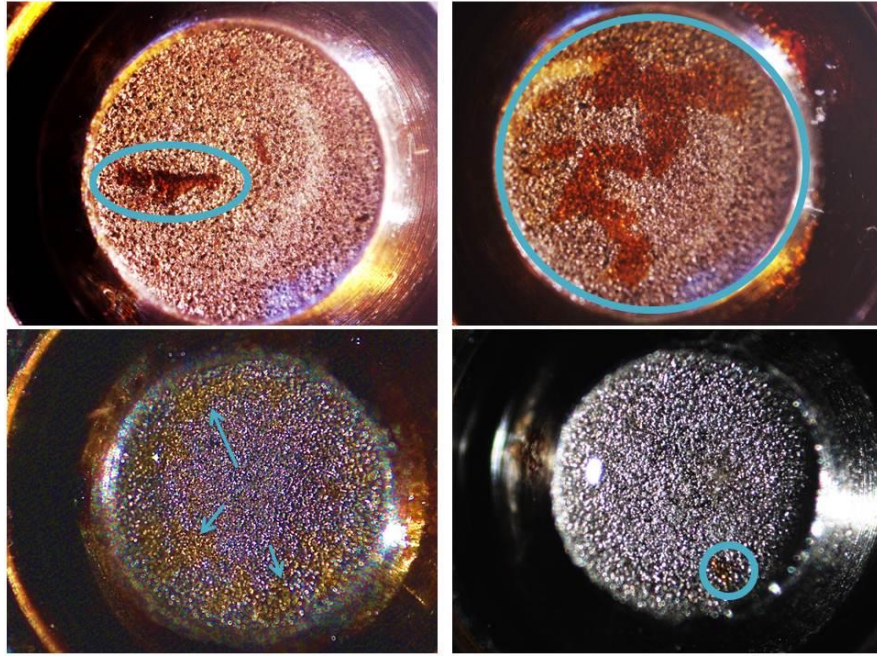


Figure 30. Emitter head images highlighting surface discolorations.

Figure 30 displays various discoloration patterns on different emitter heads. Blue outlines and arrows highlight the locations. Discoloration in a dark red or rusty color is consistent among the marked locations. However, the shape and sizes have a wide variation. A relatively small, localized spot is shown in the lower right figure, while the upper right figure is stained across most of the emitter. Also, the locations along the head are varied. The upper left picture shows a streak mainly in the center of the emitter while the lower left image has markings around the perimeter.

Two possible reasons for the discolorations can be readily concluded. The first reason could be the presence of burnt propellant on the emitter head. If the propellant

impinges on the extractor grid and electrically burns, it may fall back onto the emitter head and burn onto the surface. Electrical arcing is the second possible cause of the staining. The emitter head may have arced with the extractor grid or with the propellant itself. Extremely small gaps could exist between the emitter head and propellant when the propellant reaches the emitter head surface. Small arcs could occur and over time produce a burnt pattern on the porous surface. The staining is enough to change the color of the emitter head or have extra propellant particles on the head so it may change the electrical properties or block the propellant from emitting in a certain location. Future work could be done to more fully understand the effects of the discoloration across the emitter heads.

Another random unevenness seen on the emitter head appears to be the metal on the surface having fused together in localized areas. An example is shown in Figure 31. A highlighted circle encloses an example of what seems to be metal fused together on the emitter head. The localized region has a high glossy appearance with a relative decrease in shallow areas where the propellant flows. Metal particles are fused together through the sintering process and particles on the surface may fuse together locally. This metal fusing will block the propellant rising from these areas and create a strong electric field across the fused area. Even distribution of emitter sites across the head may be restricted by the fused areas. If the emitter sites are not evenly distributed across the head, experiment repeatability may be restricted during thruster operation because the fused areas give more randomness to where and how the Taylor Cones form. Discoloration and apparent fusion are localized observations, but they may affect the emitter site locations and thruster properties.

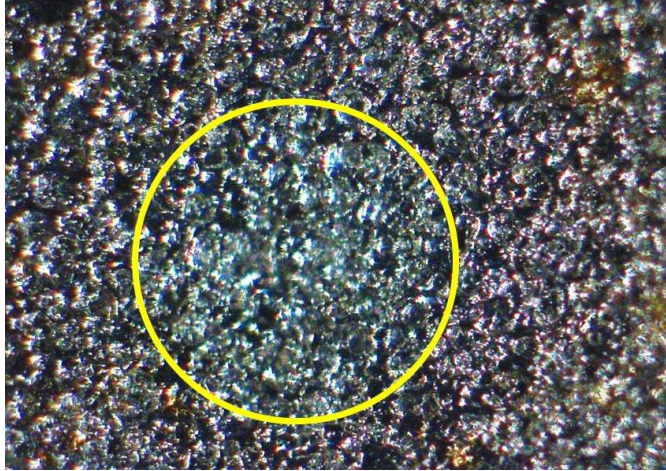


Figure 31. Emitter head surface fusing example with the fused area highlighted.

Large altitude gradients along the surface were discussed in detail in Chapter three. The centers of the emitter heads are more shallow and farther from the extractor grid than the outside perimeter. This affects the Taylor Cone distribution because the propellant will reach the center surface quicker than the edges, but the field strength at the edges will be slightly higher since they are closer to the extractor grid. The exact interaction between these two differences is unknown, but estimated to make more Taylor Cones appear in the center instead of around the perimeter.

Hilly plateaus on the terrain instead of mountainous peaks are the final aspect of the overall emitter head worth mentioning. Before imaging the heads, localized peaks on the surface similar to steep mountain ranges were believed to exist. The emitter heads were imaged at a 30 degree angle and one result is shown in Figure 32.

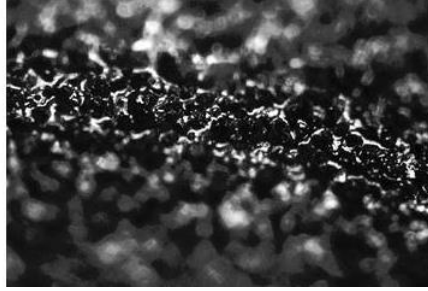


Figure 32. Emitter head image on a 30 degree angle displaying the profile along the porous head.

Figure 32 shows topography of flat rolling plateaus as opposed to discrete peaks. The electric field on the surface will not have much variability in the absence of peaks. This means the propellant may have a larger range of emitter spots during the low flow rate condition. Without prominent peaks, the emitter locations will have a great deal of variation. Variation in emitter sites erodes the repeatability of the emitter head to reproduce similar Taylor Cone patterns for a given flow rate.

Broad observations about the emitter heads have been discussed. These have been qualitative assessments, therefore, only estimates of their causes and consequences have been given. Now quantitative results and discussion are provided regarding the emitter head.

4.2 Theoretical Performance

Determining the unknown parameter, ψ , was the next task in developing the theoretical characteristics. This variable enabled the calculations of the thruster specifications assuming a constant number of droplets released per second. The constant

droplet calculations provided a baseline to compare the results to the theory of a variable number of emission sites.

Calculations of the relevant colloid thruster parameters were performed by varying the volumetric flow rate and setting the theoretical parameter constant at 163.48. A number of comparisons between the two droplet release rate assumptions, constant and variable, were made. When the droplet amount was held constant, it was the last variable calculated and all other variables scaled accordingly without affecting this parameter. On the other hand, when the number of sites was an input into the calculations, the other parameters were driven by this constraint. However, the beam current, thrust, specific charge, and specific impulse were equal in both cases because they were calculated independently of the number of emitter sites. They were calculated solely as a function of propellant electrochemical properties, beam current, beam voltage, and volumetric flowrate. Beam current and thrust results are shown in Figure 33.

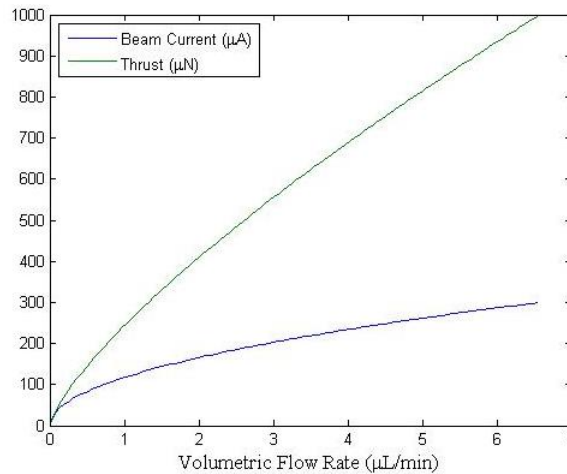


Figure 33. Theoretical beam current and thrust varying with volumetric flow rate.

Thrust varies proportionally with beam current; hence, the plots in Figure 33 show the expected relationship. The maximum values of thrust and current are the maximum stated for the thruster, 1 mN and $300\ \mu\text{A}$.

The charge-to-mass ratio of the colloid thruster is directly proportional to the beam current and inversely proportional to the thrust and flow rate. Figure 34 displays the charge-to-mass ratio as a function of flow rate.

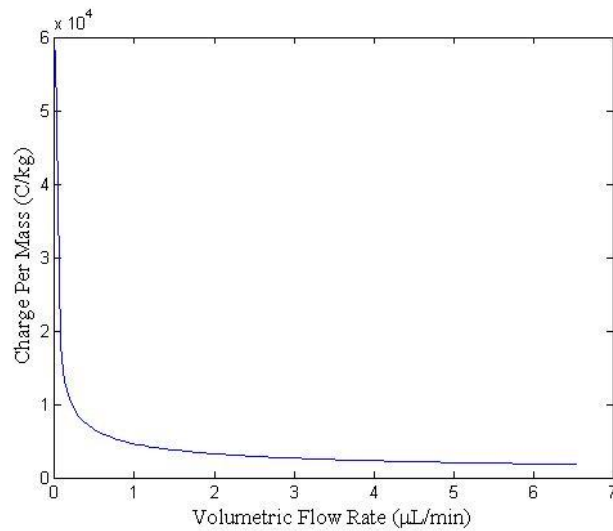


Figure 34. Theoretical specific charge as a function of volumetric flow rate.

A direct relationship exists between the specific impulse and the charge-to-mass ratio. By setting the accelerating voltage to a constant value, the specific impulse directly correlates with the charge-to-mass ratio. Figure 35 shows the specific impulse performance curve.

Busek Co. Inc. advertises an operating specific impulse range for the colloid thruster from 400 s to over 1300 s [7]. The location of the 1300 s specific impulse is

highlighted in Figure 35. Specific impulse values outside of the advertised limits are present on the curve in Figure 35.

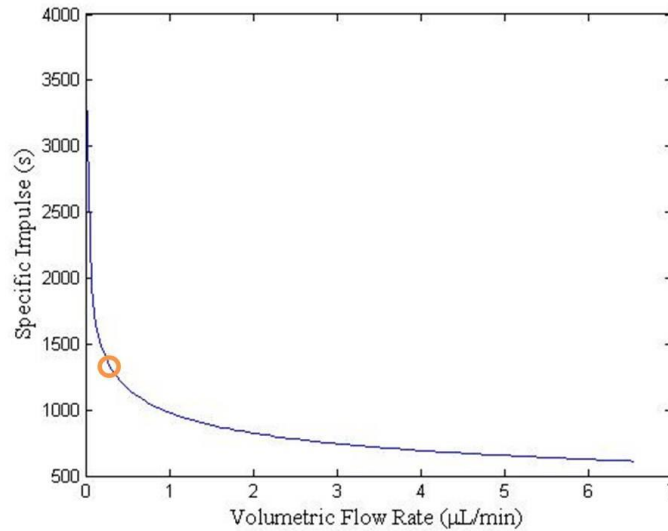


Figure 35. Theoretical specific impulse as a function of volumetric flow rate.

During low flow rate, there is a physical limit to how slowly the propellant flows through the emitter. When the volumetric flow rate approaches zero, the curve in Figure 35 moves to a vertical asymptote. This asymptote represents an infinite specific impulse and is a purely mathematical event. Based on the Busek specific impulse specifications, the minimum flow rate in the thruster is approximately 0.3 micro-Liter/minute. On the high end of the flow rate, the thrust is at a maximum of 1 mN and Figure 35 shows the specific impulse is approximately 600 s. This value is 200 s above the given specification of 400 s, a 50% increase. Two assumptions are attributed to the increase, perfect thruster efficiency and a constant theoretical function. Perfect thruster efficiency was assumed during the calculations to obtain these results. However, many performance aspects of colloid thrusters carry an efficiency decrease reducing the theoretical specific

impulse. Electrical efficiency decreases are dominated by Taylor Cone formation but other sources of efficiency decreases are present as well, such as exhaust plume polydispersion and divergence, as described in Chapter two. Also, as discussed in Chapter three, the theoretical parameter is assumed constant during the calculations, but the dielectric constant and experimental factor are strong functions of temperature and are not constant during thruster operation. The temperature dependencies of these factors will further reduce the theoretical specific impulse. Therefore, a theoretical specific impulse of 600 s is plausible when compared to the operationally measured 400 s. In addition to the overall thruster characteristics of beam current, thrust, and specific impulse, the droplet characteristics are important as well.

The foundation of the theoretical performance specification is the variable number of emitter sites since the number of released droplets helps determine the individual droplet properties. Thus, the droplet specifications will be different depending on how the droplet rates are specified. A constant number of emitter sites are assumed in the baseline model. Alternatively the model developed as part of this thesis assumes a linear decrease in emitter sites with propellant flow rate. There is a direct relationship between the number of emitter sites and the number of drops released per second. Figure 36 shows the number of drops released per second as a function of flow rate. Consistent with the decreasing number of emitter sites, the variable emitter site data shows the decreasing number of drops released as the flow rate increases.

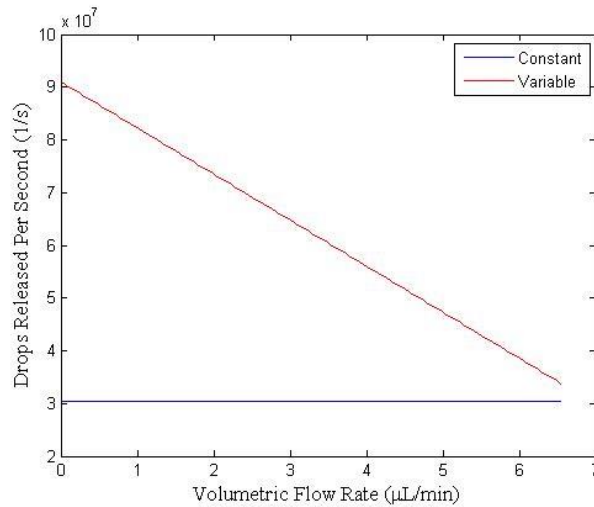


Figure 36. Number of droplets released per second as a function of volumetric flow rate for the constant droplet release rate and variable release rate theories.

The variable droplet release rate is on the same order of magnitude as the baseline constant release rate model. Calculating the droplet variables with an assumed constant droplet rate provided the optimized rate dependent on one situation, in this case, the maximum thrust condition. Values of the maximum thrust condition were used to calculate the theoretical parameter and in turn the droplet release rate needed for the specific case. Therefore, the closest droplet rate between the constant and variable cases is at the maximum thrust, or maximum flow rate, condition. This increases confidence in the model for the variable number of emission sites. There is a 10% difference between the droplet rates at the maximum thrust condition. A larger variable droplet release rate is present in the low flow rate case because the number of emitter sites was assumed to be larger. An increased number of sites correspond to a smaller droplet.

Droplet radius and mass increase as the mass flow rate is increased. Increased droplet size is necessary to increase the thrust output since the number of emitter sites is

decreasing. Figure 37 shows the droplet mass as a function of flow rate. Droplet mass increases linearly with increasing flow rate for the fixed droplet rate. This result is reasonably intuitive because as the flow rate incrementally increases, but the number of drops released remains the same, the increased mass flow distributes equally among the droplets thereby incrementally increasing their mass. This result is not the same with the variable droplet rate. In this case, the relationship between droplet mass and flow rate is more complex and interconnected with the droplet radius and charge.

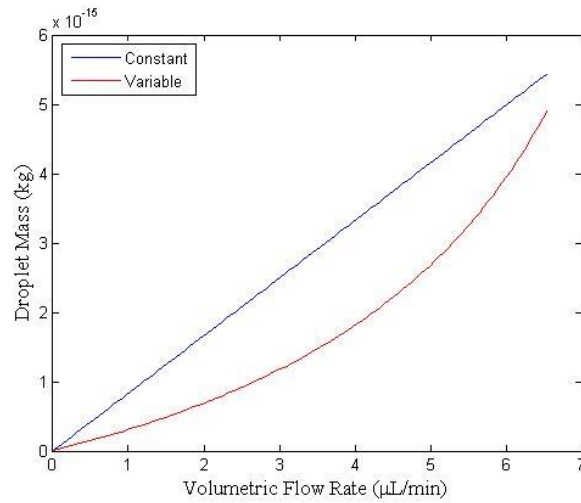


Figure 37. Droplet mass as a function of volumetric flow rate for the constant and variable droplet release rate cases.

Figure 38 displays the droplet radius response to the propellant flow rate. Both cases show a non-linear radius increase with increasing volumetric flow rate. A more gradual increase in the droplet radius is seen in the variable droplet release rate case because the radius is directly related to the droplet mass. The droplet radius and mass affect the droplet's charge through the charge-to-mass ratio.

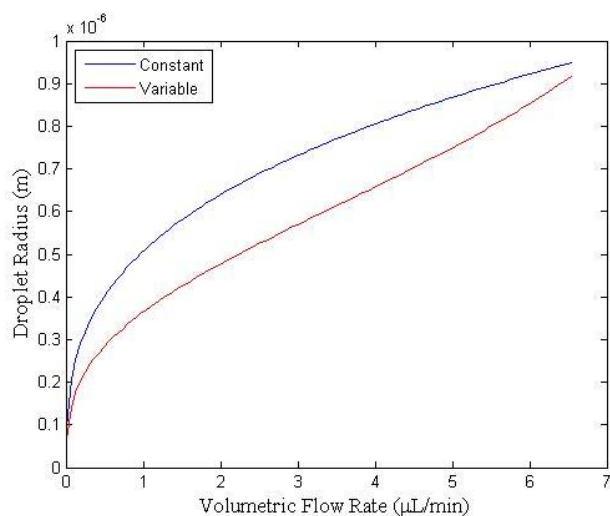


Figure 38. Theoretical droplet radius as a function of volumetric flow rate.

Figure 39 shows the droplet charge response as a function of flow rate and how the droplet charge displays a more gradual increase in the variable case than the constant case.

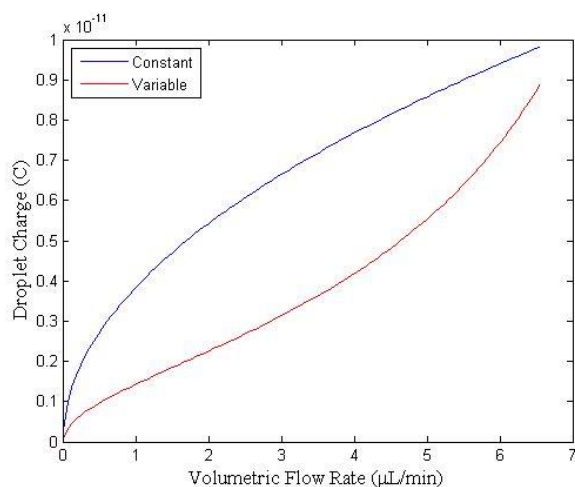


Figure 39. Theoretical droplet charge as a function of volumetric flow rate.

This is consistent with the mass and radius plots having a more gradual charge as well. Each plot shows how the orders of magnitude are on the same scale between the constant and variable droplet rate cases and the variable trends are similar. This supports the hypothesis for the expected number of emitter sites.

Results of the relevant colloid thruster parameters were discussed. Overall performance factors of thrust, beam current, and specific impulse were shown followed by droplet-specific variables of mass, cross-sectional radius, and charge. Since a baseline has been established for these variables, they were applied to the thrust and exit velocity experiments to determine their projected utility and usefulness.

4.3 Thrust experiment

In order to provide a dynamic response to the thruster from the colloid thruster, the cantilever beam and catcher plate needed to be tuned correctly. The system's linear response range needed to be in the full thrust range, from $1 \mu\text{N}$ to 1mN . Table 4 summarizes the final beam parameters, obtained through the Euler-Bernoulli equations, used during the system calibration.

Table 4. Final parameters used for the cantilever beam

Beam Parameters	Symbol	Value
Modulus of Elasticity (GPa)	γ	200
Density (kg/m^3)	ρ	7.500
Length (inch)	L	6.8
Width (inch)	w	1
Thickness (inch)	t	0.01

Using the values in Table 4, the maximum theoretical beam tip displacement was 0.25 mm, the maximum slope at the tip was 0.12 degrees, and the natural frequency of the

system was 6.0 Hz. A theoretical linear response range within the colloid thruster limits is indicated by the values specified in Table 4. Calibration was the only way to know exactly how the physical system responded, but before a calibration was taken, the lone response signal was analyzed.

To ensure there were no outside signals or periodic noise corrupting the response the displacement sensor response signal was analyzed. In order to check if there were any hidden reoccurring frequencies in the signal, the fast averaging response signal of 5 kHz was put through a Fast Fourier Transform (FFT). Figure 40 displays the direct sensor signal. This figure displays the raw data received from the sensor and shows how the mean signal remains almost constant over the 30 s duration.

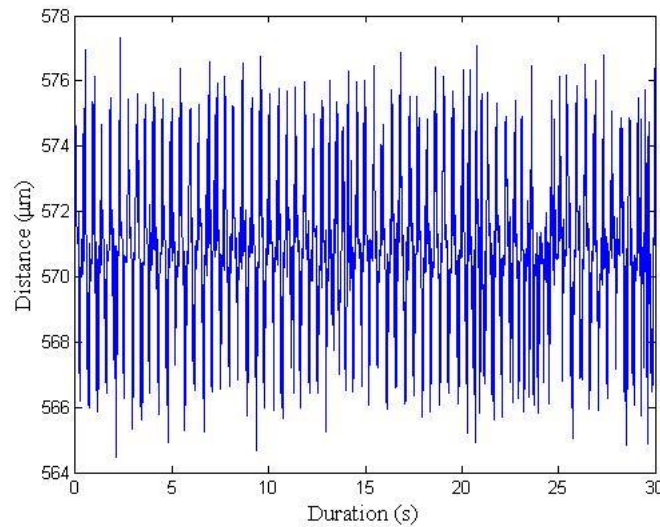


Figure 40. Distance sensor response raw data with a 5000 Hz sampling rate.

Figure 41 provides a closer look at the signal response by showing only the first four seconds of response. A periodic response of approximately every half second is shown on the response curve in Figure 41.

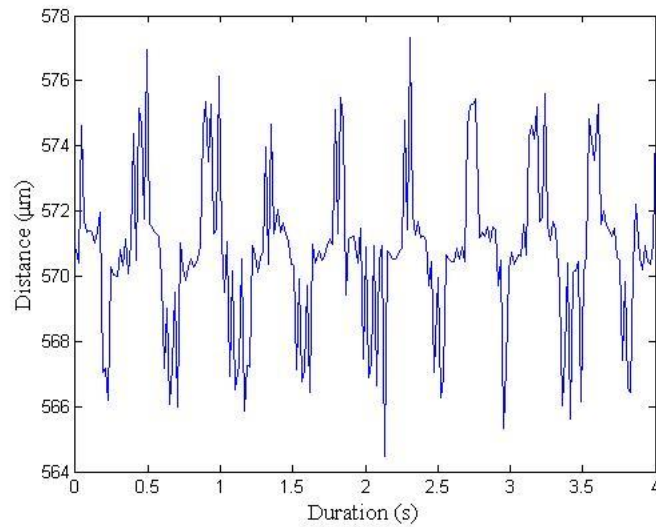


Figure 41. Distance sensor raw data during the 5000 Hz sampling rate in the first four seconds of data collection.

To detect any powerful ambient noise in the system, the data in Figure 40 and Figure 41 was transformed from the time domain into the frequency domain through the FFT process. MATLAB's *fft* function was used to execute the transform and the result is shown in Figure 42. The response is shown as a single-sided amplitude spectrum. There is no dominant time-dependent signal in the sensor as shown in the FFT data. This is the desired result because it means there are no background mechanisms generating noise in the sensor's data. Following the verification of detectable outside noise absence corrupting the sensor data, a calibration test was performed.

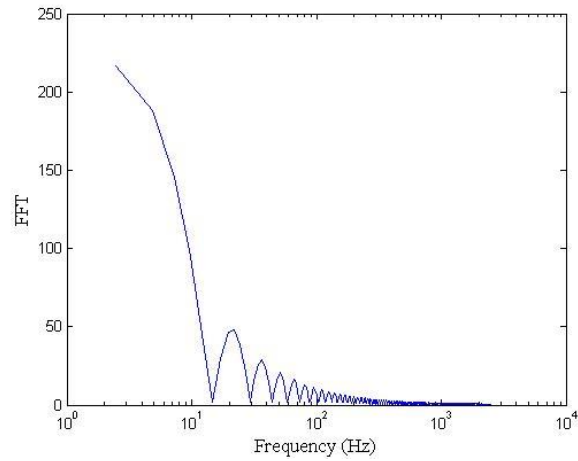


Figure 42. Fast Fourier Transform (FFT) of the 5000 Hz sensor data, shown with logarithmic x-axis.

Using the calibration weights described in Chapter three and performing calibration measurements, the system's response was determined. Figure 43 shows the calibration response curve.

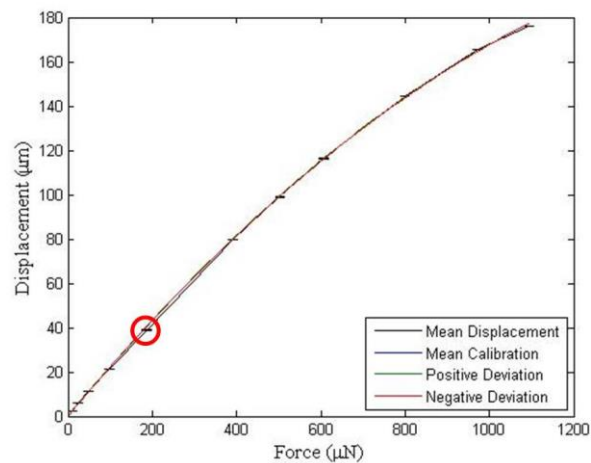


Figure 43. Calibration curve for the cantilever beam thrust measurement setup.

Figure 43 shows four curves. The mean displacement calculated from the sensor's readings is shown on the first curve. Assuming all of the weights were the exact value

given by the scale resulted in the calibration curve labeled “Mean Calibration”. If all of the calibration weights used were either one standard deviation over or under the registered weight, the “Positive Deviation” and “Negative Deviation” calibration curves, respectively, are the resultant theoretical curves. Actual data points were collected where the error bars are shown. The calibration curves shown in Figure 43 are of second order. Through the lower weights the beam system response is nearly linear, but at around 600 μN it becomes visibly nonlinear. A linear profile across the entire spectrum would have been the desired result. However, the calibration curve fits the data extremely well. MATLAB’s *polyfit* function determined the equation for the calibration curve and the standard deviations were calculated from the *polyval* function. Table 5 provides the three calibration curve equations and mean standard deviations, where F is the applied force and δ is the resulting displacement.

Table 5. Calibration data obtained from MATLAB’s *polyval* function

Calibration	Equation	Mean Standard Deviation
Mean	$\delta = -.0001F^2 + .2281F - .1711$	0.9961
Positive	$\delta = -.0001F^2 + .2283F - .0991$	0.9954
Negative	$\delta = -.0001F^2 + .2279F - .2431$	0.9973

A maximum displacement of approximately 180 μm was seen, falling within the desired 250 μm constraint imposed during the system design. All four curves follow an extremely close path, however, the area highlighted by the red circle in Figure 43 has the largest range between the data sets. The calibration curves are approximately 1.5 μm above the mean displacement curve for a given thrust in this region. An uncertainty of

1.5 μm was set by the difference between the calibration curve and displacement curve when converting the thrust to a beam displacement.

Calibration data points were collected for a length of 2 minutes at an average sampling rate of 2.5 Hz. A typical response profile for the 2 minute sampling time frame is displayed in Figure 44. Comparisons can be made between the raw output data from the 2.5 Hz frequency displayed in Figure 44 and the 5 kHz frequency raw data in Figure 40. The local peak-to-peak displacement values in the 2.5 Hz sample are less than 0.1 μm as opposed to the 10 μm range in the 5 kHz sample. Decreasing the frequency results in a clearer picture of the displacement profile over time.

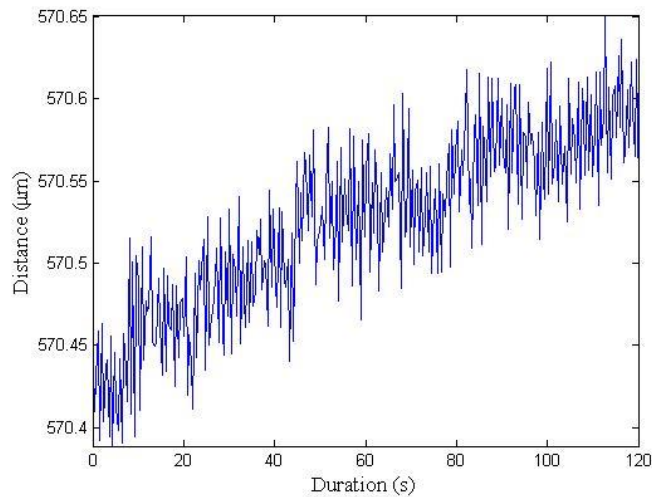


Figure 44. Distance sensor response data collected during a calibration. Data points were produced at an average 2.5 Hz.

Figure 44 shows a changing average along the duration of the collection period. The mean distance drift was never greater than 1 μm . Therefore, 1 μm was taken to be the uncertainty of the distance measurement. Combining the distance measurement

uncertainty with the calibration curve uncertainty, the system's total uncertainty was approximated at $2.5 \mu\text{m}$, assuming the total resolution was the sum of the two uncertainties. Equation (29) was then used with the beam values in Table 4 to calculate the force required to cause a $2.5 \mu\text{m}$ displacement, setting the resolution of the system. A resolution of $10.0 \mu\text{N}$ was calculated from these parameters. Comparing this resolution and calibration to the colloid thruster's specifications was the final analysis involved with the thrust measurement setup.

The colloid thruster operator has the ability to command the thrust in increments of $0.1 \mu\text{N}$ from the colloid thruster's LabView interface. This is greater resolution than the cantilever beam system can detect. Given the overall thrust command, the cantilever beam measurement system is compatible with the thruster software and can provide a rough approximation of the actual thrust produced. In order to obtain a complete understanding of how the beam system relates to the colloid thruster's individual particles, the electric field within the thruster needs to first be well understood, however, a rough approximate was made through the use of Coulomb's Law, Equation (1).

An estimate for the electric field was calculated based on the known thrust and beam current operating conditions of the thruster. An approximation of the number of droplets in the flowfield that fell within the uncertainty of $10.0 \mu\text{N}$ was found using the estimated electric field. Figure 45 displays the results of the number of droplets within the measurement system's thrust uncertainty as a percentage of the total number of droplets.

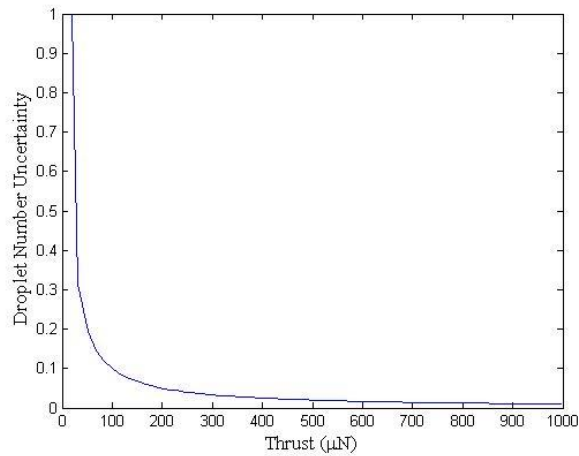


Figure 45. Uncertainty in the number of droplets in the flowfield as a function of the overall thrust.

Figure 45 shows a rapid decrease in the relative droplet uncertainty. At a thrust of $100 \mu\text{N}$, the relative uncertainty drops below 10% and continues decreasing. These results are promising when estimating the overall number of drops in the flowfield over a given time period. The thrust measurement system becomes more accurate at higher operating thrust values as shown by the curve.

Results of the analysis for the elasticity method show how this method is a practical experiment to determine the thrust. Data regarding the measurement system is limited because the displacement sensor failed during system testing, although, the sensor was functioning properly during the calibration trial and the system responded as intended. The calibration data only used weights of increasing mass to calibrate the sensor. However, another set of calibration points with decreasing weights should have been executed to check for hysteresis in the data. After concluding the thrust measurements using the cantilever beam method were viable for use with the colloid

thruster, analysis was completed testing the applicability of the exit velocity measurement experimental setup.

4.4 Exit Velocity Experiment

The next experiment set involved tracking discrete particles as they moved through air and attempted to calculate their velocity profiles. These experiments were important because the specific impulse is directly related to the exit velocity. By knowing the thrust and specific velocity profiles, the colloid thruster's operational envelope can be developed.

A CO₂ dewar was used to create solid CO₂ particles as a model for the colloid thruster plume. A sequence of TIFF images were taken with a 4480 pixel per meter resolution of CO₂ particles exiting the CO₂ dewar nozzle. Two methods were used to measure the velocity profile of the particles. The first method utilized image correlation between adjacent images in the time domain, a sample image is shown in Figure 46.

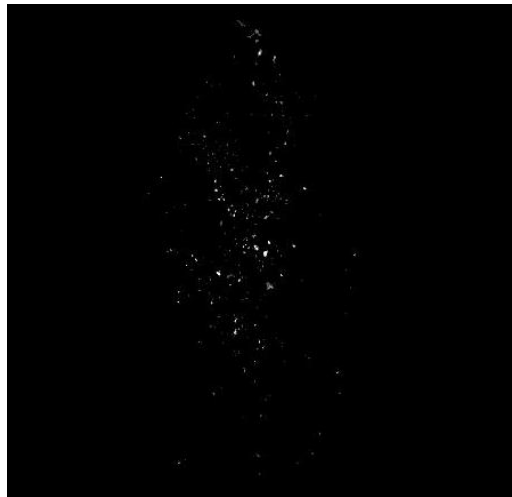


Figure 46. Sample image of CO₂ particles using Phantom camera at 20 μ s exposure time.

Measuring the length of a particle smear across an image was the second method employed. These two methods were compared to the theoretical velocity of 55 m/s, obtained by using Bernoulli's Equation, Equation (41).

Flow emanating from a nozzle has a higher velocity in the center of the flowfield than on the edges. Therefore, the span-wise, or horizontal velocity profile of the CO₂ particles was analyzed to ensure this velocity profile was seen. Image cross correlation was performed through a total 50 images. Particles with pixel areas of 1-10 were considered in the velocity profile. The resulting span-wise profile is displayed in Figure 47.

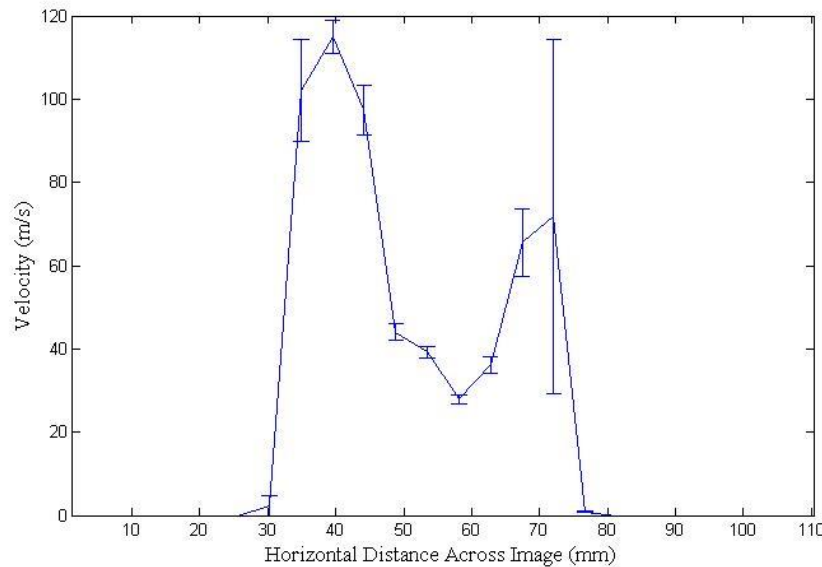


Figure 47. Velocity profile of CO₂ particles across the span of the flow using image cross-correlation.

Figure 47 shows the opposite velocity profile from the expected result. However, upon further investigation of the source images, this velocity profile is correct. In the middle of the flow, approximately 30 to 80 mm, the flow is relatively constant at around 50 m/s.

The error bars are very small because there are numerous particles in this flow regime. However, along the edges of the flow, there are fewer particles, but they are moving considerably faster. Fewer particles account for the large error bars on the edges of the flow. The nozzle orifice is optimized to spray the particles radially out in a disk pattern, but the nozzle redirects this outward spray to an axial flow. Some particles may have briefly frozen to the nozzle wall and then ejected at a higher speed caused by collisions with the flow. The actual diameter of the nozzle was 20.5 mm. Figure 47 shows the fastest particles diverged when exiting the nozzle instead of travelling parallel to the nozzle's axis.

A minimum pixel, or droplet diameter, threshold was established by the velocity determination algorithm to single out particles to include in the calculations. Any drops with a pixel area less than the minimum were not considered by the program. One would expect particles with a higher area and corresponding larger mass to travel slower than particles with a slower mass due to the energy conservation of the particles. Therefore, plots were generated to confirm the velocity differences between the particle sizes, shown in Figure 48. The curves in Figure 48 were also generated to ensure the velocity profiles between each frame were uniform and representative of the entire flowfield. Two data sampling methods were used to obtain the mean velocities and standard errors shown in Figure 48. One method averaged the velocities of all the particles from one frame to the next. After all frames were considered, the method averaged all of the frame-averaged velocities. This method is shown in Figure 48 as the "Frame-to-Frame Average". A second sampling method calculated the mean and standard error using all of the particles

considered throughout the 50 frames without regard to what frame they occurred in. This method was referred to as the “Total Droplet Average”.

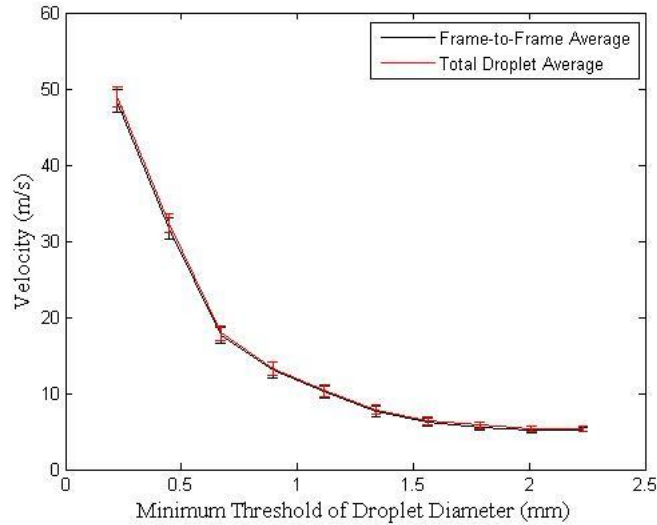


Figure 48. CO₂ particle velocity distribution as a function of the particles' minimum diameter.

Both sets of data are very similar. This result demonstrates the uniformity of the flowfield throughout the 50 sampled frames. The data from one frame to the next aligned with the total averaged data over the entire time of consideration. In addition, the data shows the particles with a larger mass moved at slower velocities as expected. Consequently, the size of the particles should have had a relatively small impact on the velocity profile data shown in Figure 47.

Both image correlation velocity profiles over the nozzle span and particle area provide confidence in this method of velocity determination. Figure 48 shows the average velocity for the particles with pixel areas of greater than or equal to one as approximately 50 m/s. This is a 9% error from the theoretical value of 55 m/s. The

image cross correlation technique was the first velocity tracking method and the particle smear tracking was the other method used to determine the particle velocity profiles.

Particle smear tracking was comprised of imaging the flowfield with a longer exposure time, $500\ \mu\text{s}$ as it pertains to this research, and tracking the number of pixels a particle traveled over the long exposure time. As shown in Figure 49, the image collected light from the particle over the range of its trajectory, leaving a “smear” pattern on the image. A greater number of particles are seen in Figure 49 than with the short exposure time. The long exposure time captures more light from particles, so distant or background particles have a greater tendency of being recorded.

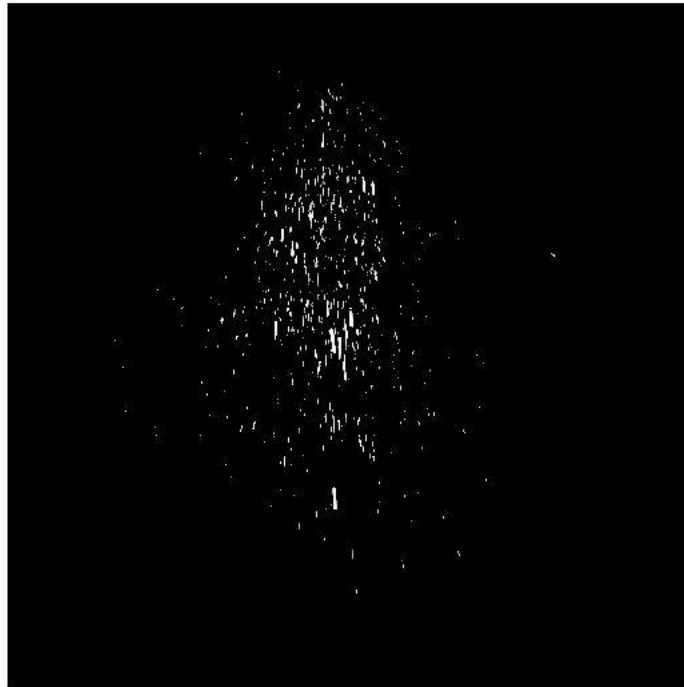


Figure 49. Sample image of CO₂ particles using Phantom camera at $500\ \mu\text{s}$ exposure time.

The particle streaks in Figure 49 are much shorter than anticipated. Methodology used in Chapter three estimated the particle streaks to cross most of the 512 vertical pixels in the image. However, the actual streaks acquired have a distance on the order of tens of pixels instead of hundreds. These short streaks skew the velocity results. Short streak patterns were likely caused by the nozzle arrangement being used for the experiment. The purpose of the CO₂ extractor nozzle is to create an outward disk of particles. Even though the long nozzle redirects the particles in the downward vertical direction, the particles still have some angle in their trajectory after leaving the nozzle. This angle makes the particles pass through the laser sheet very quickly. Instead of being illuminated through the entire image, the particle is only illuminated for a small sliver of time within the full exposure.

Figure 50 presents the velocity profile across the span of the nozzle using the streak method.

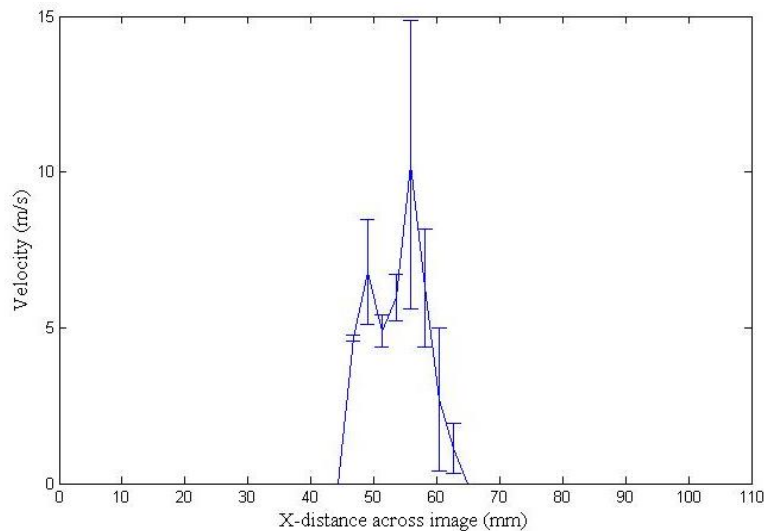


Figure 50. CO₂ particle velocity profile across the span of the flow using the streak tracking method.

The average velocity along the profile is around 10 m/s. Errors along the profile are much larger than in the correlated image data. An area of ambiguity exists with streak tracking because it is difficult to determine exactly where a particle starts and stops during its trajectory. Particles are larger than one pixel so there will be an area of pixels encompassing its end points. It is unclear where the exact location of the particle at those endpoints is, resulting in a higher error to the streak tracking measurement.

Figure 51 shows the particle velocity as a function of minimum streak distance.

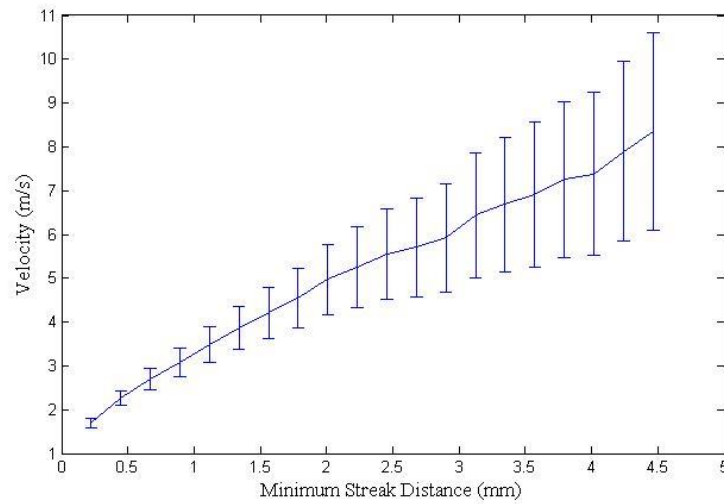


Figure 51. Particle velocity as a function of minimum streak distance.

Increasing streak distance corresponds to increasing particle velocity. Velocity error increases with increasing minimum streak distance due to the decreasing number of sample points. Figure 51 displays a maximum velocity of about 8 m/s, well below the theoretical result of around 55 m/s. The low velocities demonstrate the effect of the particle not remaining illuminated by the laser through the entire exposure time.

Two velocity tracking methods, image correlation and particle streak tracking, have been presented. Based on the results given, the image correlation method provides a more accurate representation of the flowfield than the particle streak tracking. However, if a scheme were devised to ensure a particle remained illuminated by the laser during the entire exposure time, the streak tracking may give better results. There are additional items to consider when determining the suitability of these methods for the colloid thruster. The first is the size of the particle. CO₂ particles were estimated to be between 5 and 15 μm in mean diameter [31]. However, the average size of a droplet from the colloid thruster is from around 0.2 to 1 μm based on the data in Figure 38. Current system resolution will not be able to resolve those small particles. Even if the camera were able to detect the droplets with an appropriate amount of light, their size would only fill a single camera pixel. Attempting to correlate a single pixel with the image correlation method may not provide accurate results. Another consideration is the size of the droplet compared to the laser's wavelength. A colloid thruster droplet will be approximately the same size as the laser's wavelength. Optical irregularities and light intensity issues may be caused by the closeness in size. Since the sizes are close, Mie light scattering could be utilized by illuminating the flowfield from behind where the droplets are located in between the laser and the camera. A filter could be used to block the laser light and allow the scattered light from the particles to pass into the camera. Also, a laser with a different wavelength could be used to minimize any interactions.

4.5 Taylor Cone Visualization

The Taylor Cone visualization experiment attempted to view the Taylor Cone formation with the use of a telescope lens and a high speed camera. An optical system was used to focus white light onto an emitter head. Maximizing the intensity of light on the emitter face while not overexposing the face in the vacuum chamber was the biggest challenge during this experiment. The required mirror and lens setup posed a large obstacle and constrained the thruster placement within the vacuum chamber. Loss of resolution of the thruster head resulted from the spatial constraint.

Pictures taken from the Shimadzu HPV-2 camera of the emitter head are shown in Figure 52.

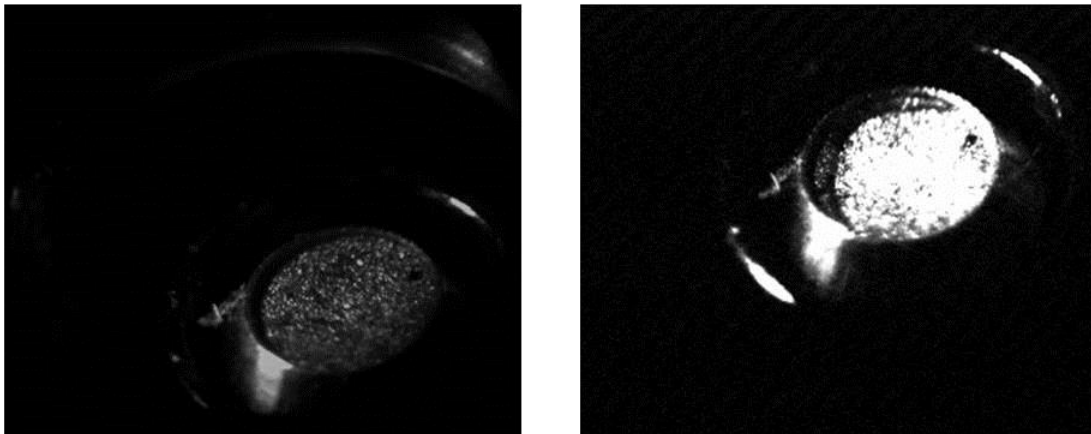


Figure 52. Emitter head pictures taken with the Shimadzu HPV-2 camera. The pictures show the brightness contrast depending on the location of the mirror used to image the emitter.

Figure 52 shows different lighting contrasts. Illumination differences were very dramatic depending on the location of the mirror used to reflect the emitter head image into the plane of the camera. A balance had to be obtained between the angle of the mirror with

respect to the surface and the amount of light received by the camera. As the angle between the mirror face and emitter face became shallower, more light was received by the camera, but a smaller angle meant a more difficult process of analyzing the Taylor Cones. A large angle was desired to see the entire profile of a Taylor Cone and determine the droplet release time. The resolution of the Questar lens and Shimadzu camera combination was limited because of the distance the emitter head was located from the lens as described in Chapter three. Even with the optical system focusing the light onto the emitter head, the minimum exposure time obtained from this setup was $8\text{ }\mu\text{s}$. However, an exposure time of $8\text{ }\mu\text{s}$ should be enough time to view the transient response of a Taylor Cone production based on the previous assumption of the droplet release rate of 1 ms.

During one experiment, the colloid thruster's fuel valve was not properly closed, but floating open. When the vacuum chamber began dropping pressure, propellant began to flow to the emitter surface, as displayed in Figure 53.

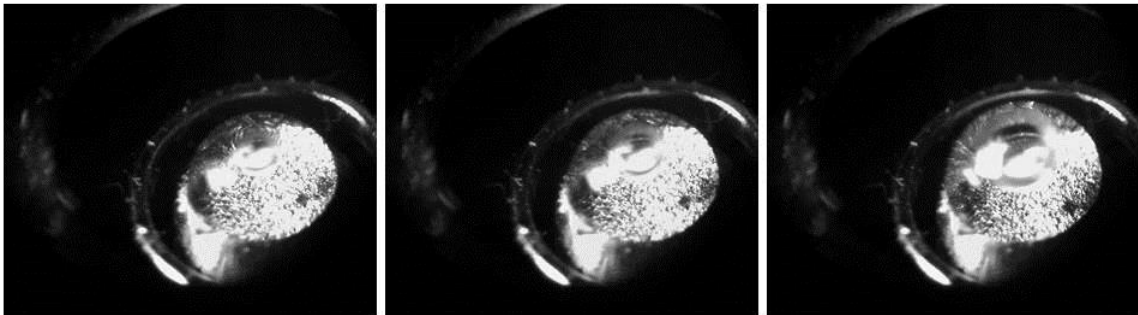


Figure 53. Three pictures capturing the progression of propellant pooling on the emitter head. Time increases with the pictures from left to right.

Figure 53 shows the progression of propellant rising to the emitter surface on backpressure from the propellant tank alone. Even though the thruster was on a level surface, it is interesting to note the propellant progression begins in the top left corner of the emitter head and spreads toward the center. This is in contrast to the expected result of propellant pooling up first from the center and then to the surrounding emitter surface. An explanation to this occurrence may be because the propellant feed system is located on the side of the emitter instead of directly underneath. The side the feed system is connected to dictates where the propellant is first seen. Even though no firm conclusions can be drawn as to why the propellant pooled in the displayed manner, the pictures in Figure 53 do give evidence to the camera system being able to distinguish the propellant from the emitter head. During the maximum flow rate, this will be important because the propellant may be pooled on top of the emitter. However, during the low flow rate case, the propellant most likely will not pool and the Taylor Cones will be difficult to distinguish.

The Taylor Cone observation results show how optics can be used to focus light onto an emitter head. By using the Shimadzu HPV-2 camera, the emitter head can be captured with an exposure time of $8\ \mu\text{s}$. However, the image resolution is the main constraint in this experiment. It is assumed the camera system will not be able to detect and clearly image thousands of Taylor Cones. It is believed at best, the imaging system will distinguish a dry emitter head from a head where propellant is being emitted. The Phantom camera should be used if this experiment is to be attempted again.

Taylor Cone formation imaging was the last experiment to be performed to characterize the colloid thruster. Before any experiments could be performed, the colloid

thruster became inoperable. A summary of the difficulties in preparing the colloid thruster for operation, the attempted startup, and failure conditions are discussed next.

4.6 Thruster Operation

The thruster never became fully operational. Numerous problems plagued the thruster and due to time constraints, a final solution making the thruster operable was never obtained. Additionally, the thruster's startup procedure was never fully completed although many individual steps were and results of those steps are presented. This section also presents some obstacles, and solutions, faced when attempting to operate the thruster.

High voltage connections caused the first set of obstacles encountered during the attempted thruster operation. Voltages as high as 10,000 Volts are present during thruster operation. These voltages flow through the wires and connections from the PPU to the thruster. However, these are not direct connections. The wires must run from the PPU to the outside vacuum chamber walls and then from the corresponding points inside the chamber to the thruster. Several wire connections were needed as a result of this wiring configuration.

Creating safe, electrically isolated wire connections was formidable. This was a problem in previous research with the colloid thruster as well [43]. Soldering was one option, but was not used because it was concluded to be too permanent and would not allow the thruster to be relocated between experiments. Instead of soldering, wire nuts were used to complete the connections. The nuts provided a safe, but temporary connection; however, arcing still resulted in the electrical system. Arcing was a problem

because when an arc occurred, the PPU would discontinue communication with the host computer. All output values from the PPU returned as zero and the PPU could not be controlled by the computer. The arcing problem was fixed by wrapping all electrical connections in high voltage electrical tape. Frequent arcing in the electrical system resulted in the PPU becoming altered.

A second obstacle was establishing the correct communication channels between the PPU and the host computer. The PPU terminates with an RS232 output. However, many present-day computers no longer have RS232 terminals, only USB ports. An RS232-to-USB converter was connected the RS232 from the PPU to the USB on the computer. Even though the physical connections mated well and the communication parameters (baud rate, stop bits, etc) were correct, the host computer could not communicate properly with the PPU. This problem was apparent based on the non-numerical, random ASCII character dialog received from the PPU. This problem was solved by locating a computer with an RS232 input and directly connecting the PPU output to the computer.

Using a high voltage power supply to provide enough power to the PPU was an additional obstacle. Early in the research, smaller power supplies were used with a voltage output of greater than 28 V, however, the lack of available current became the limiting factor. When the PPU was enabled, the power from the power supply dropped. This power drop was evidence of the PPU attempting to draw too much current and power from the power supply. Finding a power supply with an amperage limit of over 1.5 A was the solution to this problem.

Once the problems listed above were resolved, the operator was able to communicate properly with the thruster and begin the startup procedure for operation. However, during the startup procedure, severe problems surfaced resulting in the shutdown of the attempted experiments. Data taken from the thruster during the startup procedure is presented.

The first step of the procedure was to perform a high voltage impedance test ensuring there was not a short in the thruster's electrical isolation structure. A short would be evident if any beam current registered during the test. Figure 54 presents the beam voltage as a function of time and shows the gradual steps in the commanded beam voltage during this test. The thruster achieved and held the required maximum beam voltage of 10,000 V without any beam current registering.

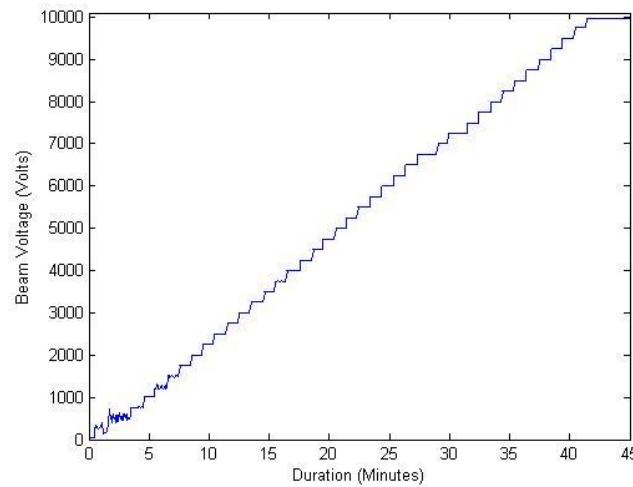


Figure 54. Beam voltage data captured during the high voltage impedance test as part of the startup procedure.

Figure 55 shows the thruster beam voltage and valve voltage as a function of the startup procedure duration. The end of the plots represents the point when the PPU output became extremely erratic and eventually terminated. The high voltage impedance test is shown in the area of the green box.

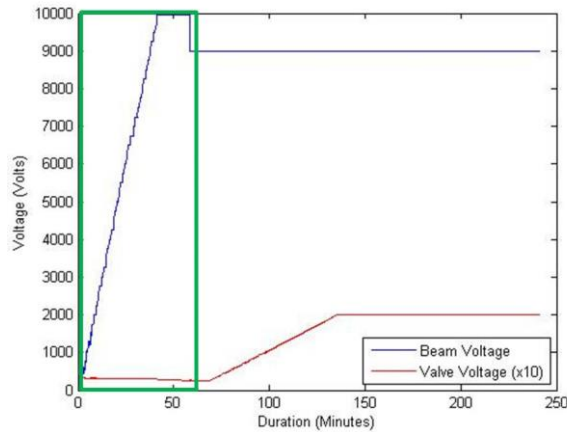


Figure 55. Beam voltage and valve voltage data captured during thruster startup procedure.

Figure 55 displays the steadiness of the beam voltage through the startup procedure. The beam voltage data is only one aspect of the startup procedure.

Another important parameter during the startup procedure is the propellant regulation valve voltage. The propellant valve regulates the flow of propellant from the storage tank to the emitter. The valve voltage automatically adjusts to the required value based on the user-commanded beam current. During the high voltage impedance test, the beam current remained near zero so the valve voltage was correspondingly zero. In Figure 55 the valve voltage shows to be slightly above zero during the impedance test, but these values are attributed to system noise. After the impedance test, the beam current was commanded to $20 \mu\text{A}$. The rise in beam current signaled the valve voltage to

increase allowing propellant to flow to the emitter. Once the beam current was commanded to $20\ \mu\text{A}$, the valve voltage began to rise as expected, seen in Figure 55. The valve voltage held steady at 200 V until the output became unreliable. In order to examine the thruster and electronics systems, the thruster startup operation was then terminated by the operator.

The vacuum chamber was subsequently vented and the thruster was investigated for problems. A propellant leak was immediately noticed. It was believed the thruster had air pockets in the propellant causing arcs between the emitter and acceleration grid. The arc disabled the PPU leaving the valve voltage at the full value so propellant flowed through the emitter. Instead of being ejected as in normal operation, the propellant simply leaked down the sides of the thruster because the acceleration grid was not powered. After the thruster was cleaned a second operating attempt was made. During the second attempt, the high voltage impedance test could not be completed during the startup procedure. The thruster's parameters outputted from the PPU were irregular and the thruster did not operate properly. The vacuum chamber was vented again and the thruster was investigated. After the second attempt, there was a dark brown liquid on the bottom of the thruster, shown in Figure 56. It is believed this is again propellant, but it appears burnt. One theory for this result is there was a leak in the propellant system instead of the regulatory valve being open. When the high voltage impedance test was being performed propellant met an open electrical source and burned. Further investigation is required before a final assessment can be made on the cause of the propellant spillage.



Figure 56. Image of the propellant pool around the thruster's base after attempted operation.

4.7 Summary

The results from performing the actions discussed in Chapter three have been presented. Along with the results, relevant discussion regarding the results was provided. Each experiment's results show promise to being used during colloid thruster operation, however, this research was unable to use the results directly with the thruster. The final chapter, Chapter five, will summarize conclusions from this research.

V. Conclusions and Recommendations

This chapter presents a summary of the work performed and conclusions drawn from the research. A brief synopsis of each experiment set will be given. Next, the significance of this research is addressed, including why it is relevant and what benefit it brings future researchers. Finally, recommendations for continuing research in this area are presented.

5.1 Conclusions of Research

Research has been performed to develop a working theory of the variable number of emitter sites and droplets released during operation of the porous emitter colloid thruster. The porous emitter heads were imaged under a microscope to determine the surface topography. Algorithms calculating the maximum and minimum number of potential emitter sites from the captured images were developed. After the extremes in emitter sites were estimated, the overall thruster performance was calculated along with the range of exhaust droplet parameters. A potential experiment to measure the thrust output using a cantilever beam and distance sensor was then analyzed. A candidate experiment to determine the droplet's exit velocity was detailed. To illuminate the flowfield enough to image the droplets and determine their exit velocity through postprocessing techniques, a laser was used. Next, a Taylor Cone formation imaging process was described and analyzed for obtaining a better estimate for the droplet release time and number of emitter sites. Finally, the attempted thruster operation was discussed.

The work performed completed three out of four of the original objectives of this research. A theory was developed for the potential number of emitter sites given a flow

rate condition. Processes for determining the thrust and exit velocity of the exhaust plume were developed and analyzed. Also, a method for imaging the Taylor Cone formation was created and inspected. However, the methods and techniques developed could only be compared qualitatively to the colloid thruster's operation. The last objective of performing the various experiments on the colloid thruster was not achieved. Regardless of the final objective remaining unaccomplished, the research performed remains significant.

5.2 Significance of Research

The research performed as part of this thesis has provided a foundational theory of how the number of emitter sites varies with propellant mass flow rate and beam current on AFIT's colloid thruster. The theory developed gives an estimate of the performance parameters and droplet specifications. Enhanced mission analysis on the integration of this thruster as the AFIT CubeSat propulsion system can be conducted using the thruster performance parameters of thrust and specific impulse. Droplet specifications can be utilized when generating experiments or analysis to further measure and quantify the thruster's operating characteristics. Experimental methods for performance testing have been reviewed and analyzed. They can be applied as a baseline for future research not only on the colloid thruster, but any future researcher can use the analysis to understand considerations for his or her own experiments.

A new measurement capability of determining thrust from a cantilever beam system was demonstrated in the AFIT laboratory. Future research can replicate these experiments for various other applications. The optical experimental methods proposed

to obtain the exit velocity can expand the electric propulsion community's body of knowledge in this subject. Optical methods of beam deflection measuring and particle tracking can be added to existing measurement methods as an alternative way of experimentally determining an electric thruster's specific impulse and thrust performance parameters.

5.3 Recommendations for Future Research

This research has provided a foundational theory and experimental techniques for analyzing the colloid thruster. Future work may be dedicated to applying the developed experimental techniques on the colloid thruster to measure its operational performance. Once the thruster's operational envelope is laboratory tested, the algorithms used to determine the maximum and minimum number of emitter sites can be refined and optimized to more accurately reflect the actual performance. Current algorithms have parameters requiring the user to arbitrarily select their values. Improvements can be made in the codes and more images can be processed to develop as accurate a solution as possible. Additional thruster analysis and development can then be based on the computer model.

Two methods of obtaining the exit velocity of the particles were discussed in this thesis, direct imaging and PDV. Due to time constraints, PDV was never attempted therefore; this method can be an area of future research. However, before utilizing a new method for velocity determination of the flowfield, improvements can be made to the direct imaging methods. As a method of viewing the flowfield, the image correlation technique showed promise. This method can be enhanced by using a pulsed laser. A

pulsed laser would provide more incident light on the flowfield, allowing a shorter exposure time with the camera. If the relative difference between images is reduced, hence, having images closer together in time, the image correlation technique can be improved. Broadening the thickness of the laser sheet may improve the streak method. A thicker laser sheet may illuminate the droplets through the full range of the camera's field of view providing more accurate smear tracking results.

A final recommendation is to design and build a test rig for using the cantilever beam setup. Repeatedly aligning the thruster emitter head grid precisely with each catcher plate is a crucial step to accurately determine the plume divergence. During the work of this thesis, no such part was formed making repeated precision alignment a laborious task. In order to facilitate repeatable experiments, an assembly devoted to precisely aligning the emitter grid, catcher plate, beam tip, and sensor should be devised.

5.4 Summary

Investigation of various electric propulsion devices for possible use with the AFIT-designed 3U CubeSat prompted the work of this thesis. The porous emitter colloid thruster is a novel design and its operating parameters are not yet fully understood. Groundwork for a better understanding of the thruster's performance parameters was established by the research performed. Experimental methodologies for use on the thruster were provided to enable future researchers to determine the thruster's capabilities and potential for future AFIT CubeSat missions.

Bibliography

- [1] Ainsworth, R. W., Thorpe, S. J., & Manners, R. J. (1997). A new approach to flow-field measurement - A view of doppler global velocimetry techniques. *The International Journal of Heat and Fluid Flow.*, 18(1), 116.
- [2] Baird, D. C. (1995). *Experimentation: an introduction to measurement theory and experiment design* (Third ed.). NJ: Prentice Hall.
- [3] Bayvel, L., & Orzechowski, Z. (1993). In Chigier N. (Ed.), *Liquid atomization*. USA: Taylor & Francis.
- [4] Benignos, J. A. C. (2005). *Numerical simulation of a single emitter colloid thruster in pure droplet cone-jet mode*. (Doctor of Philosophy, Massachusetts Institute of Technology).
- [5] Bertin, J. J. (2002). *Aerodynamics for engineers* (4th ed.). NJ: Prentice Hall.
- [6] Boguszko, M., & Elliott, G. S. (2005). Property measurement utilizing atomic/molecular filter-based diagnostics. *Progress in Aerospace Sciences* *Progress in Aerospace Sciences*, 41(2), 93-142.
- [7] Busek.CubeSat electrospray thruster system. Retrieved December 10, 2012, from http://www.busek.com/technologies_espray.htm
- [8] Cardiff, E., Jamieson, B., Norgaard, P., & Chepko, A. (2004). The NASA GSFC MEMS colloidal thruster. *40th AIAA/ASME/SAE/ASEE Joint Propulsion Conference*, Fort Lauderdale, FL.
- [9] Charrett, C., & Tatum, R. (2006). Single camera three component planar velocity measurements using two-frequency planar doppler velocimetry. *Measurement Science and Technology*, 17, 1194.
- [10] Cherney, L. (1999). Structure of taylor cone-jets: Limit of low flow rates. *Journal of Fluid Mechanics*, 378, 167.
- [11] Clemens, N. (2002). Flow imaging. *Encyclopedia of Imaging Science and Technology*, , 390.
- [12] Cowen, E. A., & Monismith, S. G. (1997). A hybrid digital particle tracking velocimetry technique. *Experiments in Fluids*, 22, 199.
- [13] De La Mora, J. F., & Loscertales, I. G. (1994). The current emitted by highly conducting taylor cones. *Journal of Fluid Mechanics*, 260, 155.

- [14] Demmons, N. (2010). *1U colloid thruster & electronics operation manual*. (). Natick, MA: Busek.
- [15] Deng, W., & Alessandro, G. (2012). Full transient response of taylor cones to a step change in electric field. *Microfluid Nanofluid*, 12, 383.
- [16] Fischer, A., Sell, F., Buttner, L., & Czarske, J. (2011). Self-calibrating doppler global velocimetry with laser frequency modulation. *Sensor and Test Conferences 2011*, 66.
- [17] Gamero-Castano, M. (2003). A torsional balance for the characterization of microNewton thrusters. *Review of Scientific Instruments*, 74(10), 4509.
- [18] Gamero-Castano, M. (2008). Characterization of the electrosprays of 1-ethyl-3-methylimidazolium bis(trifluoromethylsulfonyl) imide in vacuum. *Physics of Fluids*, 20, 20.
- [19] Gamero-Castano, M., & Hruby, V. (2001). FULL-LENGTH PAPERS - electrospray as a source of nanoparticles for efficient colloid thrusters. *Journal of Propulsion and Power*, 17(5), 977.
- [20] Gamero-Castano, M., & Hruby, V. (2001). A torsional balance that resolves sub-micro-newton forces. *27th International Electric Propulsion Conference*, Pasadena, CA.
- [21] Gamero-Castano, M., & Ziemer, J. (2005). Characterization of colloid thruster beams. *29th International Electric Propulsion Conference*,
- [22] Ganan-Calvo, A. M. (1997). Cone-jet analytical extension of taylor's electrostatic solution and the asymptotic universal scaling laws in electrospraying. *Physical Review Letters*, 79(2), 217.
- [23] Griffiths, D. J. (1999). *Introduction to electrodynamics* (Third ed.). NJ: Prentice Hall.
- [24] Harrington, R. C. (2012). *Final design and integration of the ALICE CubeSat mission*. (Master's thesis, Air Force Institute of Technology).
- [25] Hecht, E. (2001). *Optics, 4th edition* Addison-Wesley.
- [26] Henry, G. N., Larson, W. J., Humble, R. W., United States. Dept. of Defense., & United States. National Aeronautics and Space Administration. (1995). *Space propulsion analysis and design*. New York: McGraw-Hill.

- [27] Higuera, F. J. (2003). Flow rate and electric current emitted by a taylor cone. *Journal of Fluid Mechanics*, 484, 303.
- [28] Jahn, R. G. (2006). *Physics of electric propulsion*. NY: Dover.
- [29] Krpoun, R., & Shea, H. R. (2009). *Microfabricated out-of-plane arrays of integrated capillary nano-electrospray emitters*. Microsystems for Space Technologies Laboratory.
- [30] Laser Innovations. (2012). Verdi laser. Retrieved October 23, 2012, from http://www.532nm.com/VerdiLaser_532nm_LaserInnovations.htm
- [31] Love, B. (2010). *Particle size control for PIV seeding using dry ice*. (M.S., Air Force Institute of Technology).
- [32] Lozano, P. (2006). Energy properties of an EMI-IM ionic liquid ion source. *Journal of Physics D: Applied Physics*, 39, 126.
- [33] Lozano-Tovar, P. C., & Massachusetts Institute of Technology. Dept. of Aeronautics and Astronautics. (2003). *Studies on the ion-droplet mixed regime in colloid thrusters*.
- [34] Lu, Z., Charrett, T. O. H., & Tatam, R. P. (2009). Three-component planar velocity measurements using mach-zehnder interferometric filter-based planar doppler velocimetry (MZI-PDV). *Measurement Science and Technology*, 20
- [35] Lun, J., Dobson, R. T., & Steyn, W. H. (2012). Performance measurements of a medium-current short-pulsed vacuum arc thruster. *Experimental Techniques*,
- [36] Martinez-Sanchez, M. (2012). *Colloidal engines*. MIT:
- [37] McNamara, P. (2009). *Overview of LISA pathfinder*. (No. LISA-LPF-RP-0001).European Space Agency.
- [38] Meier, A., & Roesgen, T. (2012). Imaging laser doppler velocimetry. *Experiments in Fluids*, 52, 1017.
- [39] Mueller, J. (1997). *Thruster options for microspacecraft: A review and evaluation of existing hardware and emerging technologies*. (No. AIAA 97-3058).American Institute of Aeronautics and Astronautics.
- [40] Nabity, J. (2007). *The miniaturization of the colloid thruster to the micro scale*. (Unpublished Doctor of Philosophy). University of Colorado,

- [41] Newport. (2012). Beam shaping with cylindrical lenses. Retrieved October 23, 2012, from <http://www.newport.com/Beam-Shaping-with-Cylindrical-Lenses/144888/1033/content.aspx>
- [42] NIST/SEMATECH. (2012). Engineering statistics handbook. Retrieved September, 2012, from <http://www.itl.nist.gov/div898/handbook/index.htm>
- [43] Ober, S. T. (2011). *CubeSat packaged electrospray thruster evaluation for enhanced operationally responsive space capabilities*.
- [44] Ohmi, K., & Li, H. (2000). Particle-tracking velocimetry with new algorithms. *Measurement Science and Technology*, 11, 603.
- [45] Pantano, C., Ganan-Calvo, A. M., & Barrero, A. (1994). Zeroth-order electrohydrostatic solution for electrospraying in cone-jet mode. *Journal of Aerosol Science*, 25(6), 1065.
- [46] Pranajaya, F. M., & Cappelli, M. A. (2001). Performance studies of a colloid thruster system. *27th International Electric Propulsion Conference*, Pasadena, CA.
- [47] Questar. (2012). QM 100 long-distance microscope. Retrieved May 1, 2012, from <http://www.questar-corp.com/>
- [48] Randolph, T., Ziemer, J., Hruby, V., Spence, D., Demmons, N., Roy, T., & Connolly, B. (2006). Microthruster propulsion for the space technology 7 (ST7) technology demonstration mission. *42nd AIAA/ASME/SAE/ASEE Joint Propulsion Conference and Exhibit*, Sacramento, CA.
- [49] Reichbach, J., Sedwick, R., & Martinez-Sanchez, M. (2001). Micropropulsion system selection for precision formation flying satellites. *37th AIAA/ASME/SAE/ASEE Joint Propulsion Conference*, Salt Lake City, UT.
- [50] Riley, W., Sturges, L., & Morris, D. (1999). *Mechanics of materials* (Fifth ed.). NY: Wiley.
- [51] Shafer-Ray, N. (2006). Maxwell stress tensor. Retrieved January 7, 2012, from http://www.nhn.ou.edu/~shaferry/41832005_files/l4.pdf
- [52] Si, B. Q., T., Byun, D., & Lee, S. (2007). Experimental and theoretical study of a cone-jet for an electrospray microthruster considering the interference effect in an array of nozzles. *Journal of Aerosol Science*, 38, 924.

- [53] Soetomo, F., Colver, G., & Forouraghi, K. (2006). Micro-force measurement of drag on a small flat plate in the presence of a corona discharge. *Journal of Electrostatics*, 64, 525.
- [54] Stark, J., Smith, K., & Robertson, S. (2003). High accuracy measurements in electrospray source relevant to colloid thrusters. *39th AIAA/ASME/SAE/ASEE Joint Propulsion Conference*, Huntsville, AL.
- [55] Sutton, G., & Biblarz, O. (2010). *Rocket propulsion elements* (Eighth ed.). NJ: Wiley.
- [56] Tang, H., Chao-Jin, Q., & Liu, Y. (2011). Characterization of colloid thruster beams and plumes. *Journal of Aerosol Science*, 42, 114.
- [57] Taylor, G. (1969). Electrically driven jets. *Proceedings of the Royal Society of London. Series A, Mathematical and Physical Sciences*, 313(1515), 453.
- [58] The Mathworks. (2010). *Matlab* (R2010a ed.)
- [59] Thompson, W., & Dahleh M. (1997). *Theory of vibration with applications* (5th Edition ed.) Prentice Hall.
- [60] Tirsi, S. (2008). *Characterizing the exhaust plume of the micro pulsed plasma thrusters by high speed imagery*. (Master of Science in Astronautical Engineering, Air Force Institute of Technology).
- [61] United States. Air Force. Chief Scientist's Office. (2010). *Report on technology horizons : A vision for air force science and technology during 2010-2030, volume 1*. Washington, D.C.: Chief Scientist's Office, United States Air Force.
- [62] University of Washington. Surface/Interfacial tension. Retrieved December 19, 2012, from <http://depts.washington.edu/>
- [63] Urdiales, J. (2004). *Progress in colloid propulsion*. (Master of Science in Aeronautics and Astronautics, Massachusetts Institute of Technology).
- [64] Wilm, M., & Mann, M. (1994). Electrospray and taylor-cone theory, dole's beam of macromolecules at last? *International Journal of Mass Spectrometry and Ion Processes*, 136, 167.
- [65] Wolfram Mathworld. (2013). Standard error. Retrieved January, 2013, from <http://mathworld.wolfram.com/StandardError.html>

- [66] Xiong, J., Zhaoying, Z., Xiongying, Y., Xiaohao, W., Yanyin, F., & Yonghong, L. (2002). A colloid micro-thruster system. *Microelectronic Engineering*, (61-62), 1031.
- [67] Xiong, J., Zhou, Z., Sun, D., & Ye, X. (2005). Development of a MEMS based colloid thruster with sandwich structure. *Sensors and Actuators A: Physical*, 117(1), 168-172.
- [68] Zeleny, J. (1917). Instability of electrified liquid surfaces. *The Physical Review*, X(1)
- [69] Ziemer, J., Randolph, T., Franklin, G., Hruby, V., Spence, D., Demmons, N., . . . Connolly, W. (2010). Colloid micro-newton thrusters for the space technology 7 mission. *2010 IEEE Aerospace Conference*,

REPORT DOCUMENTATION PAGE				Form Approved OMB No. 074-0188	
<p>The public reporting burden for this collection of information is estimated to average 1 hour per response, including the time for reviewing instructions, searching existing data sources, gathering and maintaining the data needed, and completing and reviewing the collection of information. Send comments regarding this burden estimate or any other aspect of the collection of information, including suggestions for reducing this burden to Department of Defense, Washington Headquarters Services, Directorate for Information Operations and Reports (0704-0188), 1215 Jefferson Davis Highway, Suite 1204, Arlington, VA 22202-4302. Respondents should be aware that notwithstanding any other provision of law, no person shall be subject to any penalty for failing to comply with a collection of information if it does not display a currently valid OMB control number.</p> <p>PLEASE DO NOT RETURN YOUR FORM TO THE ABOVE ADDRESS.</p>					
1. REPORT DATE (DD-MM-YYYY) 22-03-2013		2. REPORT TYPE Master's Thesis		3. DATES COVERED (From - To) August 2011 - March 2013	
4. TITLE AND SUBTITLE Porous Emitter Colloid Thruster Performance Characterization Using Optical Techniques				5a. CONTRACT NUMBER	
				5b. GRANT NUMBER	
				5c. PROGRAM ELEMENT NUMBER	
6. AUTHOR(S) Wolf, Eric T., Captain, USAF				5d. PROJECT NUMBER 13Y109	
				5e. TASK NUMBER	
				5f. WORK UNIT NUMBER	
7. PERFORMING ORGANIZATION NAME(S) AND ADDRESS(S) Air Force Institute of Technology Graduate School of Engineering and Management (AFIT/ENY) 2950 Hobson Way, Building 640 WPAFB OH 45433-8865				8. PERFORMING ORGANIZATION REPORT NUMBER AFIT-ENY-13-M-36	
9. SPONSORING/MONITORING AGENCY NAME(S) AND ADDRESS(ES) Space & Missile Division, Propulsion Directorate, Air Force Research Laboratory 1 Ara Road, Bldg 8595, Rm 143 Edwards AFB, CA 93524 (661) 275-6799 (DSN: 525-6799); William.Hargus@edwards.af.mil Dr. William A. Hargus				10. SPONSOR/MONITOR'S ACRONYM(S) AFRL/RQRS	
				11. SPONSOR/MONITOR'S REPORT NUMBER(S)	
12. DISTRIBUTION/AVAILABILITY STATEMENT APPROVED FOR PUBLIC RELEASE; DISTRIBUTION UNLIMITED.					
13. SUPPLEMENTARY NOTES This material is declared a work of the U.S. Government and is not subject to copyright protection in the United States.					
14. ABSTRACT This research focuses on experimentally characterizing the performance parameters of a colloid thruster with porous emitters through optical techniques. Porous emitters are different than traditional needle emitters in how they allow a variation in the number and size of Taylor Cones throughout a range of propellant volumetric flow rate conditions. An algorithm is created to calculate the estimated minimum and maximum number of emitter sites based on magnified images of the porous emitter heads. Theoretical thruster performance parameters are then established from the estimated number of emitter sites. Experimental techniques for measuring the thrust and exhaust exit velocity are proposed. They are then analyzed for their compatibility and limitations with colloid thruster testing based on the theoretical performance parameters. The research and analysis lays the foundation for future colloid thruster testing and characterization. This baseline model and analysis can be refined through laboratory testing in order to be used for future mission analysis determining the viability of the new porous emitter as an enhanced colloid thruster feature over traditional needles.					
15. SUBJECT TERMS Colloid Thruster, Electric Propulsion, Porous Emitter					
16. SECURITY CLASSIFICATION OF:			17. LIMITATION OF ABSTRACT	18. NUMBER OF PAGES	19a. NAME OF RESPONSIBLE PERSON
a. REPORT	b. ABSTRACT	c. THIS PAGE			David Liu, Capt, USAF ADVISOR
U	U	U	UU	135	19b. TELEPHONE NUMBER (Include area code) (937) 255-3636, ext 4542 (David.Liu@afit.edu)

